



---

# Navigating phase diagram complexity to guide robotic inorganic materials synthesis

---

In the format provided by the authors and unedited

# Supplementary Information Contents

<b>SI1. Synthesis planning theory</b> .....	<b>3</b>
SI1.1. Synthesis planning algorithm.....	3
SI1.2. Precursor selection principles using chemical potential diagrams.....	5
SI1.3. Comparison against other synthesis prediction algorithms.....	8
<b>SI2. Robotic laboratory setup and procedures</b> .....	<b>9</b>
SI2.1. ASTRAL system overview.....	9
SI2.1.1. Mobile robotic arm.....	9
SI2.1.2. Sample handling.....	10
SI2.1.3. Powder dispensing.....	11
SI2.1.4. Liquid handling.....	12
SI2.1.5. Ball milling.....	13
SI2.1.6. Solvent removal.....	14
SI2.1.7. High temperature heat treatment.....	15
SI2.1.8. X-ray diffraction.....	15
SI2.2. ASTRAL platform software implementation.....	16
SI2.2.1. ASTRAL python controller.....	16
SI2.2.2. Experiment planning.....	17
SI2.2.3. Automated XRD analysis.....	17
SI2.2.4. Reproducibility Analysis.....	20
SI2.3. Challenges and solutions of automated powder ceramic synthesis.....	21
<b>SI3. Synthesis result analysis</b> .....	<b>23</b>
SI3.1. Summary of synthesis recipes and results.....	23
SI3.2. Metastable materials synthesis efficacy.....	25
SI3.3. Comparison of energy contribution between $T\Delta S$ and $\Delta H$ .....	26
SI3.4. Failed synthesis: Summary/discussion.....	31
SI3.5. Reaction compound convex hull, XRD, phase purity of 35 target systems.....	32
LiZnPO <sub>4</sub> .....	32
LiMnPO <sub>4</sub> .....	33
Li <sub>2</sub> CuP <sub>2</sub> O <sub>7</sub> .....	34
LiMgPO <sub>4</sub> .....	35

BaLiBO <sub>3</sub> .....	36
SrLiBO <sub>3</sub> .....	37
Li <sub>3</sub> Pr <sub>2</sub> (BO <sub>3</sub> ) <sub>3</sub> .....	38
LiGeBO <sub>4</sub> .....	39
K <sub>3</sub> LiP <sub>2</sub> O <sub>7</sub> .....	40
Li <sub>3</sub> Sc <sub>2</sub> (PO <sub>4</sub> ) <sub>3</sub> .....	41
Li <sub>3</sub> V <sub>2</sub> (PO <sub>4</sub> ) <sub>3</sub> .....	42
KLi(PO <sub>3</sub> ) <sub>2</sub> .....	43
Li <sub>2</sub> TiSiO <sub>5</sub> .....	44
LiNbGeO <sub>5</sub> .....	45
Li <sub>2</sub> TiGeO <sub>5</sub> .....	46
Li <sub>3</sub> Fe <sub>2</sub> (PO <sub>4</sub> ) <sub>3</sub> .....	47
KBaPO <sub>4</sub> .....	48
BaNaBO <sub>3</sub> .....	49
KMgPO <sub>4</sub> .....	50
NaSrBO <sub>3</sub> .....	51
K <sub>3</sub> Bi <sub>2</sub> (PO <sub>4</sub> ) <sub>3</sub> .....	52
K <sub>2</sub> Zr(PO <sub>4</sub> ) <sub>2</sub> .....	53
K <sub>3</sub> Al <sub>2</sub> (PO <sub>4</sub> ) <sub>3</sub> .....	54
KTiPO <sub>5</sub> .....	55
KNiPO <sub>4</sub> .....	56
K <sub>3</sub> Fe <sub>2</sub> (PO <sub>4</sub> ) <sub>3</sub> .....	57
KNbWO <sub>6</sub> .....	58
KTa <sub>2</sub> PO <sub>8</sub> .....	59
Li <sub>3</sub> Y <sub>2</sub> (BO <sub>3</sub> ) <sub>3</sub> .....	60
Na <sub>2</sub> Al <sub>2</sub> B <sub>2</sub> O <sub>7</sub> .....	61
NaSiBO <sub>4</sub> .....	62
KTiNbO <sub>5</sub> .....	63
LiSi <sub>2</sub> BO <sub>6</sub> .....	64
LiNbWO <sub>6</sub> .....	65
LiZnBO <sub>3</sub> .....	66

## SI1. Synthesis planning theory

### SI1.1. Synthesis planning algorithm

The code used to predict precursors for more efficient synthesis is open-sourced at [https://github.com/dd-debug/synthesis\\_planning\\_algorithm](https://github.com/dd-debug/synthesis_planning_algorithm). The code is built in python, and leverages the Materials Project Application Programming Interface (API) and the pymatgen code base, specifically, the `pymatgen.analysis.phase_diagram` and `pymatgen.analysis.interface_reactions` modules.

Compositions and energies of various materials systems were retrieved from the Materials Project using the REST API in December 2020.

To determine the list of 3104 reactions in the supplementary data, along with the precursors predicted using our design principles, we first collect all quaternary oxides with Li-, Na-, and K- cations, including quaternary oxides that have complex phosphate ( $\text{PO}_4$ )<sup>3-</sup> and borate ( $\text{BO}_3$ )<sup>3-</sup> anions.

For a given *A-B-C-O* quaternary oxide convex hull, for each quaternary oxide, we enumerate all pairwise precursor combinations that can form these candidate target phases. In this study, we only considered candidate targets that fall on an isopleth between a pair of precursors. It is not generally the case that two precursors will be available for each target oxide. We exclude reactions that consider elemental  $\text{O}_2$  as a precursor. In the convex hull, each pairwise reaction corresponds to the slice plane between the pairwise precursors, which intersects the target. This approach determines all compositionally feasible pairwise reactions for the formation of all candidate quaternary oxide targets.

The list is further sieved by identifying reactions where the target material is the deepest point in the reaction convex hull (as calculated from the `interface_reactions` module). We also evaluate the *inverse hull energy* of each phase, defined as the energetic extent by which the target phase is below its neighboring stable phases in the convex hull. The Inverse Hull Energy is illustrated in **Figure S1** for the target  $\text{Li}_3\text{Sc}_2(\text{PO}_4)_3$  phase from the precursors  $\text{LiPO}_3 + \text{Sc}_2\text{O}_3$ . Of the two possible reactions that could form  $\text{Li}_3\text{Sc}_2(\text{PO}_4)_3$ , which are  $3\text{LiPO}_3 + \text{Sc}_2\text{O}_3 \rightarrow \text{Li}_3\text{Sc}_2(\text{PO}_4)_3$  and  $2\text{ScPO}_4 + \text{Li}_3\text{PO}_4 \rightarrow \text{Li}_3\text{Sc}_2(\text{PO}_4)_3$ , we hypothesize that  $3\text{LiPO}_3 + \text{Sc}_2\text{O}_3$  will be the best precursors, due to its large inverse hull energy.

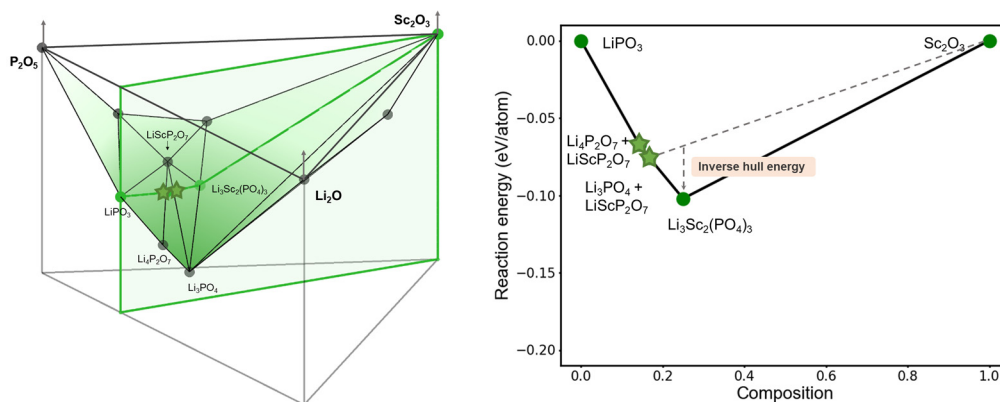


**Figure S1.** Reaction compound convex hull of  $\text{Li}_3\text{Sc}_2(\text{PO}_4)_3$ . **Left.)** the convex hull of  $\text{P}_2\text{O}_5$ ,  $\text{Sc}_2\text{O}_3$ , and  $\text{Li}_2\text{O}$ , where two kinks (green stars) represent the decomposition reactions that might happen at given compositions. The equilibrium phase is a 2-phase coexistence. The green slice plane corresponds to **Right.)**  $\text{LiPO}_3|\text{Sc}_2\text{O}_3$  convex hull.

The inverse hull energy is computed using the reaction convex hull from `interface_reactions`, where we identify the kinks in the convex hull that compete with the target compound. Because this is a 1-dimensional compositional intersection with a 3-dimensional quaternary phase diagram, the intersection can include critical compositions that correspond to single phases, or tie lines between 2 phases.

If the intersected tie line is the deepest point in the reaction convex hull, we anticipate the reaction will form the terminal phases of the tie line, such as green stars will decompose to  $\text{Li}_4\text{P}_2\text{O}_7 + \text{LiScP}_2\text{O}_7$  and  $\text{Li}_3\text{PO}_4 + \text{LiScP}_2\text{O}_7$  in **Figure S1**.

In executing this algorithm over the Li-, Na- and K- containing quaternary oxides, borates and phosphates, we identified 3104 reactions. We then determined the minimum set of precursors that would maximize the number of potential candidate reactions, whilst also considering the available precursors available on hand at Samsung. This process led to the target materials and precursor selections presented in this work.

When there were multiple precursor pairs that could be used to synthesize the target compound, we chose the final precursor pair by first prioritizing Principle 3, where the target compound was at the deepest point of the convex hull—this ensures that the thermodynamic driving force for nucleation of the target compound is greater than the driving forces to all other competing phases. We next prioritized Principle 5, where the target compound has the largest inverse hull energy. A reaction having a large inverse hull energy supersedes both Principle 2, the reaction energy (as illustrated by the discussion around Figure 2a) and Principle 4, number of competing phases – as the number of competing phases may not matter so much if the driving force to the target was much more significant than to the competing phases.

When there were multiple precursor pairs that could be used to synthesize the target compound, we chose the final precursor pair by first prioritizing Principle 3, where the target compound was at the deepest point of the convex hull. This ensures that the thermodynamic driving force for nucleation of the target compound is greater than the driving forces to all other competing phases. We next prioritized Principle 5, where the target compound has the largest inverse hull energy. A reaction having a large inverse hull energy supersedes both Principle 2, the reaction energy and Principle 4, number of competing phases. A large reaction driving force is not a sufficient criterion for synthesis; for example, in **Figure 2b** where the magnitude of the driving force of  $\text{Li}_2\text{O} + \text{Zn}_2\text{P}_2\text{O}_7 \rightarrow \text{LiZnPO}_4$  is large but selectivity may be weak compared to  $\text{ZnO} + \text{Li}_3\text{PO}_4$ . On the other hand, a large inverse hull energy means that the driving force from the competing phases to the target phase would be large, meaning that the *relative* driving force to the target phase is large, and even if competing phases did form, there would be a large driving force for a secondary reaction to form the target compound from any intermediate phases.

## S11.2. Precursor selection principles using chemical potential diagrams

In Todd *et al.*,<sup>1</sup> chemical potential diagrams are used to assess the selectivity of phases during solid-state synthesis. Here, we interpret our precursor selection principles, which are built from a convex hull representation, from the perspective of a chemical potential diagram.

The chemical potential diagram is a dual representation of the convex hull, meaning it offers an alternative perspective on the same geometric object (similar to how real space and reciprocal space are dual of each other). The chemical potential diagram can be built from the convex hull using the intercept rule, produced by tilting a tangent plane underneath a ternary convex hull, as illustrated in **Figure S2**. **Figure S3** shows for the Li-Zn-P-O system the convex hull, as well as its corresponding chemical potential diagram on  $\mu_{\text{Li}}$ ,  $\mu_{\text{Zn}}$ ,  $\mu_{\text{P}}$  axes (with fixed  $\mu_{\text{O}} = 0$ , corresponding to oxygen gas at ambient conditions). The phases that appear on the convex hull exactly correspond to the phases on the chemical potential diagrams. The three-phase coexistence *triangles* on the convex hull correspond to the three-phase coexistence *points* on the chemical potential diagram, while the single-phase *points* on the convex hull correspond to the single-phase *polygons* in the chemical potential diagram.

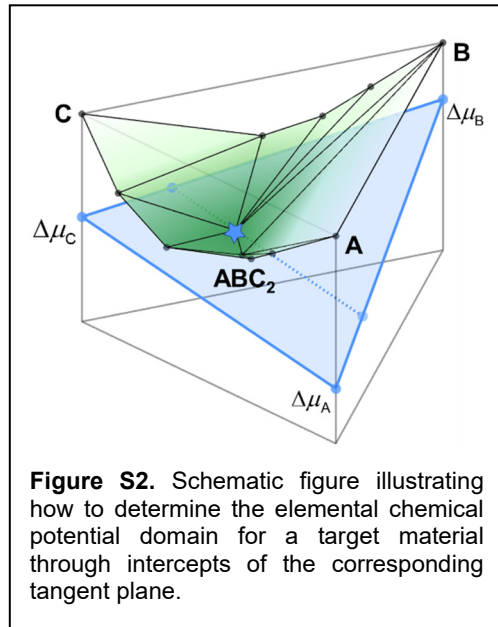


**Figure S2.** Schematic figure illustrating how to determine the elemental chemical potential domain for a target material through intercepts of the corresponding tangent plane.

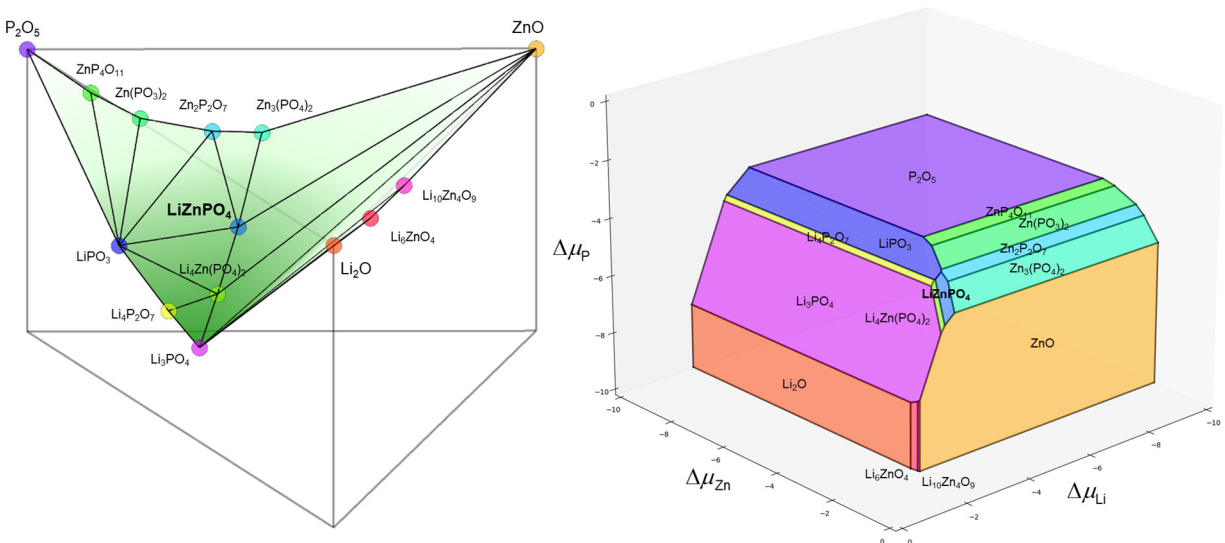


**Figure S3.** Comparison between convex hull and chemical potential diagram. Same phase is marked in the same color. Left) ZnO-P<sub>2</sub>O<sub>5</sub>-Li<sub>2</sub>O compound convex hull. Right) P-Zn-Al chemical potential diagram when  $\mu_{\text{O}}$  is fixed at -2 eV/atom.

**Figure S4** uses a model A-B system to show that the inverse hull energy of a phase is directly proportional to the size of its stability window on a chemical potential diagram. In **Figure S4a** we constructed a convex hull with a relatively deep inverse hull energy for  $A_3B_4$ , and a smaller inverse hull energy in **Figure S4c**; with the formation energies of all other phases held the same. This larger inverse hull energy from **S4a** corresponds to a wider chemical potential stability window for  $A_3B_4$  in both  $\mu_A$  and  $\mu_B$ , as shown by the intercept rule. In Figures **S4b,d** we show the size of the stability domain for  $A_3B_4$  on a chemical potential diagram. For the large inverse hull energy in **S4a**, we see a correspondingly larger chemical potential stability window for  $A_3B_4$  in **S4b**; and vice versa a smaller inverse hull energy in **S4c** results in a smaller chemical potential window in **S4d**. This size of the chemical potential window is similar to the ‘chemical potential distance’ metric presented in Todd *et al.*<sup>1</sup> In this sense, our selection of the inverse hull energy metric is comparable to the arguments from Todd *et al.*, in that both approaches indicate a stronger tendency for the target phase to form.

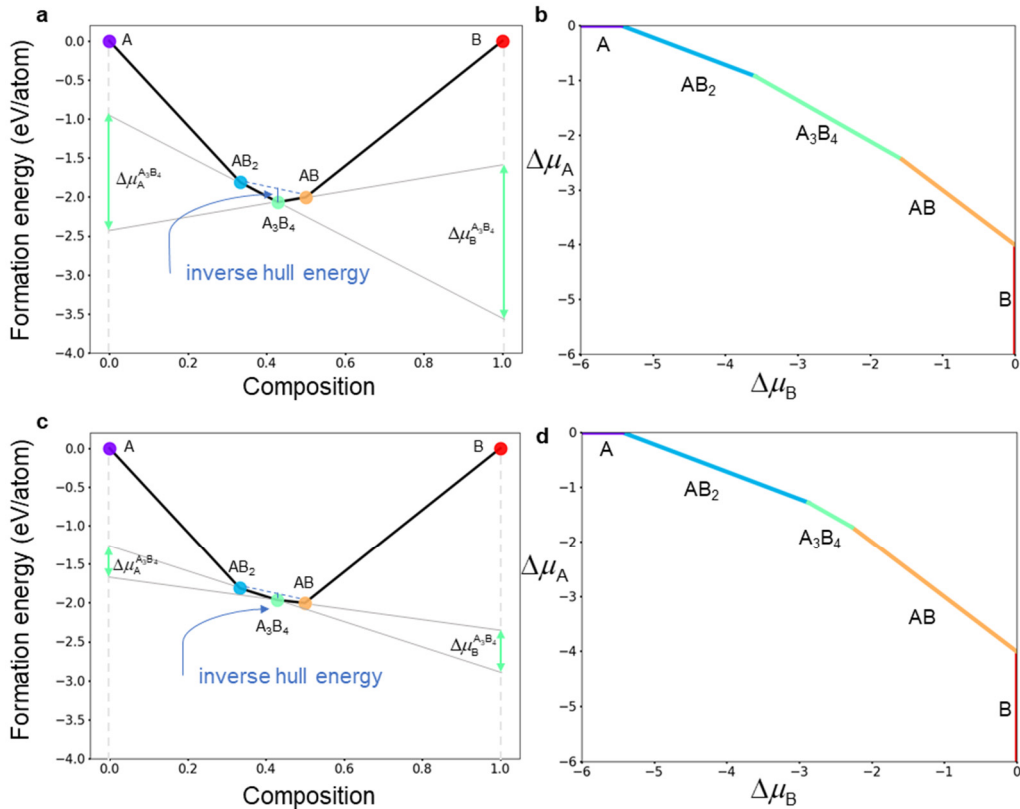


**Figure S4.** The relationship between inverse hull energy and chemical potential stability window of  $A_3B_4$ . The convex hull of A-B system with **a)** large, **c)** small inverse hull energy of  $A_3B_4$ , and the corresponding chemical potential diagram of A-B system with **b)** large, **d)** small inverse hull energy of  $A_3B_4$ . Larger inverse hull energy corresponds to larger size of chemical potential window.

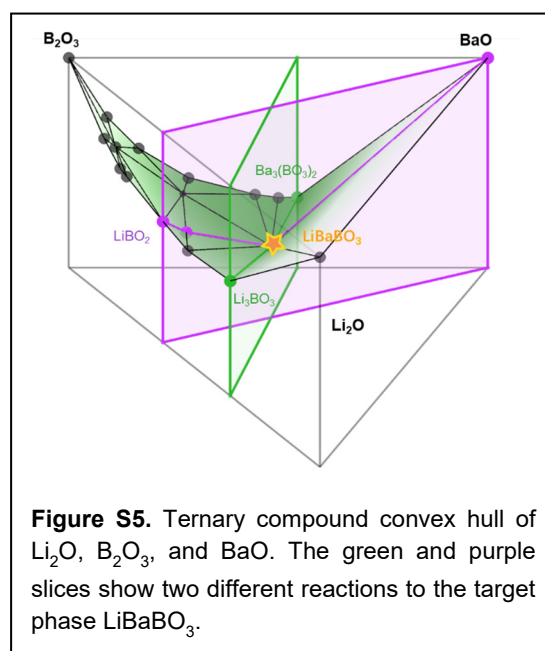
One disadvantage of chemical potential diagrams is that it is not straightforward to graphically illustrate stoichiometrically-balanced pairwise reactions on a chemical potential diagram. Take for example the  $\text{Li}_2\text{O} + \text{Zn}_2\text{P}_2\text{O}_7 \rightarrow \text{LiZnPO}_4$  reaction from manuscript **Figures 2a** and **2b**. It is very clear on the convex hull that there are 5 stoichiometrically-balanced reaction products on the  $\text{Li}_2\text{O} | \text{Zn}_2\text{P}_2\text{O}_7$  isopleth, including the phase-separated products  $\text{ZnO} + \text{Li}_3\text{PO}_4$ —which is in fact the product pair with the largest reaction energy. This fact is not very obvious on the chemical potential diagram from **Figure S3** above—where even though  $\text{ZnO}$  and  $\text{Li}_3\text{PO}_4$  have very large stability regions by themselves, on the chemical potential diagram their 2-phase coexistence is represented only by a phase boundary line, which looks like any other phase-boundary line on the chemical potential diagram.

For this reason, we elected to conduct our analyses from the convex hull perspective. By using the inverse hull energy metric, we capture the size of a stability region from a chemical potential diagram, however we also have the advantage of directly visualizing stoichiometrically-balanced reactions, as well as the driving force to form multi-phase mixtures.

### S11.3. Comparison against other synthesis prediction algorithms

Recently, Muratahan *et al.* [Manuscript Reference 32] devised a synthesis route prediction algorithm named PIRO, which is grounded in the principles of nucleation barrier assessment for the target phase on reactant surfaces, as well as the enumeration of competing phase occurrences. A lower nucleation barrier coupled with a reduced number of competing phases signifies an increased likelihood of the formation of the target phase. PIRO addresses a Pareto optimization problem to minimize the nucleation barrier and mitigate the competition from parasitic phases. In the case of BaLiBO<sub>3</sub>, PIRO suggests the best following reaction: 0.5 Ba + 0.5 Ba(BO<sub>2</sub>)<sub>2</sub> + Li + 0.5 O<sub>2</sub> → BaLiBO<sub>3</sub>. Our predicted precursors, BaO + LiBO<sub>2</sub> → BaLiBO<sub>3</sub>, is ranked as the 72<sup>nd</sup> best option in PIRO, and is accompanied by a nucleation barrier of 2.37 atomic units (64.49 eV) which is relatively large compared to other precursors. The main qualitative difference between PIRO and our algorithm is we impose a constraint on pairwise reactions, since reactions from multiple elementary precursors can often get kinetically trapped in low-energy intermediate reaction products.

McDermott *et al.* [Manuscript Reference 29] developed a graph-based network for the prediction of chemical reactions, where the graph data structure was constructed using a combination of phases within the convex hull as nodes, and reaction-energy-based descriptors as the weights of edges. Subsequently, pathfinding algorithms were employed to identify the lowest ‘cost’ from precursor nodes to target nodes, thereby predicting reaction pathways. For BaLiBO<sub>3</sub>, the optimal reaction recommended by McDermott *et al.*, is Ba<sub>3</sub>(BO<sub>3</sub>)<sub>2</sub> + Li<sub>3</sub>BO<sub>3</sub> → BaLiBO<sub>3</sub>, (green slice in **Figure S5**). The reaction energy and inverse hull energy values for this reaction is  $\Delta G_{\text{rxn}} = \Delta G_{\text{inv}} = -0.04$  eV/atom. On the other hand, our predicted reaction BaO + LiBO<sub>2</sub> → BaLiBO<sub>3</sub> has reaction energy and inverse hull energy values of  $\Delta G_{\text{rxn}} = -0.192$  eV/atom,  $\Delta G_{\text{inv}} = -0.153$  eV/atom.



## SI2. Robotic laboratory setup and procedures

### SI2.1. ASTRAL system overview

The ASTRAL platform developed at the Samsung Advanced Materials Lab (AML) is a robotic system designed to perform high-throughput automated synthesis of inorganic materials, in order to accelerate the research and development of new materials of technological interest. To the best of our knowledge, ASTRAL is the first robotic system that automates inorganic ceramic synthesis from powder precursors. To develop ASTRAL, we overcame major practical challenges in powder precursor processing, and the challenges and solutions in powder ceramic synthesis for automated laboratory are shown in **Table S1**.

The ASTRAL system is centered around a flexible collaborative robot arm mounted on a linear rail, which is able to perform dexterous manipulation tasks and transport samples throughout the system. Surrounding the central rail system are several stations that perform specialized tasks needed for the synthesis process, such as dispensing solid powder precursor chemicals, dispensing liquid chemicals, heat treatment to calcine and react precursors, and X-ray diffraction to characterize synthesis outcomes. The layout of the ASTRAL platform and robotic coverage area are illustrated in 3D-model of the system shown in **Figure S6**.

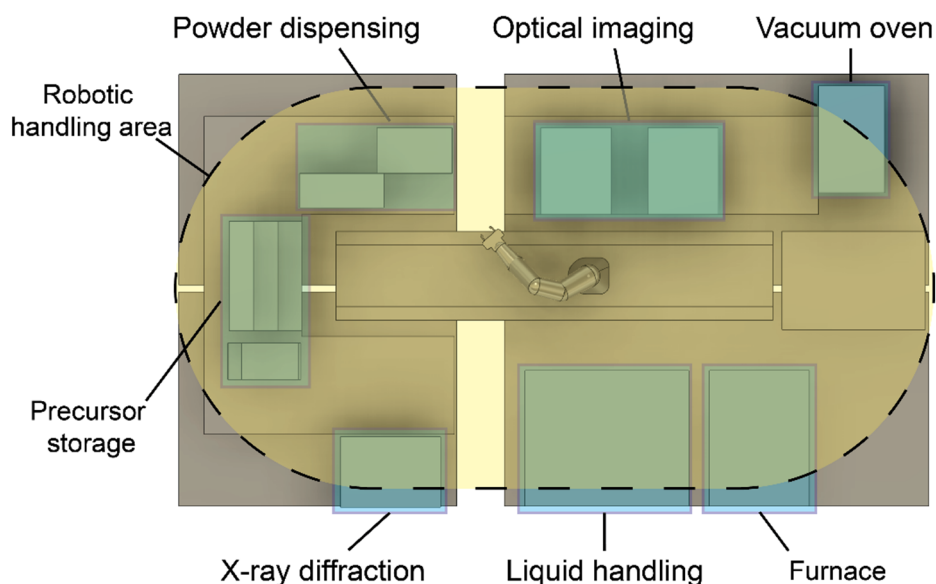


**Figure S6:** 3D-model of ASTRAL automated synthesis platform. Stations for storage, characterization, and synthesis operations, marked with blue rectangles, are arranged around the perimeter of the platform. The Panda robotic arm and rail in the center of the platform transports samples between stations throughout the robotic handling area marked in yellow.

#### SI2.1.1. Mobile robotic arm

Transport of samples between stations is accomplished by two robots, a 7-axis Panda robotic arm supplied by Franka Emika, and a linear rail supplied by Vention.io. The Panda arm is a highly flexible collaborative robot with a reach of 855mm and a payload of 3kg, with positional repeatability of 0.5mm allowing high reliability for manipulating small objects. The Panda arm is mounted on the linear rail system, which uses the Vention.io MachineMotion controller and a rack-and-pinion actuator to transport the arm over a linear distance of 2320mm, with positional repeatability of 0.1mm. By utilizing the rail system to extend the

range of the Panda arm, the system is able to accomplish highly precise generalized manipulation tasks over the approximately 1710mm x 4030mm area shown in **Figure S6**.

In addition to performing repeatable precise movements, the Panda arm is equipped with force and position sensors that allow it to detect collisions and allow it to apply controlled gentle force to objects that are being manipulated. This allows the robot to handle samples and interface with a wide variety of equipment in a manner similar to a human researcher. For example, the Panda arm can be used to press buttons, turn handles, and open doors without risk of damage, allowing the system to easily and safely interface with equipment that is designed for human use.

### SI2.1.2. Sample handling

Disposable 5mL glass test tubes (Corning) are used to hold precursors during dispensing, mixing, and vacuum drying. Alumina crucibles (Advalue Technology) are used to hold the mixed precursors during high temperature heat treatment. As the ASTRAL system is designed to accommodate handling of individual as well as trays of 8 or 24 sample holders, the platform uses a wide range of custom holders and adapters to enable reliable robotic handling, shown in **Figure S7**.

Sample holders intended for room temperature use are manufactured out of Acrylonitrile styrene acrylate (ASA), and utilize embedded magnets to reversibly and accurately locate parts during handling. In addition, aluminum plates are used to hold sets of 24 glass tubes during vacuum drying, and alumina plates are used to hold sets of 24 crucibles during high temperature heat treatment. All holder plates include a grip pad matching the geometry of the Panda arm grip surface to maximize the reliability of robotic handling.

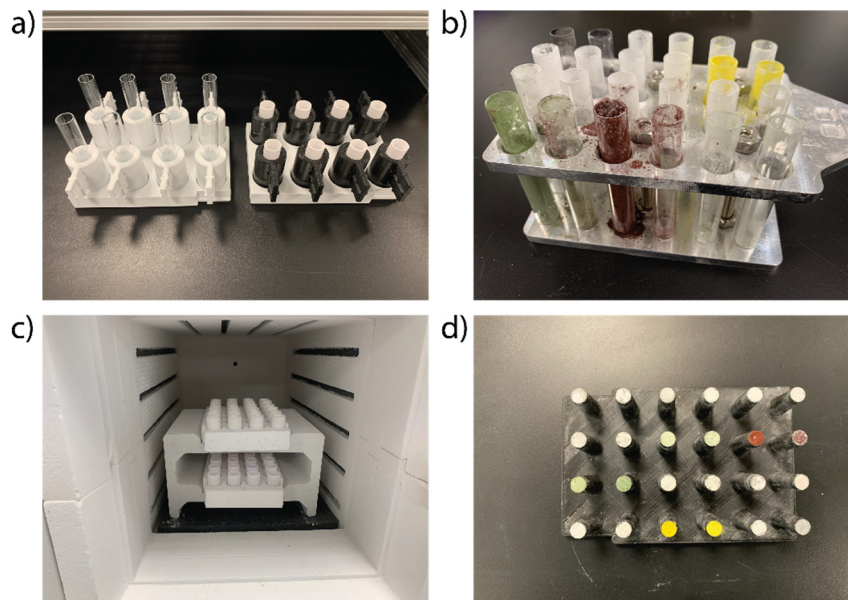


**Figure S7:** Custom holders used by ASTRAL platform for sample handling. All plates and individual holders have customized grip surfaces optimized for handling by the Panda robotic arm. (a) ASA plates holding 8 ASA sample holders, which each hold an individual glass test tube or alumina crucible. Both the plates and sample holders have embedded magnets to securely locate parts during robotic handling. (b) Aluminum plate holding 24 test tubes suitable for solvent mixing, wet chemistry, and heat treatment up to 250C. (c) Cast alumina plates holding 24 alumina crucibles, suitable for heat treatment up to 1200C. (d) ASA plate holding 24 stainless steel stubs with mounted powder samples for X-ray diffraction. Embedded magnets are used to hold the stubs in place during handling operations.

### SI2.1.3. Powder dispensing

The ASTRAL platform uses a Quantos solid dispensing unit, supplied by Mettler Toledo, to dispense the precursor powders used for synthesis experiments. The Quantos dispenser uses gravimetric dispensing to dose powders into sample containers, with fully automated operation enabled by an RS-232 interface. To accomplish the many-to-many dispensing required for synthesis experiments, the ASTRAL platform uses the Panda arm to sequentially load sample holders and precursor dosing heads into the Quantos dispenser to complete each dispense operation.

The ASTRAL platform includes storage for up to 63 separate powder precursor chemicals in the storage rack shown in **Figure S8a**. The precursor powders are stored in dosing heads designed to interface with the Quantos solid dispensing unit, supplied by Mettler Toledo. To facilitate handling by the Panda robot arm, the dosing heads are equipped with custom designed grip pads, which clamp securely onto the exterior and provide a reliable grip surface that the Panda uses to insert and retrieve dosing heads from the dispenser.

Powders are stored in dosing heads supplied by Mettler Toledo designed to interface with the Quantos powder dispenser. In order to facilitate handling using the Panda robot arm, the dosing heads are equipped with custom designed grip pads as indicated in **Figure S8b**, which clamp securely onto the exterior and provide an optimal shape for controlled handling by the gripper used by the Panda arm.

Powder dispensing presents several practical challenges, particularly due to the variability of physical characteristics such as particle sizes and flowability. We found that no single model of dosing head could successfully dispense all of the powders, but by selecting between three different models we are able to reliably dose all of the precursors. The full list of precursors used in this study, with associated dosing head and manufacturer information, is included in **Table S2**.

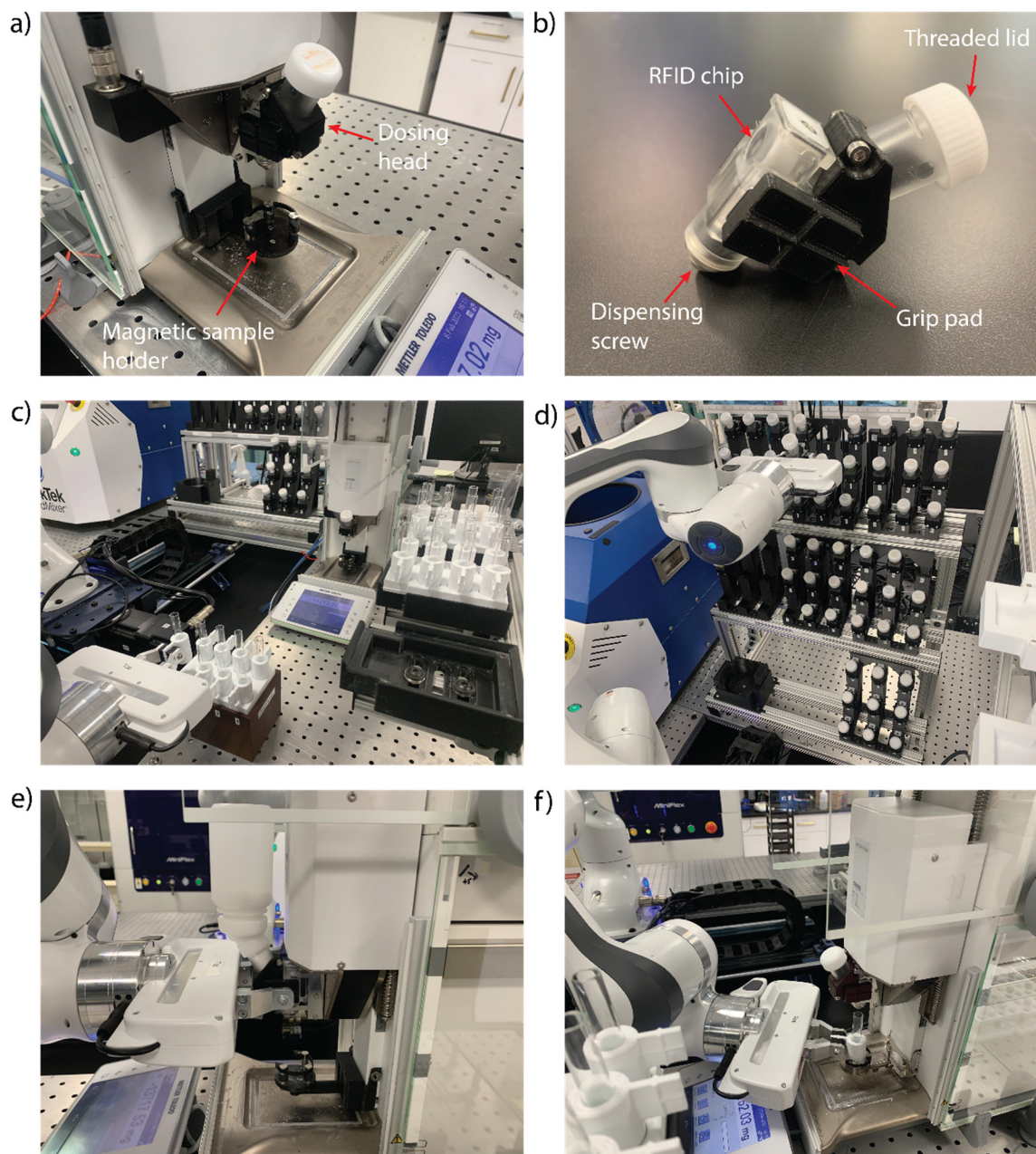


**Figure S8:** Components and workflow for the ASTRAL platform automated powder dispensing system. (a) Quantos powder dispenser, used for gravimetric dispensing of precursor powders. (b) Dosing head used by Quantos to store and dispense powders, with attached grip pad for Panda arm. (c) Powder dispensing station in use by ASTRAL to dose precursors into 24 glass sample holders. (d) Powder inventory with 63 storage slots for precursor dosing heads. (e) Panda arm loading dosing head into Quantos to prepare for precursor dispensing. (f) Panda arm loading sample holder into Quantos to receive dispensed powder.

#### SI2.1.4. Liquid handling

Dispensing of liquid solvents and precursor solutions is accomplished by a Freedom EVO 100 liquid handling robot, supplied by Tecan Life Sciences. The liquid handler uses a set of 8 reusable pipettes with

1mL solution capacity, mounted on a 3-axis gantry system to allow movement throughout the deck of the robot. The liquid handler employs the pipettes to aspirate and dispense liquids with 1 $\mu$ L accuracy from an installed storage rack containing 64 prepared solutions, allowing any arbitrary mixture of liquids to be added to samples. All containers are sealed with septum caps to allow pipetting operations while minimizing evaporation of stored liquids.

The Freedom EVO liquid handler is also equipped with an additional Pick and Place (PnP) arm, which is used for fast and accurate movement of small objects between containers on the deck of the liquid handler. In the ASTRAL platform, the PnP arm is used for robotic manipulation of objects that are too small to be accomplished by the Panda robot arm, such as individual test tubes, crucibles, and XRD sample holders.

While the ASTRAL platform is capable of using the liquid handler for a broad range of wet chemistry, in particular using Pechini method for inorganic sol-gel synthesis, in the present study the only liquid dispensed was 1.5mL of ethanol added to each sample to act as a milling solvent. The PnP arm was additionally used for all handling operations transferring individual crucibles, test tubes, and XRD sample stubs between holder plates.

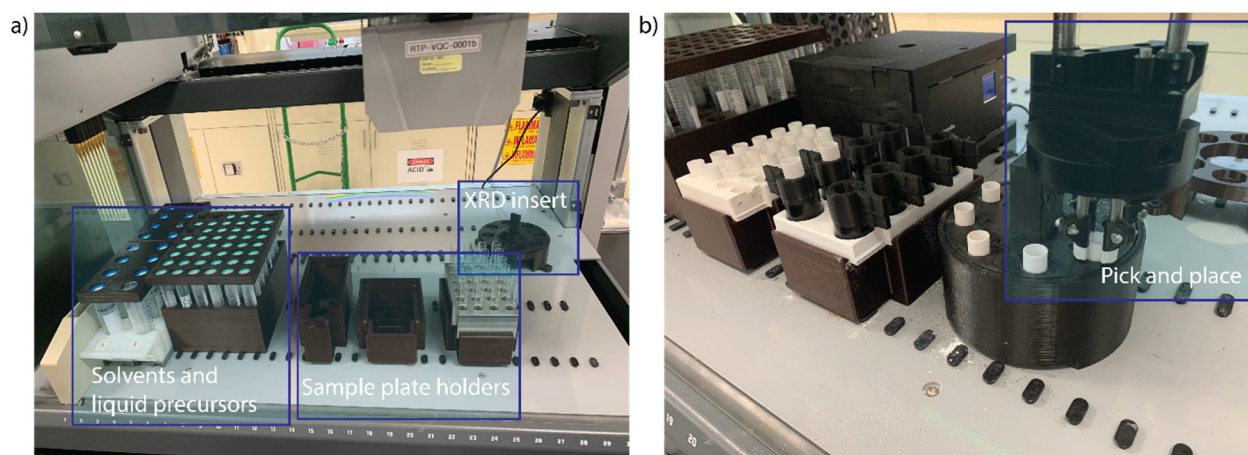


**Figure S9:** Freedom EVO 100 liquid handling robot installed in the ASTRAL platform. (a) Configuration of the deck of the liquid handler. The storage racks on the left hold 16 50mL Falcon tubes and 48 15mL Falcon tubes with solvents and liquid precursor chemicals for use in synthesis experiments. The holders on the right side of the deck are accessible for the Panda arm to place any of the holder plates for liquid dispensing or pick and place operations. (b) The liquid handler pick and place arm transferring crucibles between holder plates.

### SI2.1.5. Ball milling

Powder mixing in the ASTRAL platform is done by an SFM-2 rotary ball mill supplied by MTI Corporation, using 3mm stainless steel mixing balls to break up and mix powders contained inside sealed test tubes. At the time of writing, the powder mixing by the ASTRAL platform is not fully automated, but is instead accomplished using high-throughput handling methods that allow a human researcher to efficiently and reproducibly process batches of samples. The high-throughput ball milling system consists of (1) a specialized jig used to dispense a consistent number of mixing balls into 24 test tubes at a time, (2) customized inserts allowing groups of 8 samples to be mixed simultaneously in a single chamber of the mill, (3) a magnetic extraction tool to allow simultaneous removal of mixing balls from 8 samples at a time,

and (4) a customized funnel allowing simultaneous transfer of 24 samples from glass test tubes to alumina crucibles in preparation for heat treatment.

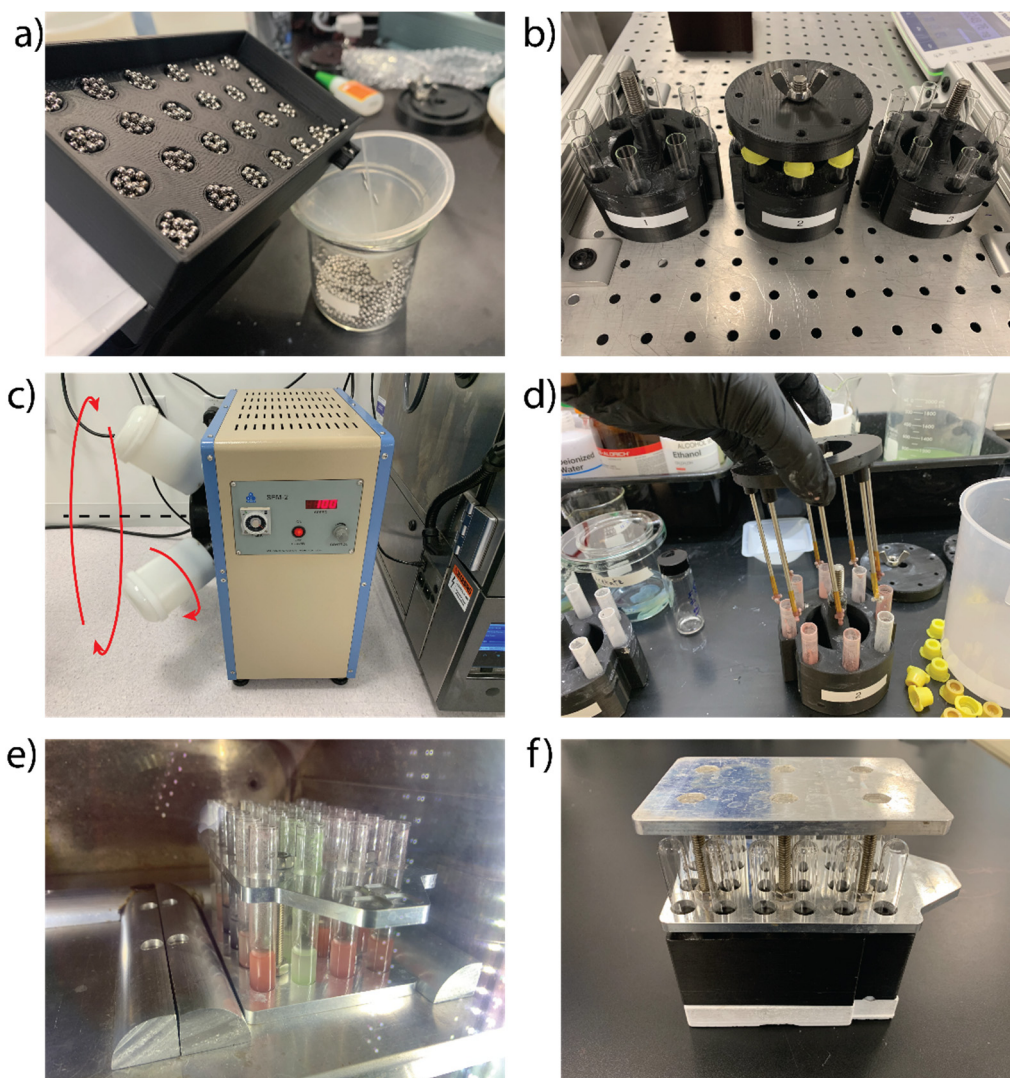


**Figure S10:** High-throughput ball milling for ASTRAL synthesis experiments. (a) Fixture for controlled dispensing of 3mm stainless steel mixing balls into plate of 24 glass tubes. (b) Custom inserts to hold 8 test tubes in a single chamber of the rotary mixer. (c) Mixing precursors in rotary ball mill. (d) Magnetic extraction of stainless steel mixing balls. (e) Vacuum drying for solvent removal. (f) Powder transfer from glass tubes to alumina crucibles via customized funnel plate.

#### SI2.1.6. Solvent removal

Sample drying and solvent removal is accomplished using a vacuum oven (Across International AT09e), with an attached diaphragm vacuum pump (Welch DryFast), with trays of samples loaded and unloaded using the Panda arm. The temperature controls for the vacuum oven are controlled automatically by the ASTRAL controller using Modbus communications over an RS485-USB interface. The gas intake for the vacuum chamber can be diverted between vacuum and intake of ambient air using an automated solenoid diverting valve actuated by a digital i/o module attached to the Vention MachineMotion controller. To allow gentle but fast solvent drying, throughout the drying process the intake valve is cycled between 120s

of vacuum and 10s of ambient air refill. The periodic refill cycles allow for efficient displacement and exhaust of accumulated solvent vapors, and decreases the chance of powders being expelled from test tubes due to overly aggressive solvent vaporization.

### SI2.1.7. High temperature heat treatment

High temperature calcination and heat treatment of samples is accomplished using a Nabertherm p480 box furnace, with a controllable temperature range of up to 1200C. Automated control of the heating profile by the Astral controller is done using a Modbus/TCP communication interface. Batches of samples are held in 12mm x 29mm alumina crucibles, loaded into alumina holder plates that can be handled by the Panda arm to transport samples in and out of the furnace, as illustrated in **Figure S11**.

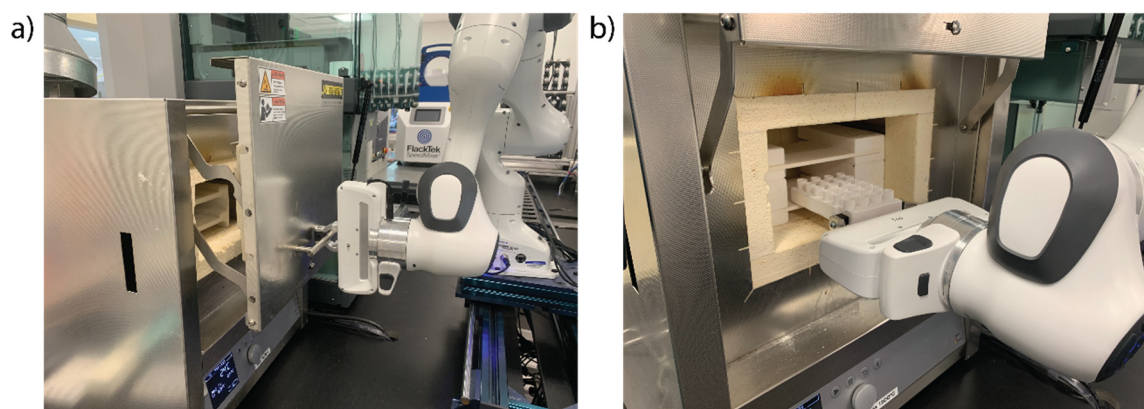


**Figure S11:** Heat treatment and calcination at up to 1200C using Nabertherm p480 box furnace. (a) Panda arm opening furnace door. (b) Panda arm loading tray of 24 samples into furnace for heat treatment.

### SI2.1.8. X-ray diffraction

The ASTRAL platform uses automated X-ray diffraction in order to characterize the outcome of synthesis experiments. As with the ball milling process, preparation for the X-ray diffraction requires some manual sample preparation by a human researcher, utilizing a high-throughput processing setup designed to produce high efficiency and consistent results. The high-throughput setup consists of (1) a plate containing 24 embedded stainless steel dowel pins, and (2) a matching plate with 24 posts, each containing an embedded magnet securing a matching stainless-steel stub, with a thin layer of vacuum grease applied to the top surface. In order to prepare samples for X-ray diffraction, the dowel plate is first pressed repeatedly into the crucible plate to break up the fired powders into small loose particles. Once the powders are broken up, the sample holder plate is inverted and pressed into the plate of powders, causing a thin layer of powder for each sample to adhere to the vacuum grease in a flat layer appropriate for X-ray diffraction. Sample holders and key process steps for the XRD sample preparation are illustrated in **Figure S12 (a-c)**.

Following the transfer of powders to the XRD holder, the remainder of the X-ray diffraction measurements are accomplished using fully automated robotic handling. To do this, each plate of 24 mounted samples is transported by the Panda arm to the deck of the liquid handler. The PnP arm is then used to transfer the next group of 8 samples into a custom insert designed to fit into the 8-sample changer used by the Rigaku Miniflex XRD. The insert is then loaded into the XRD, using the Panda robot arm to release the interlock, open the door, and transport the samples. The required measurements are then automatically set up and

executed, using the pyautogui python package to interface with the GUI of the Miniflex Guidance control software through simulated mouse and keyboard actions.

XRD patterns are taken from  $2\theta$  ranging from 10-70, however for the XRD figures plotted in SI.3 we only show  $2\theta$  ranging from 15-55, where the most XRD features are. If full range is shown, some of the important peak features become compressed and more difficult to see.

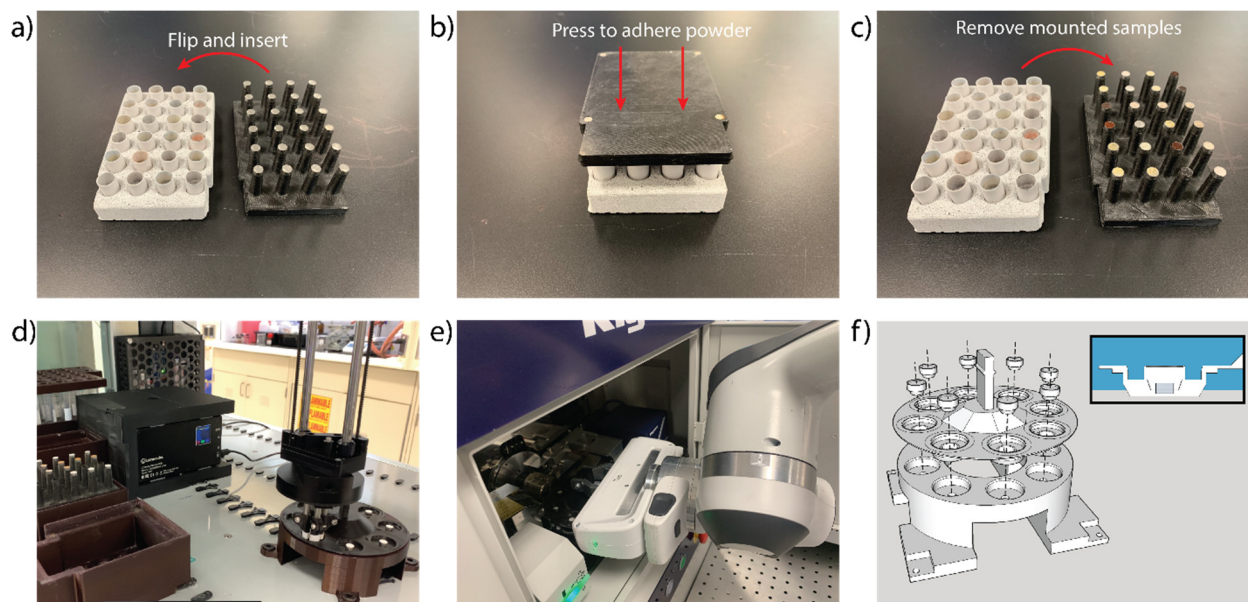


**Figure S12:** Workflow for characterization of synthesis outcomes by the ASTRAL platform via X-ray diffraction. (a-c) High-throughput preparation of powder samples for XRD. A thin layer of vacuum grease is applied to the stainless steel XRD stubs prior to pressing to allow a thin layer of calcined powder to adhere to the top surface. XRD stubs are secured to ASA holder plate during pressing operation by embedded magnets. (d) PnP arm transferring XRD stubs between holder plate and insert. (e) Panda arm transferring insert into XRD for measurement. (f) Design detail of XRD insert, showing magnetic holding system that is used to locate powder samples in XRD measurement plane.

## SI2.2. ASTRAL platform software implementation

### SI2.2.1. ASTRAL python controller

The ASTRAL platform manages the scheduling and control of robotic movements using central control software written in-house using python, with a graphical interface implemented through the PyQt5 package. The ASTRAL python controller uses a modular, multithreaded programming approach to permit simultaneous operation of any number of attached robots, with each robot controlled by a separate thread. The thread controlling each robot is responsible for receiving and executing commands and monitoring the status of the equipment.

For operation of multiple experiments in parallel, the ASTRAL controller uses a reservation system to allocate resources and avoid conflicts. For each experiment step, the controller determines which robots and inventory resources are required for execution, and will wait until all resources are available to begin. Once the process step has started, all required resources are reserved for the exclusive use of that experiment for the duration of the step, then released back to the pool of available resources.

The scheduling approach used by the ASTRAL platform allows parallel operation of multiple experiments, which is particularly critical for inorganic materials as synthesis methods typically require multiple days to complete. For example, during typical operation, the system will be dispensing powders for one plate of samples, while running heat treatment on a second and X-ray diffraction on a third, allowing the system to maintain maximum possible throughput without requiring human attention to avoid conflicts.

### SI2.2.2. Experiment planning

ASTRAL experiments are specified using a JSON format, which describes the experimental procedure as a series of general, human-readable steps, such as “Dispense powders”, “Mix”. For execution of each experiment, the JSON used as input by the ASTRAL controller to generate a list of all of the required robot tasks required to complete the specified experiment. The intention of the JSON format is to use a flexible, platform-independent specification that mimics the manner in which procedures are typically described in scientific literature. This enables a high level of flexibility and portability of the experiment plans, and acts analogously to a thorough and consistently formatted digital lab notebook.

Each experiment JSON contains specifications for running a synthesis experiment on a batch of up to 24 samples, which will be processed in parallel for mixing, heat treatment, and XRD. For each sample an independent target composition, yield, and list of precursors are provided, allowing preparation of 24 different mixtures. The appropriate quantities of each precursor to dispense for each sample are calculated using the pymatgen reaction\_calculator module to generate a balanced reaction from the specified precursors. For syntheses that use a heat treatment of 600C or more, it is assumed that volatile compounds such as CO<sub>2</sub>, H<sub>2</sub>O, and O<sub>2</sub> can be freely removed, and so the reaction calculator is adjusted to permit loss of these compounds when generating a balanced reaction from the precursor list.

### SI2.2.3. Automated XRD analysis

X-ray diffraction is the primary characterization method used by the ASTRAL platform to determine the outcome of synthesis experiments. Standard methods used for XRD analysis require two steps: (1) identification of phases present in the sample, and (2) pattern fitting through methods such as Rietveld refinement to quantify the lattice parameters and weight percent of the phases. The traditional method for phase identification is to compare collected XRD patterns to a database of reference structures such as the Inorganic Crystal Structure Database (ICSD), most often using a search-match algorithm to compare peak positions and determine likely matches. While this approach is very effective at detecting matches to known structures, it requires a human to review candidate structures to exclude false positives and select true matches. More recently, several research groups have presented machine learning algorithms that can be trained on a set of reference structures to identify phases in experimental XRD [Manuscript References 36, 37]. These machine learning approaches offers great potential for improving automated phase identification, but requires additional steps to construct an appropriate training data set consistent with the characteristics of the experimental setup and chemical spaces. The training of these machine-learning methods is also reported in Ref 36 to take up to 20 hours for a system, also requiring GPU-accelerated machines.

Given the 35 systems that we are investigating here, we were not able to use these machine-learning methods to fully quantify all impurity phases detected in XRD for all samples processed on the ASTRAL platform. However, some quantification of synthesis outcomes is necessary to efficiently analyze trends

over large data sets. Therefore, we have adopted a semi-quantitative approach to evaluating synthesis outcomes, based on Rietveld refinement of the XRD using only the crystal structure of the target material.

Rietveld refinement of data is accomplished using the BGMN kernel, with python scripts used for the automated generation of the necessary input files, execution of the Rietveld refinement via the command line, and extraction of the fitting data from the output files. The target structure is used as the sole input phase for the BGMN kernel, and as such, in an ideal case, the Rietveld refinement will split the XRD signal into components associated with the target phase, background, and residual. The fraction of the target phase can then be estimated by dividing the integrated intensity of the target phase by the combined intensity of the target phase and residual,  $I_{target}/(I_{target} + I_{residual})$ . In this work we considered values greater than 0.5 to be high purity, between 0.2 and 0.5 moderate purity, and less than 0.2 considered low purity.

For samples of low purity, where the peaks corresponding to the target phase are small in magnitude, the integration of co-aligned peaks for small peak heights can be difficult to ascribe precisely to the target phase (as opposed to noise). Therefore, the phase fraction characterized from our XRD result should primarily be interpreted quantitatively for purity greater than 0.2

To minimize the excess residual, for each sample the algorithm supplies a background XRD pattern taken on an empty sample holder, to increase the effectiveness of the BGMN background fitting. As the background differs slightly for different sample holders, this procedure is repeated for each of 16 XRD patterns for empty sample holders, and the lowest residual is used as the final value for the calculation.

The primary limitations of this method are: (1) it neglects the different scattering factors of the target and impurity phases, (2) it can underestimate phase fraction due to any components of the residual that are not associated with impurity phases, and (3) it can overestimate phase fraction due to incorrect fitting of peaks for the target phase to impurity peaks. Due to the possibility of false positives due to (3), a value of  $0.2 \times 10^6$  counts is used as a detection threshold, so the target phase is considered not detected for any samples where the target phase intensity is lower than this value.

Despite these potential limitations, we validated that our procedure produces adequate results on a wide range of data, and is suitably accurate for detecting successful or failed synthesis outcomes in the great majority of cases. To perform this validation, we used a set of 255 previously-obtained experimental XRD patterns collected using the ASTRAL platform for which all impurity phases were identified. We then compared our approach of calculating  $I_{target}/(I_{target} + I_{residual})$ , versus the fully Rietveld refined XRD phase fractions.

**Figure S13** shows a comparison of the XRD quantification results using both our semi-quantitative method described above and full quantitative Rietveld refinement. The color of the dots correspond to the weighted R-factor  $R_{wp}/R_{exp}$  returned by the BGMN kernel as a goodness-of-fit metric, with higher values indicating greater discrepancy between the theoretical and experimental curves. The semi-quantitative method produced an estimated phase fraction that was on average 22.9% lower than the full quantitative refinement, but otherwise the two measures produced good agreement with a root mean squared difference of 4.6%. Therefore, we consider that the phase purity estimates produced by the semi-quantitative method are likely to be conservative, but generally effective for discriminating synthesis outcomes within 10% accuracy.

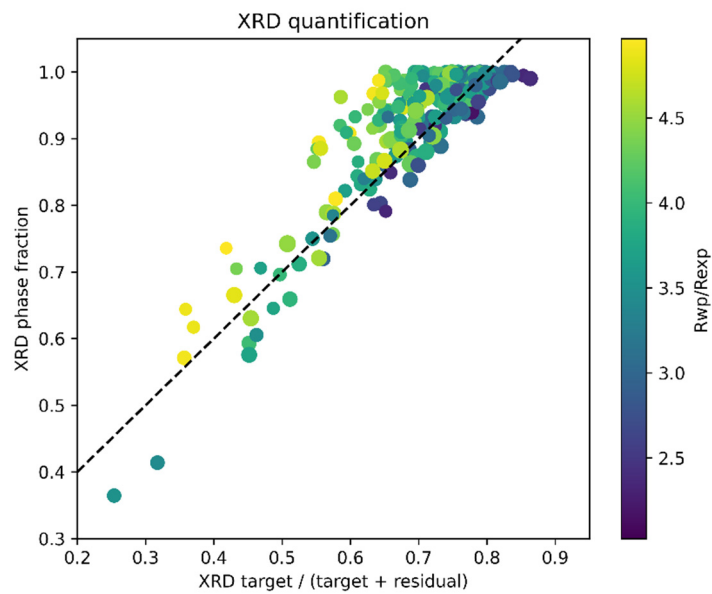


**Figure S13:** Comparison between semi-quantitative XRD analysis (x-axis) and full quantitative Rietveld refinement (y-axis) on a test data set of 255 samples synthesized on the ASTRAL platform. The size of the points is determined by the integrated XRD signal, while the color of the dots are determined by the quality-of-fit metric ( $R_{wp}/R_{exp}$ ) output by BGMN for the full Rietveld refinement.

#### SI2.2.4. Reproducibility Analysis

To examine the reproducibility of our ASTRAL experiments, we performed 153 replicate experiments, sampled for 20 different target compositions over 8 chemical systems and calcination temperatures ranging from 600-1200°C. We chose to sample a diverse set of reactions with both high yield and low yield of target compounds. We performed the replicate reactions using the same ASTRAL reaction conditions—including precursors, target composition, calcination temperature, and calcination time. However, we did not ensure that the crucibles were the same, as this may be a common source of laboratory variation. For each pair of replicate samples, the calculated fraction of the target phase was determined using the automated Rietveld refinement method described in **SI.2.2.3**.

The calculated phase fractions for each pair are shown in **Figure S14a**. The target phase fractions show a bimodal distribution, with the majority of results falling either above 0.5 for a successful synthesis, or below 0.2 for an unsuccessful synthesis outcome. In the majority of cases the phase fractions are close to the dashed guide line, which would indicate perfect reproducibility, though some deviation is observed, particularly in the low purity range where the synthesis conditions may be marginal for a particular compound. The distribution of the differences between the phase purities of the replicate samples is shown in **Figure S14b**. The absolute phase purity reproducibility error was centered around zero (mean = -0.6% difference in phase purity), with a standard deviation of 7.6%. We found that 79.7% of replicate experiments achieved an XRD-characterized purity result within the 10% phase purity threshold as we used in this study.

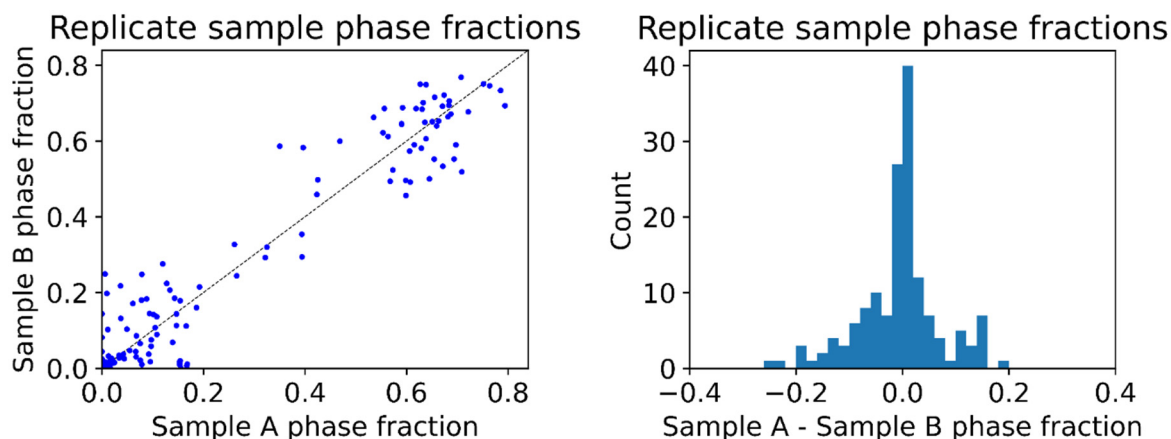


**Figure S14.** Reproducibility analysis on replicate samples for the ASTRAL platform (a) Calculated target phase fractions for pairs of replicate samples. (b) Distribution of the difference in calculated phase fractions between each pair of replicates.

## SI2.3. Challenges and solutions of automated powder ceramic synthesis

**Table S1:** Problems of powder ceramic synthesis for automated laboratory and our solutions.

Challenges	Solutions
Powders are difficult to handle for automated dispensing due to varying size and physical properties	The ASTRAL platform using a Quantos powder dispenser supplied by Mettler Toledo, which uses gravimetric dispensing to dose precursor powders with high accuracy. To accommodate broad variety of powder types needed for synthesis experiments, each precursor powder is assigned one of three models of dosing heads for reliable dispensing.
Hygroscopic precursors	For handling hygroscopic precursors, we use the Quantos dosing heads for short-term storage, tightly sealed to minimize moisture infiltration. Hygroscopic powders are replaced on a schedule to maintain the quality of the dispensed precursors.
Powders are much more difficult to mix than liquid precursors	<p>Successful synthesis requires that precursors are mixing intimately and homogeneously before heat treatment to produce a uniform and consistent product.</p> <p>The ASTRAL platform accomplishes mixing of powders using a high-throughput ball milling system, consisting of the following components:</p> <ul style="list-style-type: none"> <li>• High-throughput dispensing of mixing balls</li> <li>• Automated addition of milling solvent</li> <li>• High-throughput milling holders</li> <li>• Magnetic mixing ball extraction</li> <li>• High-throughput powder transfer to crucibles using funnel plate</li> </ul>
Powders react and/or fuse with crucibles during high temperature heat treatment	<p>During high-temperature calcination, many precursors or reaction products may become molten, and react with the alumina crucible, resulting in contamination with aluminum and/or fusing of the sample to the crucible walls.</p> <p>We apply a boron nitride coating to the alumina crucibles for materials that are susceptible to this behavior. The boron nitride coating is highly non-reactive and resists wetting by most molten oxides, minimizing reactivity and fusing between the samples and crucibles.</p>
Difficulties in preparing and mounting powders for XRD characterization	<p>It is challenging to automate preparation of powders for characterization, due to varying physical properties and lack of a solvent to assist with dispersal.</p> <p>To address this, the ASTRAL platform performs characterization using a high-throughput system for XRD measurement, consisting of:</p> <ul style="list-style-type: none"> <li>• Custom magnetic sample stubs for XRD measurements</li> <li>• High-throughput mounting of powders onto XRD stubs by full plate</li> <li>• Fully automated robotic XRD loading and measurement execution</li> </ul>

**Table S2:** List of precursor chemicals and associated Quantos dosing heads stored in the ASTRAL inventory

<b>Formula</b>	<b>CAS number</b>	<b>Dosing head</b>	<b>Distributor</b>	<b>Purity</b>
Al <sub>2</sub> O <sub>3</sub>	1344-28-1	QH012-LNLX	Sigma Aldrich	99.99%
B <sub>2</sub> O <sub>3</sub>	1303-86-2	QH012-LNMW	Sigma Aldrich	99%
Bi <sub>2</sub> O <sub>3</sub>	1304-76-3	QH012-LNLT	Alfa Aesar	99.9%
BaO	1304-28-5	QH012-LNMW	Alfa Aesar	99.5%
CaO	1305-78-8	QH012-LNMW	Alfa Aesar	99%
CuO	1317-38-0	QH012-LNMW	Acros Organics	99%
Fe <sub>2</sub> O <sub>3</sub>	1309-37-1	QH012-LNLT	Alfa Aesar	99.9%
GeO <sub>2</sub>	1310-53-8	QH012-LNMW	Alfa Aesar	99.999%
In <sub>2</sub> O <sub>3</sub>	1312-43-2	QH012-LNMW	Thermo Fisher	99.99%
K <sub>2</sub> CO <sub>3</sub>	584-08-7	QH012-LNLT	Alfa Aesar	99%
K <sub>3</sub> PO <sub>4</sub>	7778-53-2	QH012-LNMW	Alfa Aesar	99%
KNbO <sub>3</sub>	12030-85-2	QH012-LNMW	Strem Chemicals	99.999%
KPO <sub>3</sub>	7790-53-6	QH012-LNLT	Strem Chemicals	98%
Li <sub>2</sub> CO <sub>3</sub>	554-13-2	QH012-LNMW	Alfa Aesar	99%
Li <sub>2</sub> TiO <sub>3</sub>	12031-82-2	QH012-LNMW	Sigma Aldrich	99%
LiBO <sub>2</sub>	13453-69-5	QH012-LNMW	Alfa Aesar	99%
LiNbO <sub>3</sub>	12031-63-9	QH012-LNMW	Alfa Aesar	99.99%
LiPO <sub>3</sub>	13762-75-9	QH012-LNLT	American Elements	99%
MgO	1309-48-4	QH012-LNMW	Sigma Aldrich	99%
MnO	1344-43-0	QH012-LNMW	Alfa Aesar	99.99%
Na <sub>2</sub> CO <sub>3</sub>	497-19-8	QH012-LNMW	Alfa Aesar	98%
NaBO <sub>2</sub>	10555-76-7	QH012-LNMW	Alfa Aesar	98%
NaPO <sub>3</sub>	68915-31-1	QH012-LNMW	Acros Organics	99%
Nb <sub>2</sub> O <sub>5</sub>	1313-96-8	QH012-LNMW	Sigma Aldrich	99.99%
NH <sub>4</sub> H <sub>2</sub> PO <sub>4</sub>	7722-76-1	QH012-LNMW	Alfa Aesar	99%
NiO	1313-99-1	QH012-LNMW	Alfa Aesar	99%
Pr <sub>6</sub> O <sub>11</sub>	12037-29-5	QH012-LNMW	Sigma Aldrich	99.9%
Sc <sub>2</sub> O <sub>3</sub>	12060-08-1	QH012-LNMW	Sigma Aldrich	99.9.%
SiO <sub>2</sub>	60676-86-0	QH012-LNMW	Sigma Aldrich	99.5%
SrO	1314-11-0	QH012-LNMW	Sigma Aldrich	99.9%
Ta <sub>2</sub> O <sub>5</sub>	1314-61-0	QH012-LNLT	Sigma Aldrich	99%
TiO <sub>2</sub>	1317-80-2	QH012-LNLT	Alfa Aesar	99.5%
V <sub>2</sub> O <sub>3</sub>	1314-34-7	QH012-LNMW	Alfa Aesar	95%
WO <sub>3</sub>	1314-35-8	QH012-LNLT	Sigma Aldrich	99.9%
Y <sub>2</sub> O <sub>3</sub>	1314-36-9	QH012-LNMW	Sigma Aldrich	99.99%
ZnO	1314-13-2	QH012-LNLT	Acros Organics	99.5%

### SI3. Synthesis result analysis

We summarize the synthesis recipes and results for both traditional and predicted reactions in 35 systems we synthesized in **Table S3**. The reaction energy and inverse hull energy of each predicted reaction is shown in **Figure S15**. The details of the synthesis for each system are also provided. For each system, we prepare four sections of data, 1) traditional precursors reaction compound convex hull; 2) predicted precursors reaction compound convex hull; 3) XRD results of traditional and predicted synthesis; 4) Table of phase fraction of traditional and predicted synthesis.

#### SI3.1. Summary of synthesis recipes and results

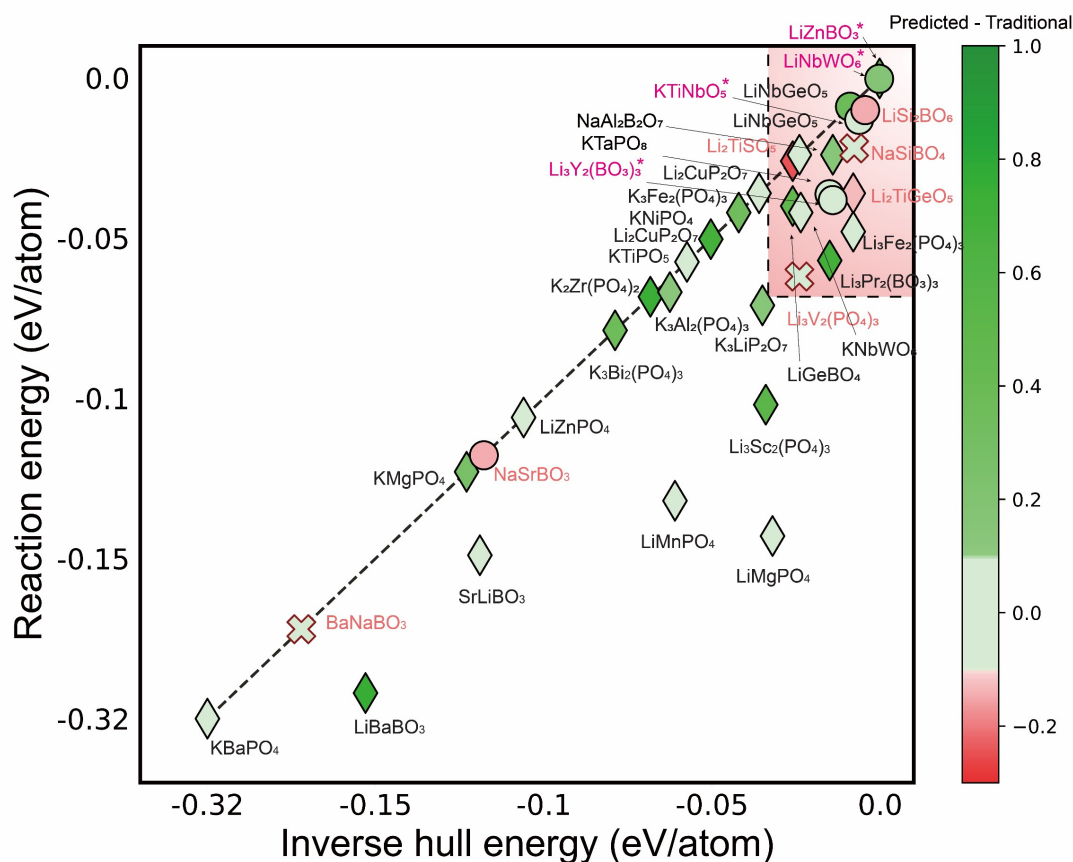


**Figure S15:** Labeled plot of reaction energy and inverse hull energy for all targets. Marker shape corresponds to best phase purity of predicted precursors, where diamonds are high purity, circles are moderate and low purity, and crosses with red outline means both predicted precursors and traditional precursors failed. Targets with magenta color star are metastable materials. Same color scheme is used in b, c, d. The dashed line represents when inverse hull energy equals reaction energy.

**Table S3.** Traditional and predicted precursors for different targets. The colors in the first four columns represent shows how much better the predicted precursors over traditional, where green means predicted precursors perform better, light green means they perform similarly, and red means traditional precursors perform slightly better. The color in the “Best predicted Synthesis” column represents what is the best phase purity the predicted precursors can get, where green means high phase purity, light blue means moderate purity, yellow means low purity, and gray means what traditional and predicted precursors failed with no XRD signal. The “Best Temperature” column shows the reaction temperature to get the best synthesis results using predicted precursors. The last two columns show the inverse hull energies and reaction energies for predicted precursors.

	Target	Traditional Precursors	Predicted Precursors	Best Predicted Synthesis	Best Temperature (C)	For predicted precursors (eV/atom) Inverse hull energy	Reaction Energy
1	BaLiBO <sub>3</sub>	Li <sub>2</sub> CO <sub>3</sub> , B <sub>2</sub> O <sub>3</sub> , BaO	BaO, LiBO <sub>2</sub>		800	-0.153	-0.192
2	K <sub>2</sub> Zr(PO <sub>4</sub> ) <sub>2</sub>	K <sub>2</sub> CO <sub>3</sub> , NH <sub>4</sub> H <sub>2</sub> PO <sub>4</sub> , ZrO <sub>2</sub>	KPO <sub>3</sub> , ZrO <sub>2</sub>		800	-0.068	-0.068
3	Li <sub>3</sub> Pr <sub>2</sub> (BO <sub>3</sub> ) <sub>3</sub>	Li <sub>2</sub> CO <sub>3</sub> , B <sub>2</sub> O <sub>3</sub> , Pr <sub>6</sub> O <sub>11</sub>	LiBO <sub>2</sub> , Pr <sub>6</sub> O <sub>11</sub>	High purity	600	-0.015	-0.057
4	KNiPO <sub>4</sub>	K <sub>2</sub> CO <sub>3</sub> , NH <sub>4</sub> H <sub>2</sub> PO <sub>4</sub> , NiO	KPO <sub>3</sub> , NiO		800	-0.050	-0.050
5	Li <sub>3</sub> Sc <sub>2</sub> (PO <sub>4</sub> ) <sub>3</sub>	Sc <sub>2</sub> O <sub>3</sub> , Li <sub>2</sub> CO <sub>3</sub> , NH <sub>4</sub> H <sub>2</sub> PO <sub>4</sub>	Sc <sub>2</sub> O <sub>3</sub> , LiPO <sub>3</sub>		900	-0.034	-0.102
6	LiGeBO <sub>4</sub>	Li <sub>2</sub> CO <sub>3</sub> , B <sub>2</sub> O <sub>3</sub> , GeO <sub>2</sub>	LiBO <sub>2</sub> , GeO <sub>2</sub>		800	-0.026	-0.040
7	KLi(PO <sub>3</sub> ) <sub>2</sub>	Li <sub>2</sub> CO <sub>3</sub> , K <sub>2</sub> CO <sub>3</sub> , NH <sub>4</sub> H <sub>2</sub> PO <sub>4</sub>	LiPO <sub>3</sub> , KPO <sub>3</sub>	Moderate	800	-0.009	-0.009
8	LiNbWO <sub>6</sub>	Li <sub>2</sub> CO <sub>3</sub> , Nb <sub>2</sub> O <sub>5</sub> , WO <sub>3</sub>	LiNbO <sub>3</sub> , WO <sub>3</sub>	Low purity	700	0.000	0.000
9	LiZnBO <sub>3</sub>	Li <sub>2</sub> CO <sub>3</sub> , ZnO, B <sub>2</sub> O <sub>3</sub>	LiBO <sub>2</sub> , ZnO		700	0.000	0.000
10	K <sub>3</sub> Fe <sub>2</sub> (PO <sub>4</sub> ) <sub>3</sub>	K <sub>2</sub> CO <sub>3</sub> , NH <sub>4</sub> H <sub>2</sub> PO <sub>4</sub> , Fe <sub>2</sub> O <sub>3</sub>	KPO <sub>3</sub> , Fe <sub>2</sub> O <sub>3</sub>		700	-0.042	-0.042
11	KMgPO <sub>4</sub>	K <sub>2</sub> CO <sub>3</sub> , NH <sub>4</sub> H <sub>2</sub> PO <sub>4</sub> , MgO	MgO, KPO <sub>3</sub>		800	-0.123	-0.123
12	K <sub>3</sub> Bi <sub>2</sub> (PO <sub>4</sub> ) <sub>3</sub>	K <sub>2</sub> CO <sub>3</sub> , NH <sub>4</sub> H <sub>2</sub> PO <sub>4</sub> , Bi <sub>2</sub> O <sub>3</sub>	Bi <sub>2</sub> O <sub>3</sub> , KPO <sub>3</sub>		700	-0.079	-0.079
13	K <sub>3</sub> LiP <sub>2</sub> O <sub>7</sub>	Li <sub>2</sub> CO <sub>3</sub> , NH <sub>4</sub> H <sub>2</sub> PO <sub>4</sub> , K <sub>2</sub> CO <sub>3</sub>	LiPO <sub>3</sub> , K <sub>3</sub> PO <sub>4</sub>		700	-0.035	-0.071
14	Na <sub>2</sub> Al <sub>2</sub> B <sub>2</sub> O <sub>7</sub>	Na <sub>2</sub> CO <sub>3</sub> , Al <sub>2</sub> O <sub>3</sub> , B <sub>2</sub> O <sub>3</sub>	Al <sub>2</sub> O <sub>3</sub> , NaBO <sub>2</sub>		700	-0.014	-0.024
15	K <sub>3</sub> Al <sub>2</sub> (PO <sub>4</sub> ) <sub>3</sub>	K <sub>2</sub> CO <sub>3</sub> , NH <sub>4</sub> H <sub>2</sub> PO <sub>4</sub> , Al <sub>2</sub> O <sub>3</sub>	KPO <sub>3</sub> , Al <sub>2</sub> O <sub>3</sub>		700	-0.063	-0.067
16	Li <sub>2</sub> CuP <sub>2</sub> O <sub>7</sub>	Li <sub>2</sub> CO <sub>3</sub> , NH <sub>4</sub> H <sub>2</sub> PO <sub>4</sub> , CuO	LiPO <sub>3</sub> , CuO	High purity	700	-0.036	-0.036
17	LiNbGeO <sub>5</sub>	GeO <sub>2</sub> , Li <sub>2</sub> CO <sub>3</sub> , Nb <sub>2</sub> O <sub>5</sub>	GeO <sub>2</sub> , LiNbO <sub>3</sub>		1000	-0.024	-0.024
18	Li <sub>3</sub> Fe <sub>2</sub> (PO <sub>4</sub> ) <sub>3</sub>	Li <sub>2</sub> CO <sub>3</sub> , NH <sub>4</sub> H <sub>2</sub> PO <sub>4</sub> , Fe <sub>2</sub> O <sub>3</sub>	LiPO <sub>3</sub> , Fe <sub>2</sub> O <sub>3</sub>		700	-0.008	-0.048
19	SrLiBO <sub>3</sub>	Li <sub>2</sub> CO <sub>3</sub> , B <sub>2</sub> O <sub>3</sub> , SrO	LiBO <sub>2</sub> , SrO		600	-0.119	-0.149
20	KNbWO <sub>6</sub>	K <sub>2</sub> CO <sub>3</sub> , Nb <sub>2</sub> O <sub>5</sub> , WO <sub>3</sub>	WO <sub>3</sub> , KNbO <sub>3</sub>		800	-0.024	-0.042
21	LiMgPO <sub>4</sub>	Li <sub>2</sub> CO <sub>3</sub> , NH <sub>4</sub> H <sub>2</sub> PO <sub>4</sub> , MgO	LiPO <sub>3</sub> , MgO		800	-0.032	-0.143
22	LiZnPO <sub>4</sub>	Li <sub>2</sub> CO <sub>3</sub> , NH <sub>4</sub> H <sub>2</sub> PO <sub>4</sub> , ZnO	LiPO <sub>3</sub> , ZnO		800	-0.106	-0.106
23	KBaPO <sub>4</sub>	K <sub>2</sub> CO <sub>3</sub> , NH <sub>4</sub> H <sub>2</sub> PO <sub>4</sub> , BaO	KPO <sub>3</sub> , BaO		700	-0.316	-0.316
24	KTiPO <sub>5</sub>	K <sub>2</sub> CO <sub>3</sub> , NH <sub>4</sub> H <sub>2</sub> PO <sub>4</sub> , TiO <sub>2</sub>	TiO <sub>2</sub> , KPO <sub>3</sub>		800	-0.057	-0.057
25	LiMnPO <sub>4</sub>	Li <sub>2</sub> CO <sub>3</sub> , NH <sub>4</sub> H <sub>2</sub> PO <sub>4</sub> , MnO	LiPO <sub>3</sub> , MnO		700	-0.061	-0.132
26	KTa <sub>2</sub> PO <sub>8</sub>	K <sub>2</sub> CO <sub>3</sub> , NH <sub>4</sub> H <sub>2</sub> PO <sub>4</sub> , Ta <sub>2</sub> O <sub>5</sub>	KPO <sub>3</sub> , Ta <sub>2</sub> O <sub>5</sub>		700	-0.015	-0.036
27	Li <sub>3</sub> Y <sub>2</sub> (BO <sub>3</sub> ) <sub>3</sub>	Li <sub>2</sub> CO <sub>3</sub> , Y <sub>2</sub> O <sub>3</sub> , B <sub>2</sub> O <sub>3</sub>	LiBO <sub>2</sub> , Y <sub>2</sub> O <sub>3</sub>	Low purity	700	-0.014	-0.038
28	KTiNbO <sub>5</sub>	K <sub>2</sub> CO <sub>3</sub> , TiO <sub>2</sub> , Nb <sub>2</sub> O <sub>5</sub>	TiO <sub>2</sub> , KNbO <sub>3</sub>		700	-0.006	-0.013
29	BaNaBO <sub>3</sub>	Na <sub>2</sub> CO <sub>3</sub> , BaO, B <sub>2</sub> O <sub>3</sub>	BaO, NaBO <sub>2</sub>		600	-0.172	-0.172
30	Li <sub>3</sub> V <sub>2</sub> (PO <sub>4</sub> ) <sub>3</sub>	Li <sub>2</sub> CO <sub>3</sub> , NH <sub>4</sub> H <sub>2</sub> PO <sub>4</sub> , V <sub>2</sub> O <sub>3</sub>	LiPO <sub>3</sub> , V <sub>2</sub> O <sub>3</sub>	Not detected	900	-0.024	-0.062
31	NaSiBO <sub>4</sub>	Na <sub>2</sub> CO <sub>3</sub> , SiO <sub>2</sub> , B <sub>2</sub> O <sub>3</sub>	SiO <sub>2</sub> , NaBO <sub>2</sub>		600	-0.008	-0.022
32	Li <sub>2</sub> TiGeO <sub>5</sub>	GeO <sub>2</sub> , Li <sub>2</sub> CO <sub>3</sub> , TiO <sub>2</sub>	GeO <sub>2</sub> , Li <sub>2</sub> TiO <sub>3</sub>	High purity	1000	-0.008	-0.036
33	Li <sub>2</sub> TiSiO <sub>5</sub>	SiO <sub>2</sub> , TiO <sub>2</sub> , Li <sub>2</sub> CO <sub>3</sub>	SiO <sub>2</sub> , Li <sub>2</sub> TiO <sub>3</sub>		1000	-0.026	-0.026
34	NaSrBO <sub>3</sub>	Na <sub>2</sub> CO <sub>3</sub> , SrO, B <sub>2</sub> O <sub>3</sub>	SrO, NaBO <sub>2</sub>		700	-0.118	-0.118
35	LiSi <sub>2</sub> BO <sub>6</sub>	Li <sub>2</sub> CO <sub>3</sub> , SiO <sub>2</sub> , B <sub>2</sub> O <sub>3</sub>	LiBO <sub>2</sub> , SiO <sub>2</sub>	Moderate	700	-0.004	-0.010

### SI3.2. Metastable materials synthesis efficacy

In this work, we also considered 4 target materials that are calculated in DFT to be metastable relative to the convex hull, meaning they have an energy above the hull. These metastable materials are listed in **Table S4**. We aimed to investigate if the materials were calculated to be metastable, if they were still synthesizable using predicted precursors. We chose  $\text{LiZnBO}_3$ , which is calculated in DFT to be metastable with respect to our predicted precursors  $\text{ZnO} + \text{LiBO}_2$ . We also chose  $\text{LiNbWO}_6$ ,  $\text{KTiNbO}_5$ , and  $\text{Li}_3\text{Y}_2(\text{BO}_3)_3$ , which are metastable with respect to decomposition products that are not our precursors. We hypothesized that by starting with precursors that are in a different ‘compositional direction’, we might be able to synthesize these metastable phases. To determine the predicted precursors for these metastable compounds, we constructed artificial entries for these compositions, but with an energy slightly smaller than the existing convex hull energy at that composition. For this work, we chose an arbitrary value of  $\Delta E_{\text{hull}} = -0.01$  eV.

Of these four systems, we obtained a reasonably high target yield for  $\text{LiZnBO}_3$ , whereas the three metastable targets received low yields from both the predicted and traditional precursors. All three metastable materials were synthesized with low sample purity, ostensibly within the noise of the XRD characterization method. This illustrates that our algorithm is better suited to predict precursors for target materials that are convex hull stable, rather than metastable.

**Table S4.** Target materials that are not thermodynamic stable on the convex hull.

Target	Energy above hull (meV/atom)	Decomposition products	Target phase fraction	
			From predicted precursors	From traditional precursors
$\text{LiZnBO}_3$	8	$1/3 \text{ ZnO} + 2/3 \text{ LiBO}_2$	0.52	0.15
$\text{LiNbWO}_6$	10	$\text{LiNb}_3\text{O}_8 + \text{Li}_2\text{WO}_4 + \text{WO}_3$	0.17	0.05
$\text{KTiNbO}_5$	1	$\text{K}_4\text{Nb}_6\text{O}_{17} + \text{K}_2\text{Ti}_6\text{O}_{13}$	0.18	0.27
$\text{Li}_3\text{Y}_2(\text{BO}_3)_3$	39	$19/34 \text{ Li}_6\text{Y}(\text{BO}_3)_3 + 15/34 \text{ YBO}_3$	0.17	0.12

### SI3.3. Comparison of energy contribution between $T\Delta S$ and $\Delta H$

In this section, we compared the magnitude of the entropy contribution,  $T\Delta S$ , to the overall  $\Delta G$  of a reaction. We used experimental thermochemical data queried through Materials Project API in the ‘Experimental Data’ field. This experimental thermochemical data originated from NIST JANAF<sup>1</sup>, Materials Thermochemistry<sup>2</sup>, and the CODATA Key Values for Thermodynamics<sup>3</sup>. We collected entropy ( $S$ ) and formation enthalpy ( $H_f$ ) data at 298K for all convex hull stable binary and ternary oxides among 49 common metal elements. Then, using the selected binary metal oxides as precursors, we generated all possible pairwise combination reactions for the formation of the selected ternary oxides, resulting in exactly 100 reactions total. The energy contributions of  $T\Delta S$ ,  $\Delta H_f$ , reaction formation energy  $\Delta G$ , are plotted in **Figure S16a**, **S16b**, and **S16c**, respectively. The ratio of the magnitude of the entropy contribution to total reaction energy magnitude ( $|T\Delta S / \Delta G|$ ) was also calculated for each individual reaction, shown in **Figure S16d**. Full oxide reactions are presented in **Table S5**.

Altogether, **Figure S16** indicates that for the majority of reactions, the energy contribution of entropy at 1000K is considerably smaller in magnitude than the total reaction energy. By choosing a characteristic synthesis temperature of 1000K, the distribution peak of  $|T\Delta S|$  term is  $\sim 15$  meV/atom, while that of  $\Delta H$  term is  $-185$  meV/atom. Specifically, 60% of reactions have  $|T\Delta S / \Delta G|$  values less than 0.1. Among the remaining 40% of reactions where  $|T\Delta S / \Delta G|$  values are greater than or equal to 0.1, approximately half have a relatively low reaction formation energy  $\Delta G$  ( $\sim 100$  meV/atom). Therefore, in the context of oxide synthesis reactions, entropic contributions are usually negligible due to the dominant contribution of the enthalpy  $\Delta H$  to the free energy  $\Delta G$ .

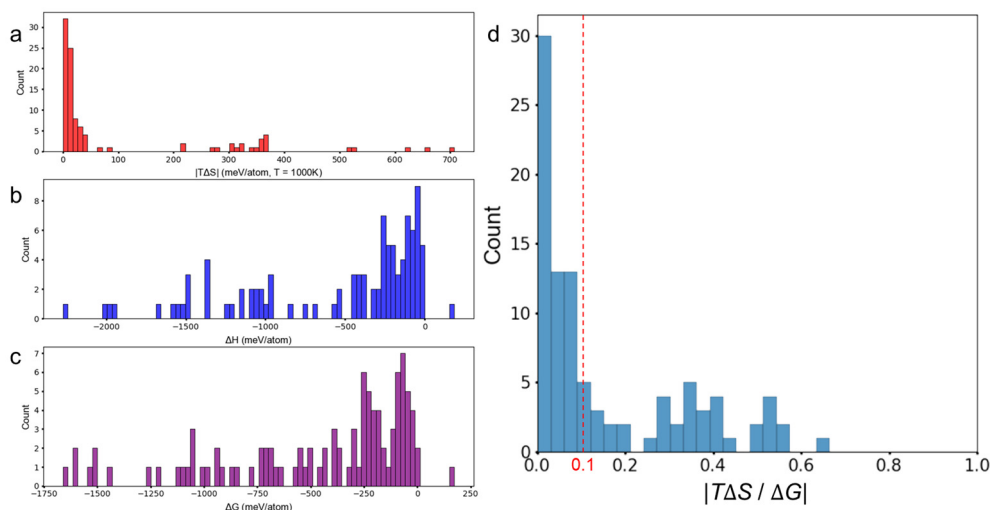


**Figure S16.** Histograms of **a.**  $|T\Delta S|$ , **b.**  $\Delta H$ , **c.**  $\Delta G$ , **d.**  $|T\Delta S/\Delta G|$  of 100 reactions which uses binary metal oxides as reactants to synthesize ternary metal oxides in Materials Projects database. The entropy and enthalpy data we use is experimental data in room temperature (298K). The synthesis temperature  $T$  we choose is 1000K.

<sup>1</sup> Chase, Malcolm W., and National Information Standards Organization (US). NIST-JANAF thermochemical tables. Vol. 9. Washington, DC: American Chemical Society, 1998.

<sup>2</sup> Kubaschewski, Oswald, Charles B. Alcock, and P. J. Spencer. "Materials thermochemistry. revised." Pergamon Press Ltd, Headington Hill Hall, Oxford OX 3 0 BW, UK, 1993. 363 (1993).

<sup>3</sup> Cox, J. D., Wagman, D. D., and Medvedev, V. A., CODATA Key Values for Thermodynamics, Hemisphere Publishing Corp., New York, 1989.

**Table S5.** Thermodynamic data table of 100 reactions which uses binary metal oxides as precursors to synthesize ternary metal oxides.

	Reactions	$\Delta S$ (meV/atom/K)	$T\Delta S$ (meV/atom, $T = 1000K$ )	$\Delta H$ (meV/atom)	$\Delta G$ (meV/atom)	$ T\Delta S/\Delta G $
1	$0.5 K_2O + 0.5 Fe_2O_3 \rightarrow KFeO_2$	-0.00729	-7.29	-1668	-1661	0.00439
2	$SrO + WO_3 \rightarrow SrWO_4$	-0.66	-660	-2271	-1610	0.41
3	$SrO_2 + MoO_2 \rightarrow SrMoO_4$	0.0405	40.5	-1567	-1607	0.0252
4	$Na_2O_2 + MoO_2 \rightarrow Na_2MoO_4$	0.0269	26.9	-1499	-1526	0.0176
5	$BaO_2 + MoO_2 \rightarrow BaMoO_4$	0.0127	12.7	-1509	-1521	0.00834
6	$2 SrO + SiO_2 \rightarrow Sr_2SiO_4$	-0.523	-523	-2024	-1501	0.349
7	$2 SrO + TiO_2 \rightarrow Sr_2TiO_4$	-0.519	-519	-1953	-1434	0.362
8	$NiO + WO_3 \rightarrow NiWO_4$	-0.707	-707	-1978	-1271	0.556
9	$MnO_2 + MoO_2 \rightarrow MnMoO_4$	0.0629	62.9	-1144	-1207	0.0522
10	$SrO + TiO_2 \rightarrow SrTiO_3$	-0.355	-355	-1483	-1128	0.315
11	$SrO + SiO_2 \rightarrow SrSiO_3$	-0.367	-367	-1475	-1107	0.332
12	$K_2O + WO_3 \rightarrow K_2WO_4$	-0.303	-303	-1370	-1067	0.284
13	$2 Na_2O + 3 TiO \rightarrow Na_2Ti_3O_7$	-0.0881	-88.1	-1150	-1062	0.0829
14	$SrO + MoO_3 \rightarrow SrMoO_4$	-0.309	-309	-1365	-1056	0.292
15	$SrO_2 + TiO \rightarrow SrTiO_3$	0.0305	30.5	-1025	-1055	0.0289
16	$SrO + ZrO_2 \rightarrow SrZrO_3$	-0.356	-356	-1353	-997.7	0.356
17	$SrO + HfO_2 \rightarrow SrHfO_3$	-0.366	-366	-1352	-986.9	0.37
18	$BaO_2 + TiO \rightarrow BaTiO_3$	-0.0412	-41.2	-975.3	-934.1	0.0441
19	$PbO + WO_3 \rightarrow PbWO_4$	-0.619	-619	-1552	-933.1	0.663
20	$Na_2O + WO_3 \rightarrow Na_2WO_4$	-0.321	-321	-1230	-908.4	0.354
21	$CaO + WO_3 \rightarrow CaWO_4$	-0.342	-342	-1202	-860.3	0.397
22	$Li_2O_2 + TiO \rightarrow Li_2TiO_3$	0.00117	1.17	-853.8	-855	0.00137
23	$Cs_2O + MoO_3 \rightarrow Cs_2MoO_4$	-0.218	-218	-1003	-784.3	0.278
24	$Li_2O + WO_3 \rightarrow Li_2WO_4$	-0.312	-312	-1054	-741.5	0.421
25	$MnO + WO_3 \rightarrow MnWO_4$	-0.355	-355	-1084	-729.7	0.486
26	$MgO + WO_3 \rightarrow MgWO_4$	-0.366	-366	-1076	-709.5	0.516
27	$0.5 Li_2O_2 + NbO_2 \rightarrow LiNbO_3$	0.00555	5.55	-700.4	-705.9	0.00787
28	$CoO + WO_3 \rightarrow CoWO_4$	-0.367	-367	-1056	-688.8	0.533
29	$SrO + Al_2O_3 \rightarrow SrAl_2O_4$	-0.279	-279	-961.7	-682.8	0.408
30	$ZnO + WO_3 \rightarrow ZnWO_4$	-0.346	-346	-1014	-668.9	0.517
31	$Cs_2O + SiO_2 \rightarrow Cs_2SiO_3$	-0.321	-321	-963	-642.3	0.499
32	$K_2O + SiO_2 \rightarrow K_2SiO_3$	0.015	15	-549.8	-564.8	0.0265
33	$1.5 Na_2O + 0.5 V_2O_5 \rightarrow Na_3VO_4$	-0.017	-17	-568.9	-551.9	0.0309
34	$3 CaO + WO_3 \rightarrow Ca_3WO_6$	-0.213	-213	-761.3	-548.1	0.389
35	$Na_2O + MoO_3 \rightarrow Na_2MoO_4$	-0.0148	-14.8	-549.3	-534.5	0.0277
36	$0.5 Na_2O + 0.5 Al_2O_3 \rightarrow NaAlO_2$	0.271	271	-237.4	-508.5	0.533
37	$0.5 Na_2O_2 + VO_2 \rightarrow NaVO_3$	0.04	40	-458.3	-498.3	0.0803
38	$Na_2O_2 + Ti_3O_5 \rightarrow Na_2Ti_3O_7$	0.00839	8.39	-439.9	-448.3	0.0187
39	$0.5 Na_2O + 0.5 V_2O_5 \rightarrow NaVO_3$	0.00569	5.69	-430	-435.6	0.0131

40	$\text{Na}_2\text{O} + 2 \text{MoO}_3 \rightarrow \text{Na}_2\text{Mo}_2\text{O}_7$	0.00323	3.23	-426.3	-429.6	0.00752
41	$\text{K}_2\text{O} + 2 \text{SiO}_2 \rightarrow \text{K}_2\text{Si}_2\text{O}_5$	0.0112	11.2	-378.6	-389.9	0.0288
42	$2 \text{BaO} + \text{SiO}_2 \rightarrow \text{Ba}_2\text{SiO}_4$	-0.0144	-14.4	-396.3	-382	0.0376
43	$\text{BaO} + \text{MoO}_3 \rightarrow \text{BaMoO}_4$	-0.00506	-5.06	-385.1	-380	0.0133
44	$2 \text{Na}_2\text{O} + \text{SiO}_2 \rightarrow \text{Na}_4\text{SiO}_4$	-0.0355	-35.5	-410.9	-375.4	0.0945
45	$\text{Na}_2\text{O} + \text{SiO}_2 \rightarrow \text{Na}_2\text{SiO}_3$	-0.0366	-36.6	-408.9	-372.3	0.0984
46	$\text{BaO} + \text{SiO}_2 \rightarrow \text{BaSiO}_3$	-0.0225	-22.5	-334.8	-312.4	0.072
47	$\text{BaO} + \text{TiO}_2 \rightarrow \text{BaTiO}_3$	-0.0291	-29.1	-327.8	-298.7	0.0975
48	$\text{CaO} + \text{MoO}_3 \rightarrow \text{CaMoO}_4$	0.0114	11.4	-286.2	-297.6	0.0385
49	$2 \text{BaO} + \text{TiO}_2 \rightarrow \text{Ba}_2\text{TiO}_4$	0.00385	3.85	-289.8	-293.6	0.0131
50	$3 \text{CaO} + \text{V}_2\text{O}_5 \rightarrow \text{Ca}_3\text{V}_2\text{O}_8$	0.0238	23.8	-256.8	-280.6	0.0847
51	$\text{BaO}_2 + 2 \text{VO}_2 \rightarrow \text{BaV}_2\text{O}_6$	0.00737	7.37	-253.4	-260.7	0.0283
52	$2 \text{CaO} + \text{V}_2\text{O}_5 \rightarrow \text{Ca}_2\text{V}_2\text{O}_7$	0.0128	12.8	-247.2	-260	0.0493
53	$\text{Na}_2\text{O} + 2 \text{SiO}_2 \rightarrow \text{Na}_2\text{Si}_2\text{O}_5$	-0.0161	-16.1	-275.1	-259	0.0623
54	$\text{BaO} + \text{ZrO}_2 \rightarrow \text{BaZrO}_3$	0.00466	4.66	-248.8	-253.5	0.0184
55	$0.5 \text{Na}_2\text{O} + 0.5 \text{Cr}_2\text{O}_3 \rightarrow \text{NaCrO}_2$	-0.0128	-12.8	-259.4	-246.6	0.0518
56	$\text{Li}_2\text{O} + \text{SiO}_2 \rightarrow \text{Li}_2\text{SiO}_3$	-0.00233	-2.33	-244.3	-241.9	0.00963
57	$\text{BaO} + \text{HfO}_2 \rightarrow \text{BaHfO}_3$	-0.021	-21	-257.5	-236.5	0.0889
58	$0.5 \text{Li}_2\text{O} + 0.5 \text{Nb}_2\text{O}_5 \rightarrow \text{LiNbO}_3$	-0.00451	-4.51	-240.5	-236	0.0191
59	$\text{Li}_2\text{O} + \text{TiO}_2 \rightarrow \text{Li}_2\text{TiO}_3$	0.00699	6.99	-223.9	-230.9	0.0303
60	$2 \text{CaO} + \text{SiO}_2 \rightarrow \text{Ca}_2\text{SiO}_4$	0.0116	11.6	-208.9	-220.4	0.0525
61	$\text{K}_2\text{O} + 4 \text{SiO}_2 \rightarrow \text{K}_2\text{Si}_4\text{O}_9$	-0.00133	-1.33	-220.6	-219.3	0.00608
62	$\text{BaO} + \text{V}_2\text{O}_5 \rightarrow \text{BaV}_2\text{O}_6$	-0.0102	-10.2	-211.5	-201.3	0.0506
63	$\text{Na}_2\text{O} + 3 \text{TiO}_2 \rightarrow \text{Na}_2\text{Ti}_3\text{O}_7$	-0.0064	-6.4	-207	-200.6	0.0319
64	$0.5 \text{Li}_2\text{O} + 0.5 \text{Ta}_2\text{O}_5 \rightarrow \text{LiTaO}_3$	-0.00098	-0.984	-200.2	-199.2	0.00494
65	$0.5 \text{Na}_2\text{O} + 0.5 \text{Fe}_2\text{O}_3 \rightarrow \text{NaFeO}_2$	-0.00312	-3.12	-198.3	-195.2	0.016
66	$\text{CaO} + \text{SiO}_2 \rightarrow \text{CaSiO}_3$	0.012	12	-175.3	-187.4	0.0643
67	$\text{CaO} + \text{TiO}_2 \rightarrow \text{CaTiO}_3$	0.0116	11.6	-174.3	-185.9	0.0625
68	$0.5 \text{Li}_2\text{O} + 0.5 \text{Fe}_2\text{O}_3 \rightarrow \text{LiFeO}_2$	0.0328	32.8	-147.3	-180.2	0.182
69	$\text{CaO} + \text{V}_2\text{O}_5 \rightarrow \text{CaV}_2\text{O}_6$	0.012	12	-165.2	-177.2	0.0676
70	$\text{CaO} + \text{GeO}_2 \rightarrow \text{CaGeO}_3$	0.0197	19.7	-145.5	-165.2	0.119
71	$\text{BaO} + \text{Al}_2\text{O}_3 \rightarrow \text{BaAl}_2\text{O}_4$	0.0136	13.6	-148.6	-162.2	0.084
72	$0.5 \text{Li}_2\text{O} + 0.5 \text{Al}_2\text{O}_3 \rightarrow \text{LiAlO}_2$	0.00196	1.96	-133.3	-135.3	0.0145
73	$\text{MgO} + \text{MoO}_3 \rightarrow \text{MgMoO}_4$	0.0245	24.5	-93.22	-117.7	0.208
74	$\text{Li}_2\text{O} + \text{ZrO}_2 \rightarrow \text{Li}_2\text{ZrO}_3$	0.00578	5.78	-108.4	-114.2	0.0507
75	$\text{MnO} + \text{MoO}_3 \rightarrow \text{MnMoO}_4$	-0.00273	-2.73	-106.2	-103.5	0.0264
76	$\text{CaO} + \text{Cr}_2\text{O}_3 \rightarrow \text{CaCr}_2\text{O}_4$	0.00941	9.41	-88.67	-98.08	0.096
77	$\text{Li}_2\text{O} + \text{HfO}_2 \rightarrow \text{Li}_2\text{HfO}_3$	-0.00181	-1.81	-99.75	-97.94	0.0185
78	$0.5 \text{La}_2\text{O}_3 + 0.5 \text{Al}_2\text{O}_3 \rightarrow \text{LaAlO}_3$	-0.0246	-24.6	-121.4	-96.82	0.254
79	$2 \text{MgO} + \text{SiO}_2 \rightarrow \text{Mg}_2\text{SiO}_4$	-0.00281	-2.81	-97.86	-95.05	0.0296
80	$2 \text{MgO} + \text{V}_2\text{O}_5 \rightarrow \text{Mg}_2\text{V}_2\text{O}_7$	0.0149	14.9	-77.25	-92.13	0.162
81	$\text{ZnO} + \text{Cr}_2\text{O}_3 \rightarrow \text{ZnCr}_2\text{O}_4$	-0.0118	-11.8	-93.09	-81.33	0.145

82	$2 \text{ MnO} + \text{ SiO}_2 \rightarrow \text{ Mn}_2\text{SiO}_4$	0.000296	0.296	-78.14	-78.44	0.00377
83	$\text{ CaO} + \text{ ZrO}_2 \rightarrow \text{ CaZrO}_3$	0.0106	10.6	-63.42	-74.01	0.143
84	$\text{ MgO} + \text{ GeO}_2 \rightarrow \text{ MgGeO}_3$	0.00816	8.16	-56.07	-64.23	0.127
85	$\text{ MgO} + \text{ V}_2\text{O}_5 \rightarrow \text{ MgV}_2\text{O}_6$	0.00386	3.86	-56.82	-60.68	0.0636
86	$\text{ CaO} + \text{ HfO}_2 \rightarrow \text{ CaHfO}_3$	0.00334	3.34	-56.59	-59.92	0.0557
87	$\text{ MgO} + \text{ Cr}_2\text{O}_3 \rightarrow \text{ MgCr}_2\text{O}_4$	-0.00237	-2.37	-61.95	-59.58	0.0397
88	$\text{ MgO} + \text{ TiO}_2 \rightarrow \text{ MgTiO}_3$	-0.00445	-4.45	-62.08	-57.62	0.0773
89	$2 \text{ ZnO} + \text{ SiO}_2 \rightarrow \text{ Zn}_2\text{SiO}_4$	0.00118	1.18	-50.02	-51.21	0.0231
90	$2 \text{ MgO} + \text{ TiO}_2 \rightarrow \text{ Mg}_2\text{TiO}_4$	0.017	17	-30.37	-47.39	0.359
91	$\text{ CdO} + \text{ SiO}_2 \rightarrow \text{ CdSiO}_3$	-0.00145	-1.45	-46.93	-45.48	0.0319
92	$\text{ MgO} + \text{ Al}_2\text{O}_3 \rightarrow \text{ MgAl}_2\text{O}_4$	-0.00798	-7.98	-53.22	-45.24	0.176
93	$2 \text{ CoO} + \text{ SiO}_2 \rightarrow \text{ Co}_2\text{SiO}_4$	0.0141	14.1	-22.08	-36.14	0.389
94	$\text{ ZrO}_2 + \text{ SiO}_2 \rightarrow \text{ ZrSiO}_4$	-0.0161	-16.1	-44.2	-28.14	0.571
95	$\text{ MnO} + \text{ Al}_2\text{O}_3 \rightarrow \text{ MnAl}_2\text{O}_4$	-0.0344	-34.4	-58.9	-24.51	1.4
96	$2 \text{ BeO} + \text{ SiO}_2 \rightarrow \text{ Be}_2\text{SiO}_4$	-0.00968	-9.68	-31.08	-21.4	0.452
97	$\text{ CaO} + 2 \text{ Al}_2\text{O}_3 \rightarrow \text{ CaAl}_4\text{O}_7$	0.00443	4.43	-10.89	-15.32	0.289
98	$\text{ BeO} + \text{ Al}_2\text{O}_3 \rightarrow \text{ BeAl}_2\text{O}_4$	-0.0218	-21.8	-25.38	-3.611	6.03
99	$\text{ Al}_2\text{O}_3 + \text{ SiO}_2 \rightarrow \text{ Al}_2\text{SiO}_5$	-0.0188	-18.8	-7.123	11.71	1.61
100	$\text{ MgO} + 2 \text{ TiO}_2 \rightarrow \text{ MgTi}_2\text{O}_5$	0.0116	11.6	183.9	172.4	0.0672

To explicitly illustrate that the temperature-dependent reaction free energies are negligible, **Figure S17** shows the candidate pairwise reaction *free-energies* for  $\text{LiZnPO}_4$ ,  $\text{BaLiBO}_3$ , and  $\text{SrLiBO}_3$  as a function of temperature.  $\text{BaLiBO}_3$  and  $\text{LiZnPO}_4$  are the systems from Figures 1 and 2 of the manuscript. These free-energy calculations were conducted utilizing the *GibbsStructureComputedEntry* module within the *Pymatgen* package, where Bartel *et al.* [Manuscript Reference 45] developed a physical descriptor to predict temperature-dependent Gibbs free energy using the SISSO (Sure Independence Screening and Sparsifying Operator) machine-learning approach. This module takes both materials structure and temperature as input parameters, and calculates the temperature-dependence of the free energy.

**Figure S17** shows that as the temperature elevates from 0 to 1000K, the free energy of these solid-state reactions deviate from the reaction enthalpy by less than 10%. The magnitude of the  $T\Delta S$  contribution is much smaller than the difference in reaction enthalpies between the different precursors. Our result here reinforces the dominance of the enthalpy contribution in overall reaction energy, and supports the validity of our assumption in not accounting for the temperature-dependent free-energy in this study.

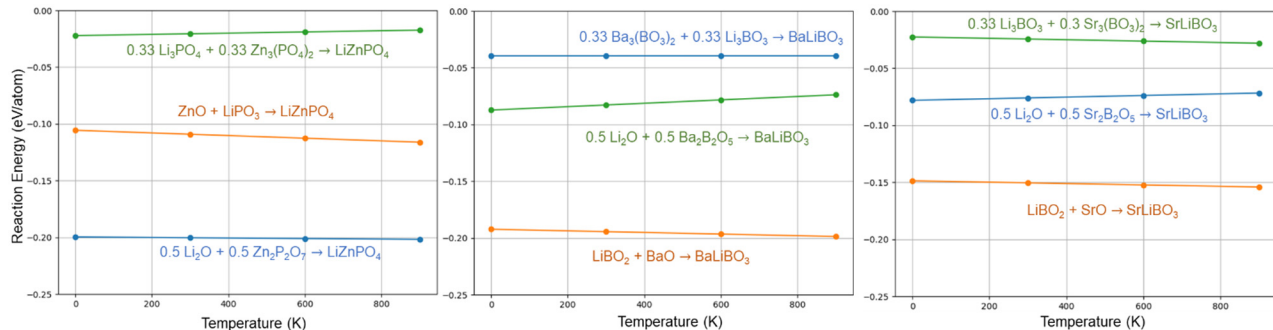


**Figure S17.** The relationship between reaction energy and temperature for three distinct pairwise reactions of  $\text{LiZnPO}_4$  system.

We note that this assumption is relevant in because we have specifically chosen reactions in this study where the reactants and products are solids. When volatile gases are involved in a solid-state reaction, the temperature dependence of the reaction is largely dominated by whether the reactant or product side has more moles of gas, which contribute an entropy of approximately  $\Delta S = 1 \text{ eV/atom/1000K}$ . (Note that by this normalization, 1 molecule of  $\text{O}_2$  gas contributes 2 eV/atom at 1000K).

### SI3.4. Failed synthesis: Summary/discussion

For a number of compounds, neither set of precursors produced an XRD signal matching the target crystal structure, and as such these synthesis attempts are classified as failures based on the XRD quantification method used in this study.

While it is often not possible to determine the exact reason for an unsuccessful synthesis, there are several common factors that can result in failed synthesis even for a thermodynamically stable target:

#### 1) **Insufficient synthesis temperature**

- If the calcination temperature is insufficient, some of the precursors may not fully decompose and react, and as a result does not form a uniform product.
- Likely applies to  $\text{KTiNbO}_5$  and  $\text{Li}_3\text{Y}_2(\text{BO}_3)_2$  in the present study.

#### 2) **Evaporation of precursors**

- Some precursors have significant vapor pressure and are prone to being lost to evaporation during calcination, resulting in deficiency of the affected components.
- Well known to occur with Li, P, B precursors.
- The great majority of studies on Li-oxide synthesis for example add excess Li precursor, most often 10%, to hedge against evaporation. We did not do this here, since it was difficult to apply this uniformly over such a broad chemical space, including Na- and K- based compounds.
- It is hard to determine *a priori* which samples evaporation could apply to here – usually this will affect purity more than overall success/failure, but it can be very impactful in cases where (a) formation of the target phase requires high temperature and/or longer times, or (b) there is a small composition window for the target phase.

#### 3) **Excessive oxidation during synthesis**

- For all ASTRAL synthesis experiments presented in this study, calcination was performed in ambient air, and as such each element will attain the most energetically favorable oxidation state based on reaction with oxygen gas at high temperature.
- For materials containing transition metals, this can result in incorrect oxidation states during synthesis, preventing formation of the target phase.
- Likely applies to  $\text{Li}_3\text{V}_2(\text{PO}_4)_3$  – in the literature report, a reducing atmosphere ( $\text{Ar} + \text{H}_2$ ) is used for the final synthesis reaction. Also, V has many available oxidation states (+2, +3, +4, +5), and for the target material we need  $\text{V}^{3+}$ , so it is reasonable to suspect that  $\text{V}^{5+}$  formation could be the cause of the failure.

#### 4) **Amorphous synthesis products**

- ASTRAL classifies synthesis outcomes based on powder XRD, and so any amorphous phases present are not detected or used for quantification. This can result in an apparently failed synthesis, even in cases where the sample has formed a homogeneous mixture of the correct composition.
- For such glass forming compositions, successful crystallization requires controlled cooling, typically with a period of annealing at an appropriate temperature to nucleate and grow crystals.
- Likely applies to  $\text{KLi}(\text{PO}_3)_2$  and  $\text{NaSiBO}_4$  in the present study, as each (1) contains a high proportion of glass-forming elements, (2) each formed fully fused samples with a glassy appearance, and (3) despite adequate yield of reaction product, almost no crystalline peaks were observed on XRD.

### SI3.5. Reaction compound convex hull, XRD, phase purity of 35 target systems

#### LiZnPO<sub>4</sub>

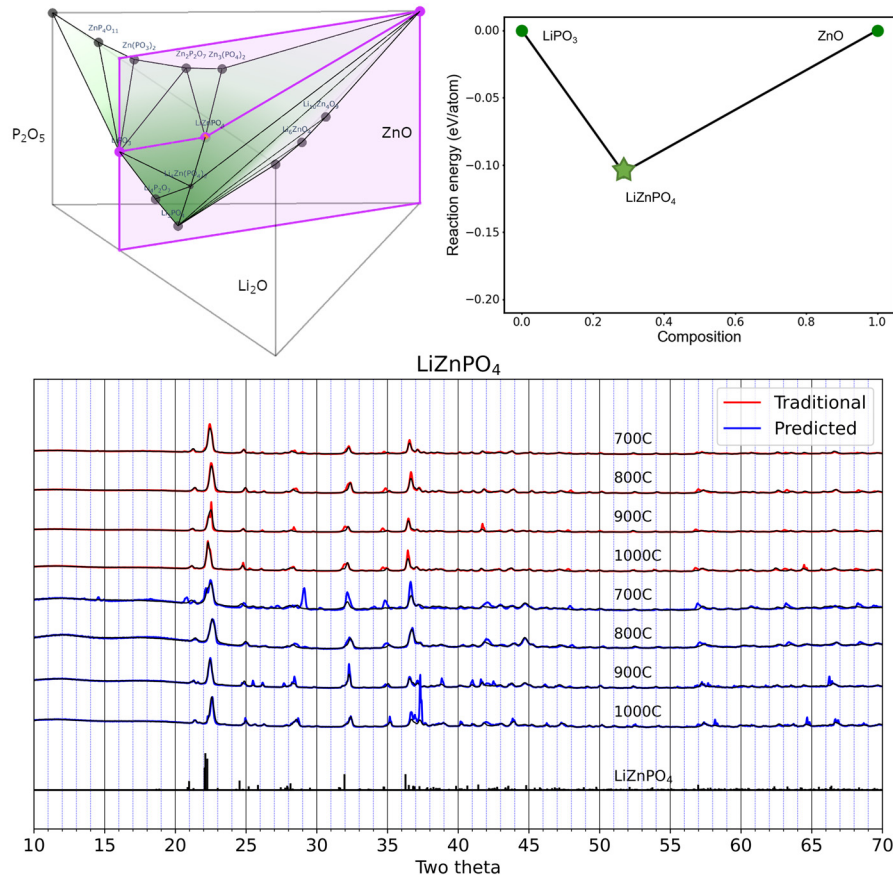


Table 1. Temperature, XRD intensities, and phase fraction of traditional and predicted reactions.

Compound	Precursor type	Precursors	Temp (°C)	Target intensity (e6)	Residual intensity (e6)	Target phase fraction
LiZnPO <sub>4</sub>	Traditional	Li <sub>2</sub> CO <sub>3</sub> , NH <sub>4</sub> H <sub>2</sub> PO <sub>4</sub> , ZnO	700	3.78	1.35	0.74
			800	5.01	1.62	0.76
			900	3.53	1.70	0.67
			1000	3.40	1.18	0.74
	Predicted	LiPO <sub>3</sub> , ZnO	700	1.83	1.34	0.58
			800	1.54	0.65	0.70
			900	2.12	0.99	0.68
			1000	2.54	1.26	0.67

Table 2. Candidate pairwise reactions evaluated using our precursor selection principles

Pairwise	Deepest	Reaction energy	Competing Phases	Inverse hull energy	Reaction	Best
Y	Y	-0.106	0	-0.106	ZnO + LiPO <sub>3</sub> → LiZnPO <sub>4</sub>	Y
Y	N	-0.2	4	-0.04	0.5 Li <sub>2</sub> O + 0.5 Zn <sub>2</sub> P <sub>2</sub> O <sub>7</sub> → LiZnPO <sub>4</sub>	N
Y	Y	-0.035	1	-0.022	0.3333 Li <sub>3</sub> PO <sub>4</sub> + 0.3333 Zn <sub>3</sub> (PO <sub>4</sub> ) <sub>2</sub> → LiZnPO <sub>4</sub>	N
Y	Y	-0.022	0	-0.022	0.25 Li <sub>4</sub> Zn(PO <sub>4</sub> ) <sub>2</sub> + 0.25 Zn <sub>3</sub> (PO <sub>4</sub> ) <sub>2</sub> → LiZnPO <sub>4</sub>	N

# LiMnPO<sub>4</sub>

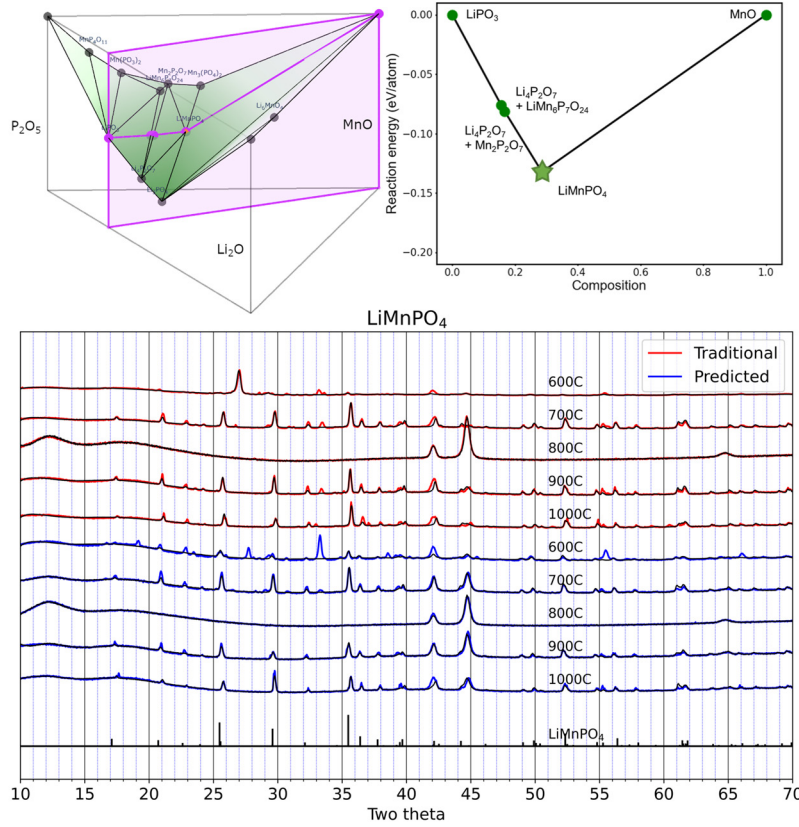


Table 1. Temperature, XRD intensities, and phase fraction of traditional and predicted reactions.

Compound	Precursor type	Precursors	Temp (°C)	Target intensity (e6)	Residual intensity (e6)	Target phase fraction
LiMnPO <sub>4</sub>	Traditional	Li <sub>2</sub> CO <sub>3</sub> , MnO, NH <sub>4</sub> H <sub>2</sub> PO <sub>4</sub>	600	0.28	0.78	0.26
			700	1.00	0.59	0.63
			800	0.00	0.29	0.01
			900	0.60	0.47	0.56
			1000	0.51	0.46	0.52
	Predicted	MnO, LiPO <sub>3</sub>	600	0.32	0.90	0.27
			700	0.66	0.46	0.59
			800	0.00	0.26	0.02
			900	0.42	0.36	0.54
			1000	0.40	0.38	0.51

Table 2. Candidate pairwise reactions evaluated using our precursor selection principles

Pairwise	Deepest	Reaction energy	Competing Phases	Inverse hull energy	Reaction	Best
Y	N	-0.54	5	-0.163	MnPO <sub>4</sub> + Li → LiMnPO <sub>4</sub>	N
Y	Y	-0.132	2	-0.063	MnO + LiPO <sub>3</sub> → LiMnPO <sub>4</sub>	Y
Y	N	-0.158	2	-0.047	0.14 Li <sub>6</sub> MnO <sub>4</sub> + 0.14 LiMn <sub>6</sub> P <sub>7</sub> O <sub>24</sub> → LiMnPO <sub>4</sub>	N
Y	N	-0.163	2	-0.044	0.5 Li <sub>2</sub> O + 0.5 Mn <sub>2</sub> P <sub>2</sub> O <sub>7</sub> → LiMnPO <sub>4</sub>	N
Y	Y	-0.008	0	-0.008	0.33 Mn <sub>3</sub> (PO <sub>4</sub> ) <sub>2</sub> + 0.33 Li <sub>3</sub> PO <sub>4</sub> → LiMnPO <sub>4</sub>	N

# Li<sub>2</sub>CuP<sub>2</sub>O<sub>7</sub>

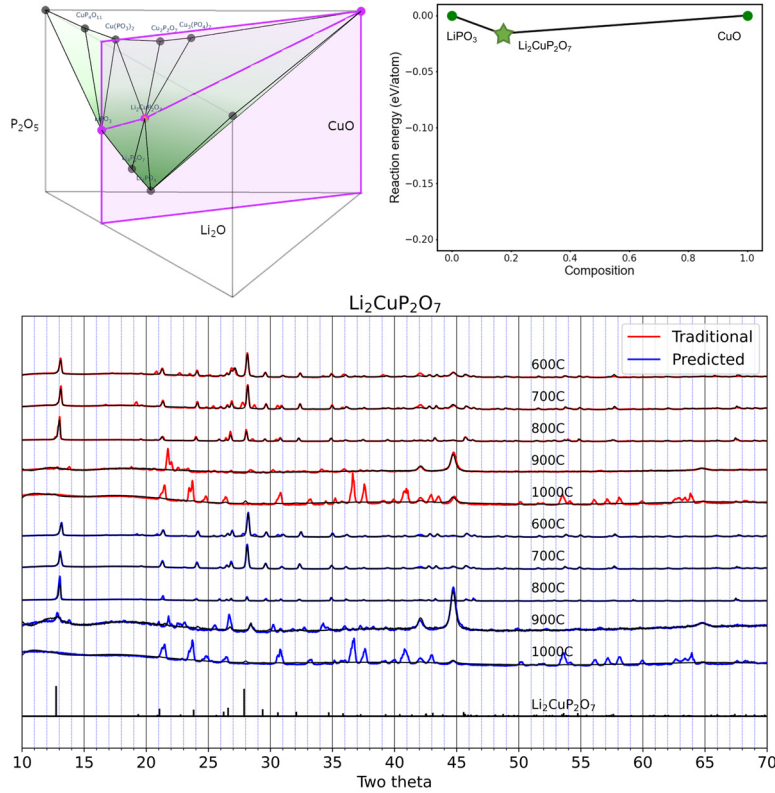


Table 1. Temperature, XRD intensities, and phase fraction of traditional and predicted reactions.

Compound	Precursor type	Precursors	Temp (°C)	Target intensity (e6)	Residual intensity (e6)	Target phase fraction
Li <sub>2</sub> CuP <sub>2</sub> O <sub>7</sub>	Traditional	CuO, Li <sub>2</sub> CO <sub>3</sub> , NH <sub>4</sub> H <sub>2</sub> PO <sub>4</sub>	600	1.90	1.10	0.63
			700	1.93	1.09	0.64
			800	3.15	1.22	0.72
			900	0.00	0.84	0.00
	Predicted	CuO, LiPO <sub>3</sub>	1000	0.10	1.59	0.06
			600	3.37	1.11	0.75
			700	3.00	0.83	0.78
			800	2.83	2.04	0.58
			900	0.20	0.70	0.22
			1000	0.05	1.46	0.03

Table 2. Candidate pairwise reactions evaluated using our precursor selection principles

Pairwise	Deepest	Reaction energy	Competing Phases	Inverse hull energy	Reaction	Best
Y	N	-0.261	2	-0.059	Li <sub>2</sub> O + Cu(PO <sub>3</sub> ) <sub>2</sub> → Li <sub>2</sub> CuP <sub>2</sub> O <sub>7</sub>	N
Y	Y	-0.036	0	-0.036	CuO + 2 LiPO <sub>3</sub> → Li <sub>2</sub> CuP <sub>2</sub> O <sub>7</sub>	Y
Y	Y	-0.035	0	-0.035	0.5 Li <sub>4</sub> P <sub>2</sub> O <sub>7</sub> + 0.5 Cu <sub>2</sub> P <sub>2</sub> O <sub>7</sub> → Li <sub>2</sub> CuP <sub>2</sub> O <sub>7</sub>	N

# LiMgPO<sub>4</sub>

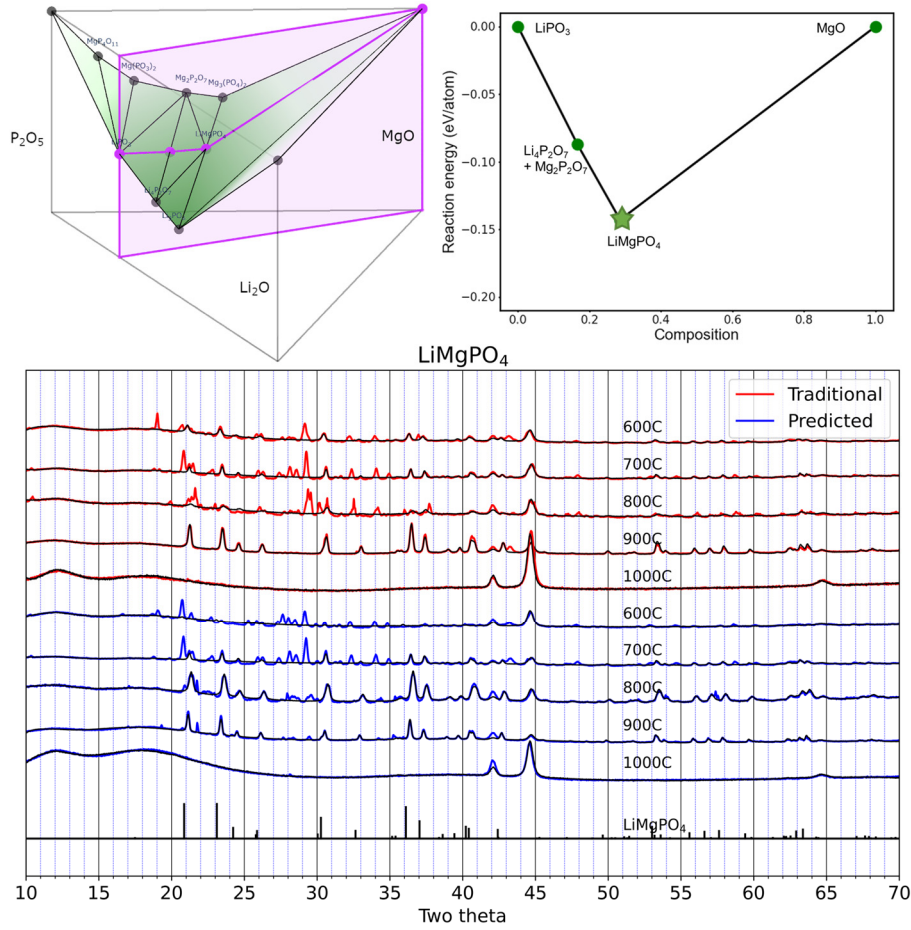


Table 1. Temperature, XRD intensities, and phase fraction of traditional and predicted reactions.

Compound	Precursor type	Precursors	Temp (°C)	Target intensity (e6)	Residual intensity (e6)	Target phase fraction
LiMgPO <sub>4</sub>	Traditional	Li <sub>2</sub> CO <sub>3</sub> , MgO, NH <sub>4</sub> H <sub>2</sub> PO <sub>4</sub>	600	0.65	1.04	0.39
			700	0.13	0.95	0.12
			800	0.32	0.81	0.29
			900	1.61	0.53	0.75
			1000	0.03	0.38	0.07
	Predicted	MgO, LiPO <sub>3</sub>	600	0.06	1.13	0.05
			700	0.14	0.77	0.15
			800	1.33	0.56	0.70
			900	1.37	0.92	0.60
			1000	0.11	0.52	0.17

Table 2. Candidate pairwise reactions evaluated using our precursor selection principles

Pairwise	Deepest	Reaction energy	Competing Phases	Inverse hull energy	Reaction	Best
Y	Y	-0.143	1	-0.068	MgO + LiPO <sub>3</sub> → LiMgPO <sub>4</sub>	Y
Y	N	-0.163	1	-0.048	0.5 Li <sub>2</sub> O + 0.5 Mg <sub>2</sub> P <sub>2</sub> O <sub>7</sub> → LiMgPO <sub>4</sub>	N
Y	Y	-0.005	0	-0.005	0.33 Mg <sub>3</sub> (PO <sub>4</sub> ) <sub>2</sub> + 0.33 Li <sub>3</sub> PO <sub>4</sub> → LiMgPO <sub>4</sub>	N

## BaLiBO<sub>3</sub>

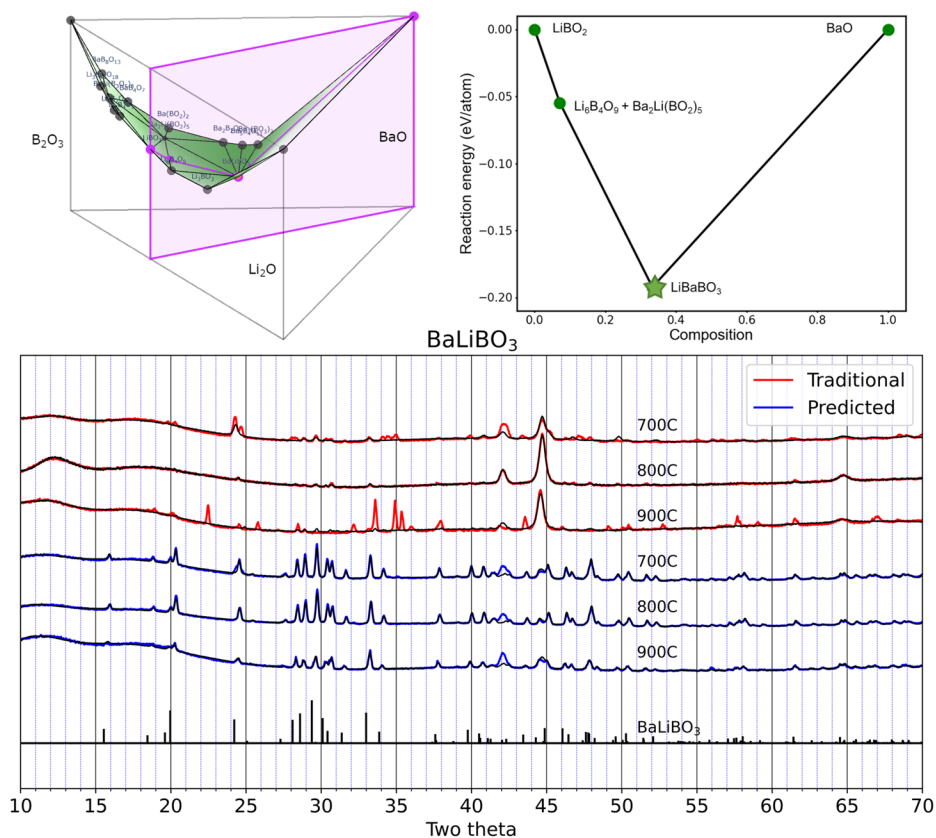


Table 1. Temperature, XRD intensities, and phase fraction of traditional and predicted reactions.

Compound	Precursor type	Precursors	Temp (°C)	Target intensity (e6)	Residual intensity (e6)	Target phase fraction
BaLiBO <sub>3</sub>	Traditional	Li <sub>2</sub> CO <sub>3</sub> ,	700	0.23	0.49	0.32
		BaO,	800	0.11	0.25	0.30
		B <sub>2</sub> O <sub>3</sub>	900	0.08	0.69	0.10
	Predicted	BaO,	700	0.98	0.35	0.74
		LiBO <sub>2</sub>	800	1.14	0.34	0.77
			900	0.54	0.36	0.60

Table 2. Candidate pairwise reactions evaluated using our precursor selection principles

Pairwise	Deepest	Reaction energy	Competing Phases	Inverse hull energy	Reaction	Best
Y	Y	-0.192	1	-0.153	LiBO <sub>2</sub> + BaO → BaLiBO <sub>3</sub>	Y
Y	Y	-0.04	0	-0.04	0.33 Li <sub>3</sub> BO <sub>3</sub> + 0.33 Ba <sub>3</sub> (BO <sub>3</sub> ) <sub>2</sub> → BaLiBO <sub>3</sub>	N
Y	Y	-0.087	0	-0.087	0.5 Li <sub>2</sub> O + 0.5 Ba <sub>2</sub> B <sub>2</sub> O <sub>5</sub> → BaLiBO <sub>3</sub>	N

## SrLiBO<sub>3</sub>

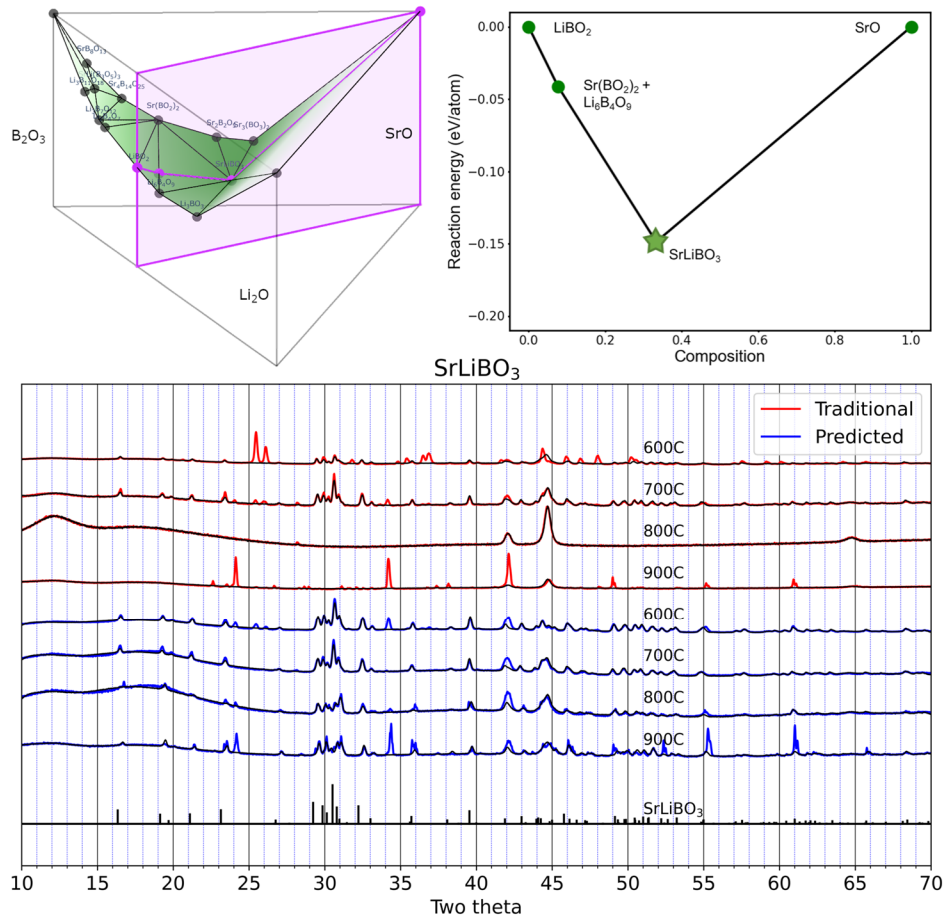


Table 1. Temperature, XRD intensities, and phase fraction of traditional and predicted reactions.

Compound	Precursor type	Precursors	Temp (°C)	Target intensity (e6)	Residual intensity (e6)	Target phase fraction
SrLiBO <sub>3</sub>	Traditional	Li <sub>2</sub> CO <sub>3</sub> , SrO, B <sub>2</sub> O <sub>3</sub>	600	1.02	1.98	0.34
			700	1.22	0.58	0.68
			800	0.00	0.25	0.00
			900	0.00	1.00	0.00
	Predicted	SrO, LiBO <sub>2</sub>	600	3.28	1.39	0.70
			700	1.47	0.77	0.66
			800	0.71	0.70	0.50
			900	0.92	0.81	0.53

Table 2. Candidate pairwise reactions evaluated using our precursor selection principles

Pairwise	Deepest	Reaction energy	Competing Phases	Inverse hull energy	Reaction	Best
Y	Y	-0.078	0	-0.078	0.5 Li <sub>2</sub> O + 0.5 Sr <sub>2</sub> B <sub>2</sub> O <sub>5</sub> → SrLiBO <sub>3</sub>	N
Y	Y	-0.023	0	-0.023	0.33 Li <sub>3</sub> BO <sub>3</sub> + 0.33 Sr <sub>3</sub> (BO <sub>3</sub> ) <sub>2</sub> → SrLiBO <sub>3</sub>	N
Y	Y	-0.149	1	-0.119	LiBO <sub>2</sub> + SrO → SrLiBO <sub>3</sub>	Y

## Li<sub>3</sub>Pr<sub>2</sub>(BO<sub>3</sub>)<sub>3</sub>

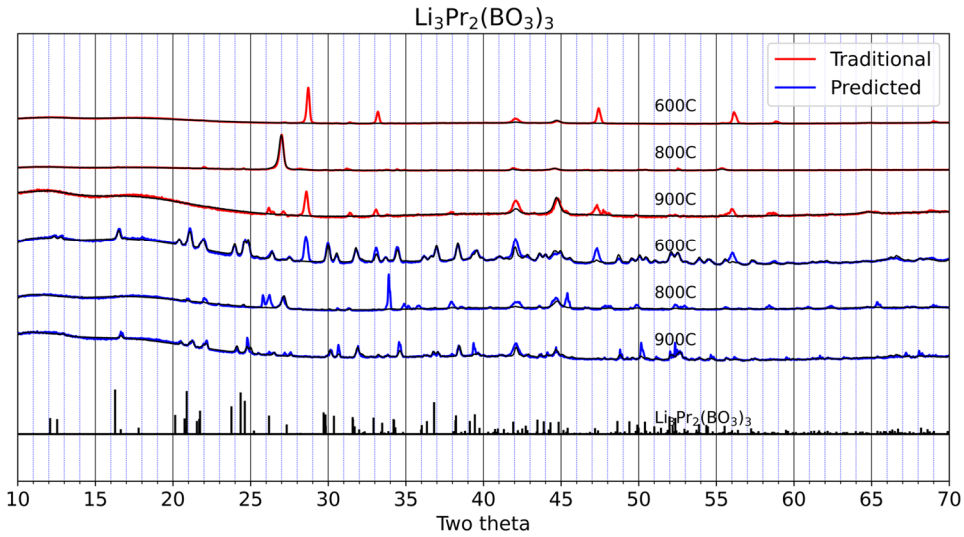
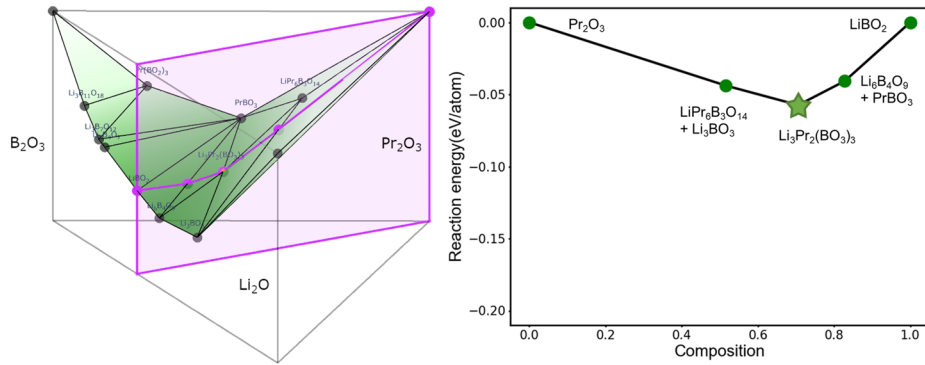


Table 1. Temperature, XRD intensities, and phase fraction of traditional and predicted reactions.

Compound	Precursor type	Precursors	Temp (°C)	Target intensity (e6)	Residual intensity (e6)	Target phase fraction
Li <sub>3</sub> Pr <sub>2</sub> (BO <sub>3</sub> ) <sub>3</sub>	Traditional	Li <sub>2</sub> CO <sub>3</sub> ,	600	0.00	1.32	0.00
		Pr <sub>6</sub> O <sub>11</sub> ,	800	0.08	0.53	0.13
		B <sub>2</sub> O <sub>3</sub>	900	0.00	0.48	0.00
	Predicted	Pr <sub>6</sub> O <sub>11</sub> ,	600	1.40	0.61	0.70
		800	0.06	0.55	0.10	
		LiBO <sub>2</sub>	900	0.52	0.43	0.55

Table 2. Candidate pairwise reactions evaluated using our precursor selection principles

Pairwise	Deepest	Reaction energy	Competing Phases	Inverse hull energy	Reaction	Best
Y	Y	-0.057	2	-0.015	3 LiBO <sub>2</sub> + Pr <sub>2</sub> O <sub>3</sub> → Li <sub>3</sub> Pr <sub>2</sub> (BO <sub>3</sub> ) <sub>3</sub>	Y
Y	Y	-0.007	0	-0.007	2 PrBO <sub>3</sub> + Li <sub>3</sub> BO <sub>3</sub> → Li <sub>3</sub> Pr <sub>2</sub> (BO <sub>3</sub> ) <sub>3</sub>	N

# LiGeBO<sub>4</sub>

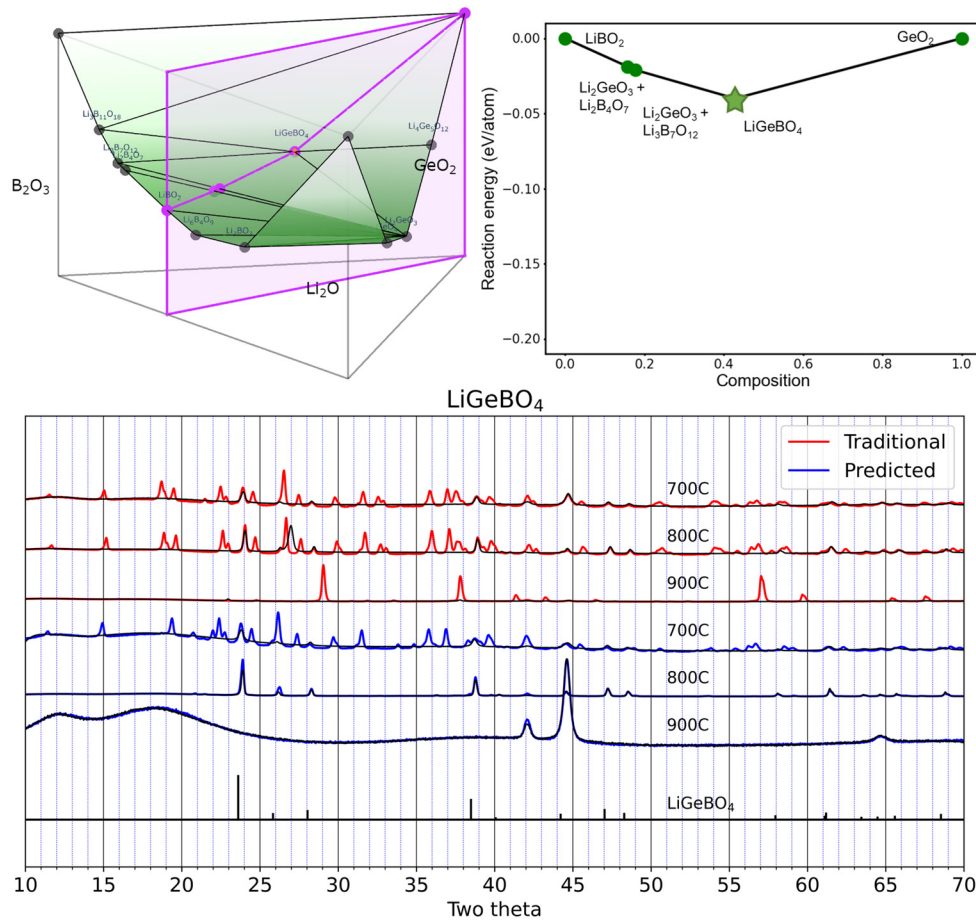


Table 1. Temperature, XRD intensities, and phase fraction of traditional and predicted reactions.

Compound	Precursor type	Precursors	Temp (°C)	Target intensity (e6)	Residual intensity (e6)	Target phase fraction
LiGeBO <sub>4</sub>	Traditional	Li <sub>2</sub> CO <sub>3</sub> ,	700	0.44	2.80	0.14
		GeO <sub>2</sub> ,	800	0.96	5.36	0.15
		B <sub>2</sub> O <sub>3</sub>	900	0.16	3.21	0.05
	Predicted	GeO <sub>2</sub> ,	700	0.58	3.17	0.15
		LiBO <sub>2</sub>	800	3.80	2.25	0.63
			900	0.00	0.41	0.00

Table 2. Candidate pairwise reactions evaluated using our precursor selection principles

Pairwise	Deepest	Reaction energy	Competing Phases	Inverse hull energy	Reaction	Best
Y	Y	-0.04	2	-0.025	LiBO <sub>2</sub> + GeO <sub>2</sub> → LiGeBO <sub>4</sub>	Y

# K<sub>3</sub>LiP<sub>2</sub>O<sub>7</sub>

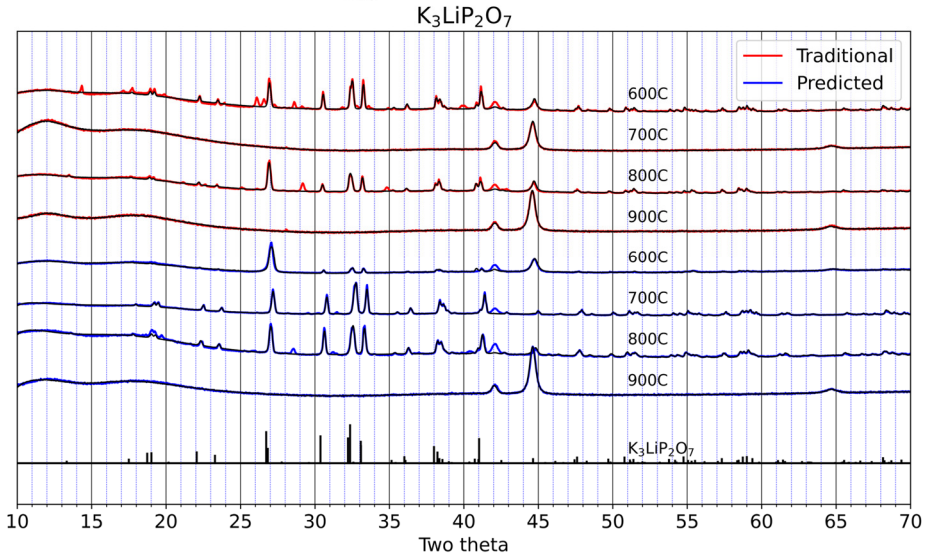
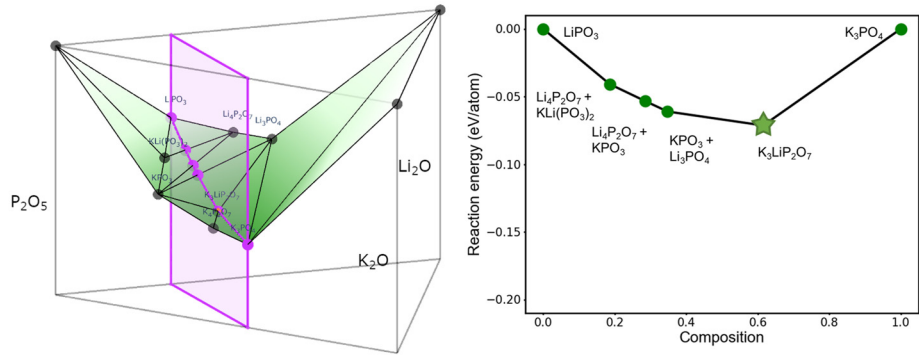


Table 1. Temperature, XRD intensities, and phase fraction of traditional and predicted reactions.

Compound	Precursor type	Precursors	Temp (°C)	Target intensity (e6)	Residual intensity (e6)	Target phase fraction
K <sub>3</sub> LiP <sub>2</sub> O <sub>7</sub>	Traditional	K <sub>2</sub> CO <sub>3</sub> , Li <sub>2</sub> CO <sub>3</sub> , NH <sub>4</sub> H <sub>2</sub> PO <sub>4</sub>	600	0.96	0.71	0.58
			700	0.00	0.94	0.00
			800	0.90	0.56	0.62
			900	0.00	0.19	0.02
	Predicted	K <sub>3</sub> PO <sub>4</sub> , LiPO <sub>3</sub>	600	0.32	0.54	0.37
			700	1.17	0.60	0.66
			800	1.05	0.54	0.66
			900	0.01	0.21	0.05

Table 2. Candidate pairwise reactions evaluated using our precursor selection principles

Pairwise	Deepest	Reaction energy	Competing Phases	Inverse hull energy	Reaction	Best
Y	N	-0.305	4	-0.035	KLi(PO <sub>3</sub> ) <sub>2</sub> + K <sub>2</sub> O → K <sub>3</sub> LiP <sub>2</sub> O <sub>7</sub>	N
Y	Y	-0.071	3	-0.035	K <sub>3</sub> PO <sub>4</sub> + LiPO <sub>3</sub> → K <sub>3</sub> LiP <sub>2</sub> O <sub>7</sub>	Y
Y	Y	-0.032	1	-0.026	0.75 K <sub>4</sub> P <sub>2</sub> O <sub>7</sub> + 0.25 Li <sub>4</sub> P <sub>2</sub> O <sub>7</sub> → K <sub>3</sub> LiP <sub>2</sub> O <sub>7</sub>	N

## Li<sub>3</sub>Sc<sub>2</sub>(PO<sub>4</sub>)<sub>3</sub>

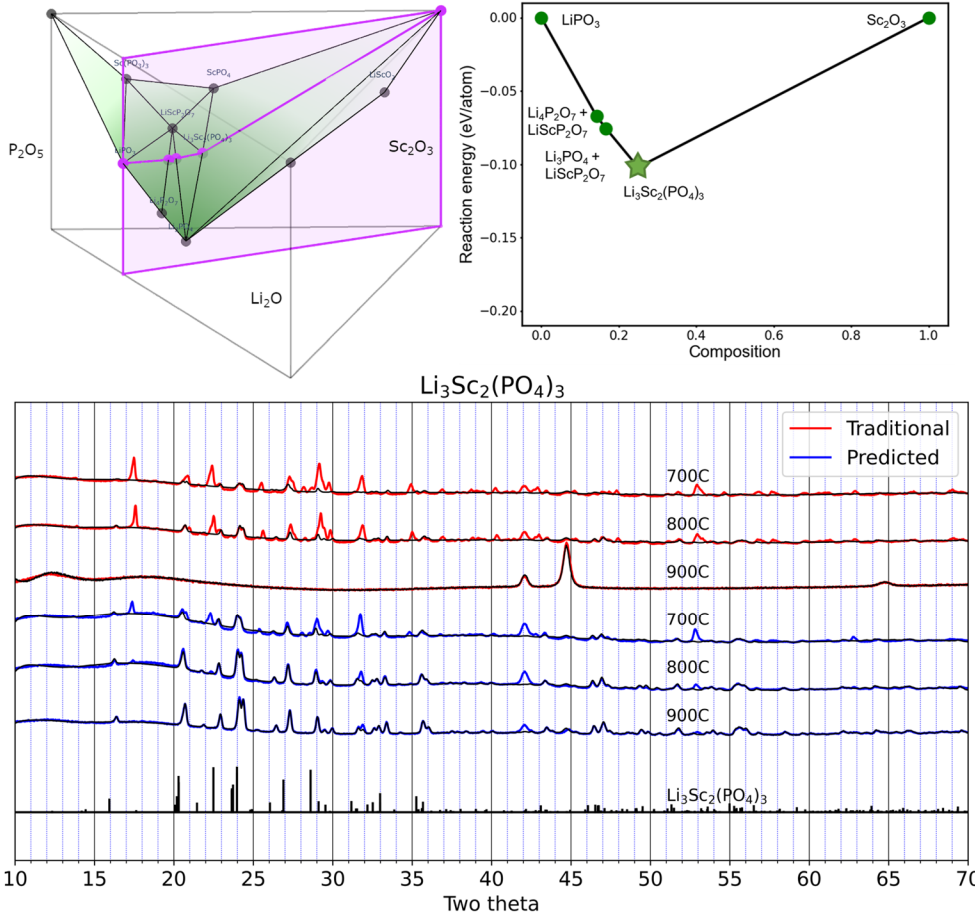


Table 1. Temperature, XRD intensities, and phase fraction of traditional and predicted reactions.

Compound	Precursor type	Precursors	Temp (°C)	Target intensity (e6)	Residual intensity (e6)	Target phase fraction
Li <sub>3</sub> Sc <sub>2</sub> (PO <sub>4</sub> ) <sub>3</sub>	Traditional	Sc <sub>2</sub> O <sub>3</sub> ,	700	0.24	1.35	0.15
		Li <sub>2</sub> CO <sub>3</sub> ,	800	0.46	1.20	0.28
		NH <sub>4</sub> H <sub>2</sub> PO <sub>4</sub>	900	0.01	0.23	0.04
	Predicted	Sc <sub>2</sub> O <sub>3</sub> ,	700	0.72	1.37	0.34
		LiPO <sub>3</sub> ,	800	1.64	0.95	0.63
		LiPO <sub>3</sub>	900	1.09	0.26	0.81

Table 2. Candidate pairwise reactions evaluated using our precursor selection principles

Pairwise	Deepest	Reaction energy	Competing Phases	Inverse hull energy	Reaction	Best
Y	Y	-0.102	2	-0.034	Sc <sub>2</sub> O <sub>3</sub> + 3 LiPO <sub>3</sub> → Li <sub>3</sub> Sc <sub>2</sub> (PO <sub>4</sub> ) <sub>3</sub>	Y
Y	Y	-0.013	0	-0.013	2 ScPO <sub>4</sub> + Li <sub>3</sub> PO <sub>4</sub> → Li <sub>3</sub> Sc <sub>2</sub> (PO <sub>4</sub> ) <sub>3</sub>	N

## Li<sub>3</sub>V<sub>2</sub>(PO<sub>4</sub>)<sub>3</sub>

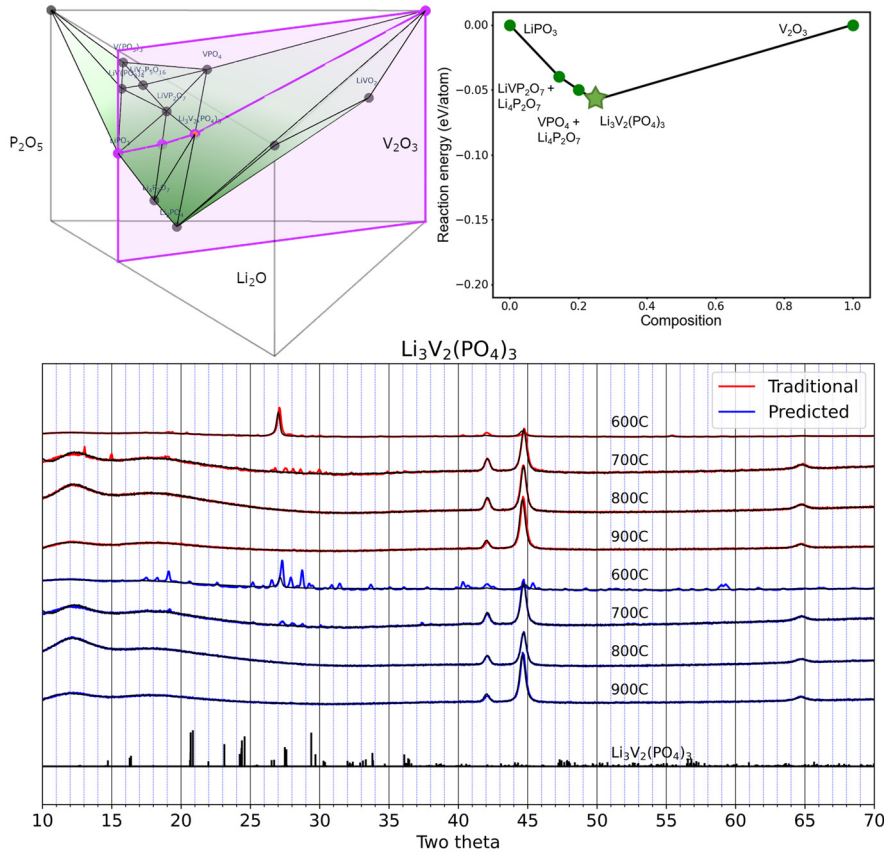


Table 1. Temperature, XRD intensities, and phase fraction of traditional and predicted reactions.

Compound	Precursor type	Precursors	Temp (°C)	Target intensity (e6)	Residual intensity (e6)	Target phase fraction
Li <sub>3</sub> V <sub>2</sub> (PO <sub>4</sub> ) <sub>3</sub>	Traditional	V <sub>2</sub> O <sub>3</sub> , Li <sub>2</sub> CO <sub>3</sub> , NH <sub>4</sub> H <sub>2</sub> PO <sub>4</sub>	600	0.00	0.84	0.00
			700	0.00	0.67	0.00
			800	0.00	0.36	0.00
			900	0.01	0.24	0.06
	Predicted	V <sub>2</sub> O <sub>3</sub> , LiPO <sub>3</sub>	600	0.00	1.32	0.00
			700	0.00	1.07	0.00
			800	0.00	0.27	0.00
			900	0.02	0.24	0.07

Table 2. Candidate pairwise reactions evaluated using our precursor selection principles

Pairwise	Deepest	Reaction energy	Competing Phases	Inverse hull energy	Reaction	Best
Y	Y	-0.062	1	-0.024	V <sub>2</sub> O <sub>3</sub> + 3 LiPO <sub>3</sub> → Li <sub>3</sub> V <sub>2</sub> (PO <sub>4</sub> ) <sub>3</sub>	Y
Y	N	-0.037	16	-0.008	0.25 Li <sub>11</sub> V <sub>8</sub> (PO <sub>4</sub> ) <sub>12</sub> + 0.25 Li → Li <sub>3</sub> V <sub>2</sub> (PO <sub>4</sub> ) <sub>3</sub>	N
Y	N	-0.338	18	-0.008	LiV <sub>2</sub> (PO <sub>4</sub> ) <sub>3</sub> + 2 Li → Li <sub>3</sub> V <sub>2</sub> (PO <sub>4</sub> ) <sub>3</sub>	N
Y	Y	-0.006	0	-0.006	2 VPO <sub>4</sub> + Li <sub>3</sub> PO <sub>4</sub> → Li <sub>3</sub> V <sub>2</sub> (PO <sub>4</sub> ) <sub>3</sub>	N

## KLi(PO<sub>3</sub>)<sub>2</sub>

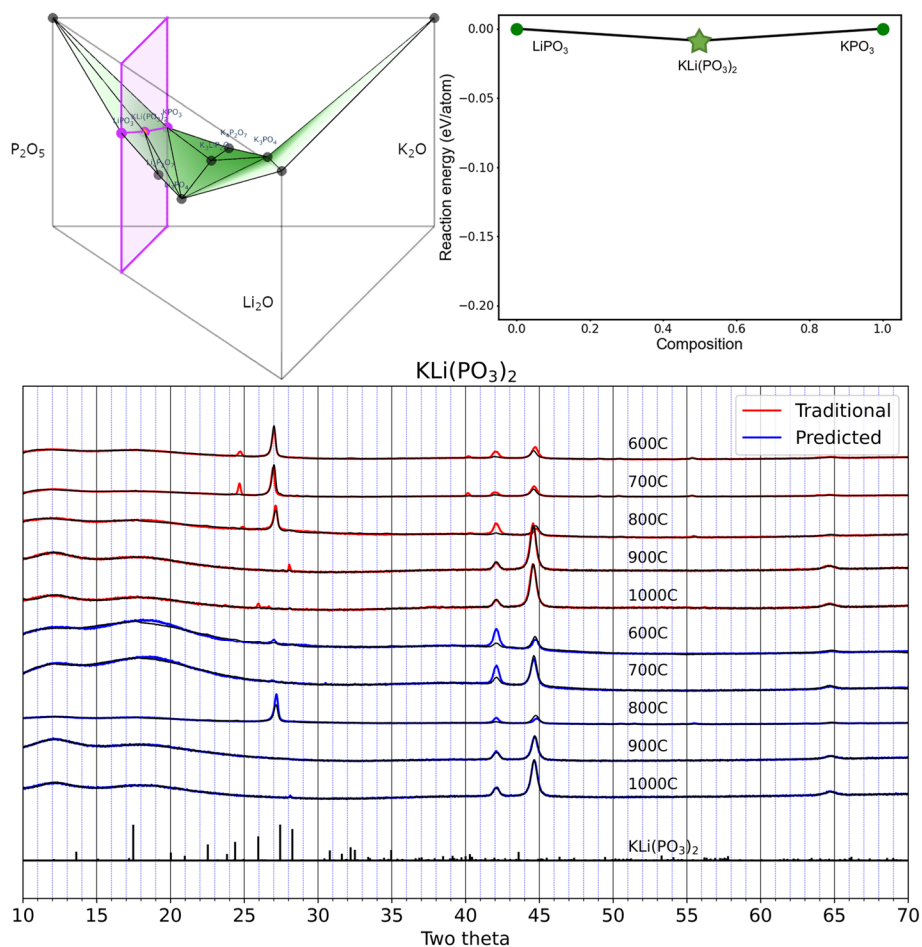


Table 1. Temperature, XRD intensities, and phase fraction of traditional and predicted reactions.

Compound	Precursor type	Precursors	Temp (°C)	Target intensity (e6)	Residual intensity (e6)	Target phase fraction
KLi(PO <sub>3</sub> ) <sub>2</sub>	Traditional	K <sub>2</sub> CO <sub>3</sub> , Li <sub>2</sub> CO <sub>3</sub> , NH <sub>4</sub> H <sub>2</sub> PO <sub>4</sub>	600	0.25	0.51	0.33
			700	0.15	0.81	0.16
			800	0.22	0.41	0.35
			900	0.03	0.24	0.12
			1000	0.02	0.25	0.09
	Predicted	KPO <sub>3</sub> , LiPO <sub>3</sub>	600	0.27	0.75	0.27
			700	0.12	0.57	0.17
			800	0.33	0.54	0.38

Table 2. Candidate pairwise reactions evaluated using our precursor selection principles

Pairwise	Deepest	Reaction energy	Competing Phases	Inverse hull energy	Reaction	Best
Y	Y	-0.009	0	-0.009	KPO <sub>3</sub> + LiPO <sub>3</sub> → KLi(PO <sub>3</sub> ) <sub>2</sub>	Y

## Li<sub>2</sub>TiSiO<sub>5</sub>

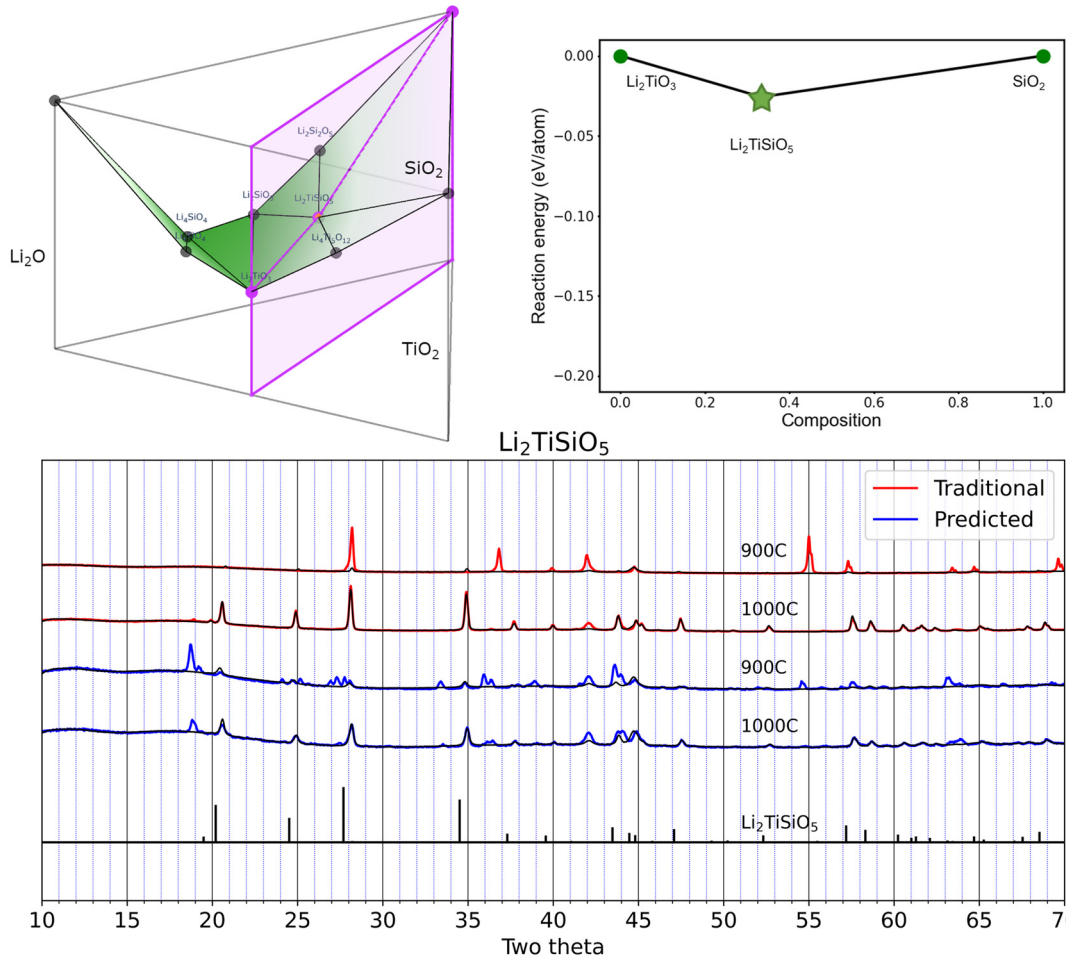


Table 1. Temperature, XRD intensities, and phase fraction of traditional and predicted reactions.

Compound	Precursor type	Precursors	Temp (°C)	Target intensity (e6)	Residual intensity (e6)	Target phase fraction
Li <sub>2</sub> TiSiO <sub>5</sub>	Traditional	SiO <sub>2</sub> , TiO <sub>2</sub> ,	900	0.06	0.68	0.08
		Li <sub>2</sub> CO <sub>3</sub>	1000	0.84	0.28	0.75
	Predicted	SiO <sub>2</sub> ,	900	0.14	0.62	0.18
		Li <sub>2</sub> TiO <sub>3</sub>	1000	0.34	0.33	0.51

Table 2. Candidate pairwise reactions evaluated using our precursor selection principles

Pairwise	Deepest	Reaction energy	Competing Phases	Inverse hull energy	Reaction	Best
Y	Y	-0.026	0	-0.026	Li <sub>2</sub> TiO <sub>3</sub> + SiO <sub>2</sub> → Li <sub>2</sub> TiSiO <sub>5</sub>	Y
Y	Y	-0.014	0	-0.014	Li <sub>2</sub> SiO <sub>3</sub> + TiO <sub>2</sub> → Li <sub>2</sub> TiSiO <sub>5</sub>	N

## LiNbGeO<sub>5</sub>

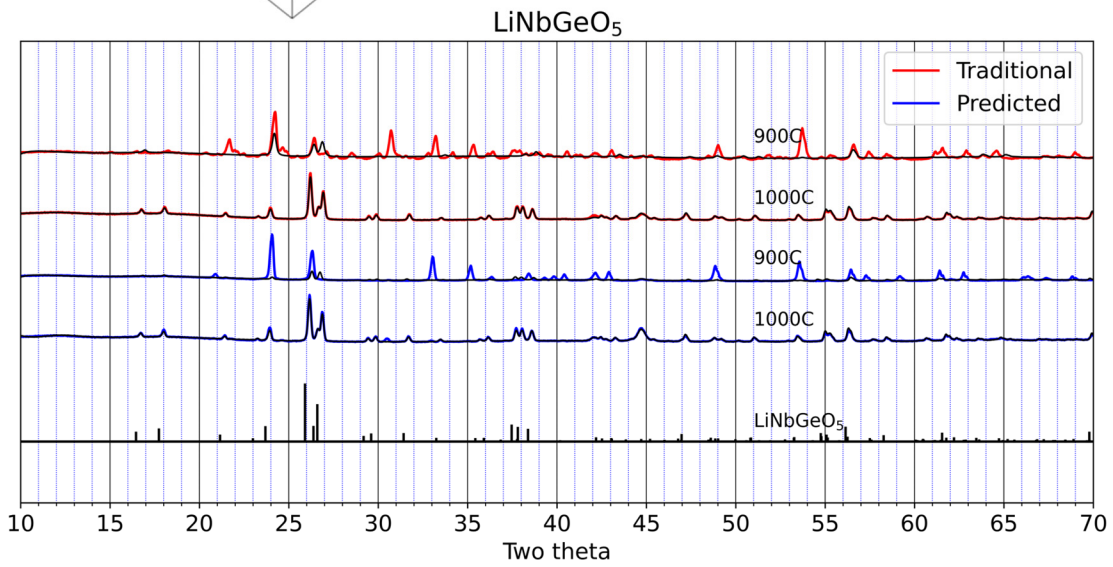
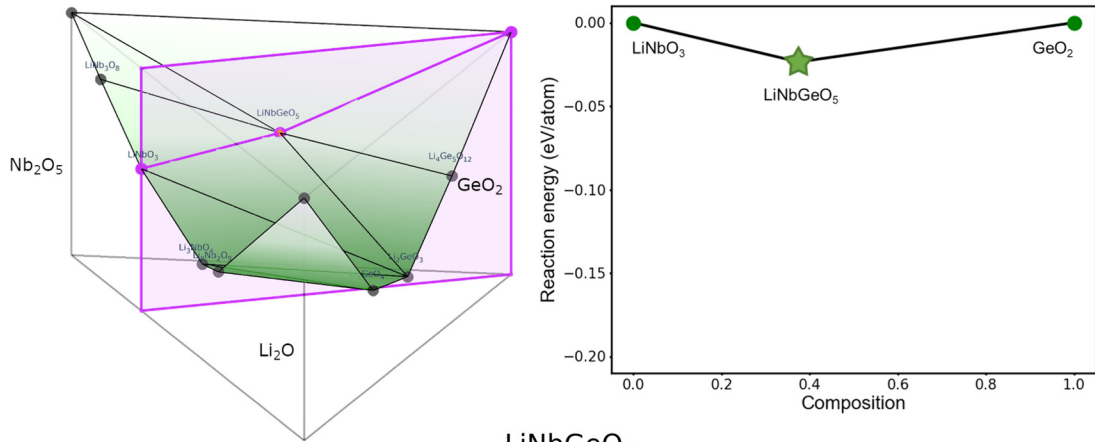


Table 1. Temperature, XRD intensities, and phase fraction of traditional and predicted reactions.

Compound	Precursor type	Precursors	Temp (°C)	Target intensity (e6)	Residual intensity (e6)	Target phase fraction
LiNbGeO <sub>5</sub>	Traditional	GeO <sub>2</sub> , Li <sub>2</sub> CO <sub>3</sub> , Nb <sub>2</sub> O <sub>5</sub>	900	0.47	1.52	0.24
			1000	1.33	0.24	0.85
	Predicted	GeO <sub>2</sub> , LiNbO <sub>3</sub>	900	0.41	1.79	0.19
			1000	1.25	0.36	0.78

Table 2. Candidate pairwise reactions evaluated using our precursor selection principles

Pairwise	Deepest	Reaction energy	Competing Phases	Inverse hull energy	Reaction	Best
Y	Y	-0.024	0	-0.024	GeO <sub>2</sub> + LiNbO <sub>3</sub> → LiNbGeO <sub>5</sub>	Y



## Li<sub>3</sub>Fe<sub>2</sub>(PO<sub>4</sub>)<sub>3</sub>

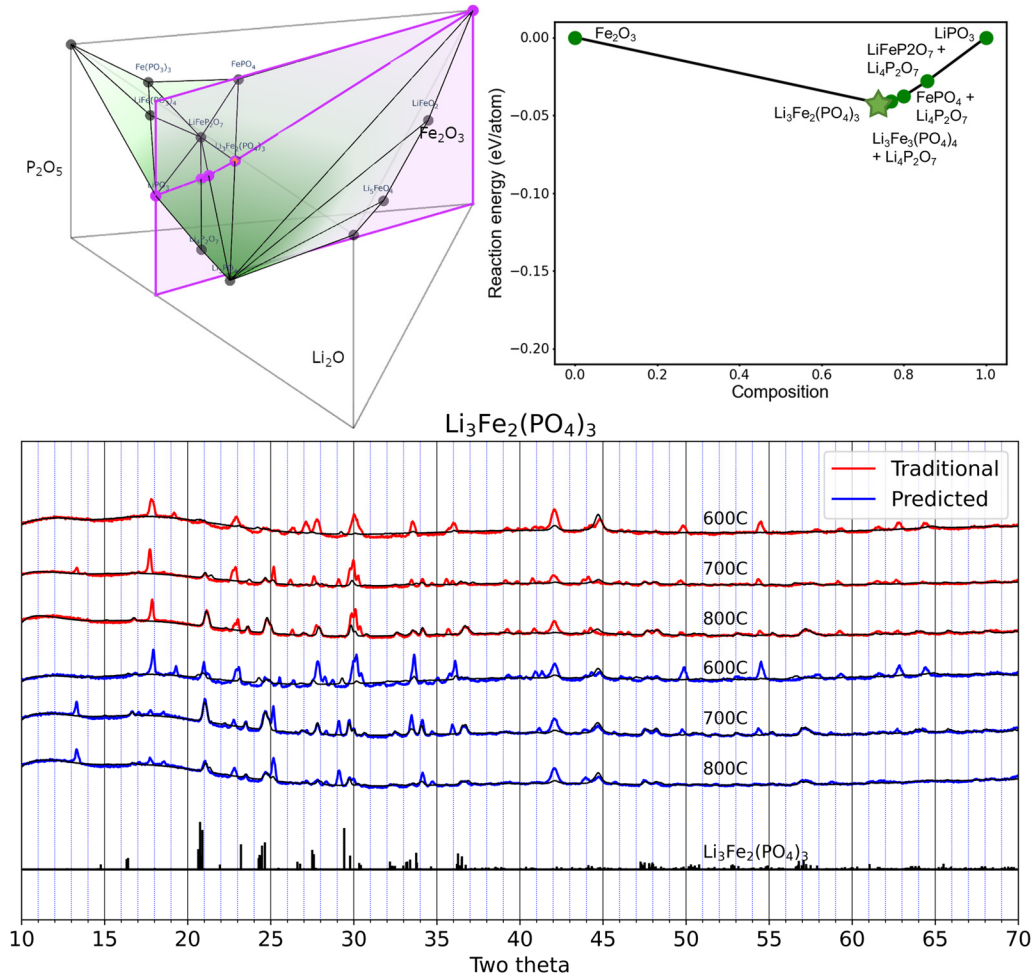


Table 1. Temperature, XRD intensities, and phase fraction of traditional and predicted reactions.

Compound	Precursor type	Precursors	Temp (°C)	Target intensity (e6)	Residual intensity (e6)	Target phase fraction
Li <sub>3</sub> Fe <sub>2</sub> (PO <sub>4</sub> ) <sub>3</sub>	Traditional	Fe <sub>2</sub> O <sub>3</sub> , Li <sub>2</sub> CO <sub>3</sub> , NH <sub>4</sub> H <sub>2</sub> PO <sub>4</sub>	600	0.09	0.88	0.09
			700	0.39	1.20	0.25
			800	0.59	0.77	0.43
	Predicted	Fe <sub>2</sub> O <sub>3</sub> , LiPO <sub>3</sub>	600	0.24	1.20	0.17
			700	0.69	0.78	0.47
			800	0.40	0.75	0.35

Table 2. Candidate pairwise reactions evaluated using our precursor selection principles

Pairwise	Deepest	Reaction energy	Competing Phases	Inverse hull energy	Reaction	Best
Y	N	-0.195	6	-0.04	Li <sub>2</sub> O <sub>2</sub> + LiFe <sub>2</sub> P <sub>3</sub> O <sub>10</sub> → Li <sub>3</sub> Fe <sub>2</sub> (PO <sub>4</sub> ) <sub>3</sub>	N
Y	Y	-0.048	2	-0.008	Fe <sub>2</sub> O <sub>3</sub> + 3 LiPO <sub>3</sub> → Li <sub>3</sub> Fe <sub>2</sub> (PO <sub>4</sub> ) <sub>3</sub>	Y
Y	Y	-0.005	0	-0.005	Li <sub>3</sub> PO <sub>4</sub> + 2 FePO <sub>4</sub> → Li <sub>3</sub> Fe <sub>2</sub> (PO <sub>4</sub> ) <sub>3</sub>	N

## KBaPO<sub>4</sub>

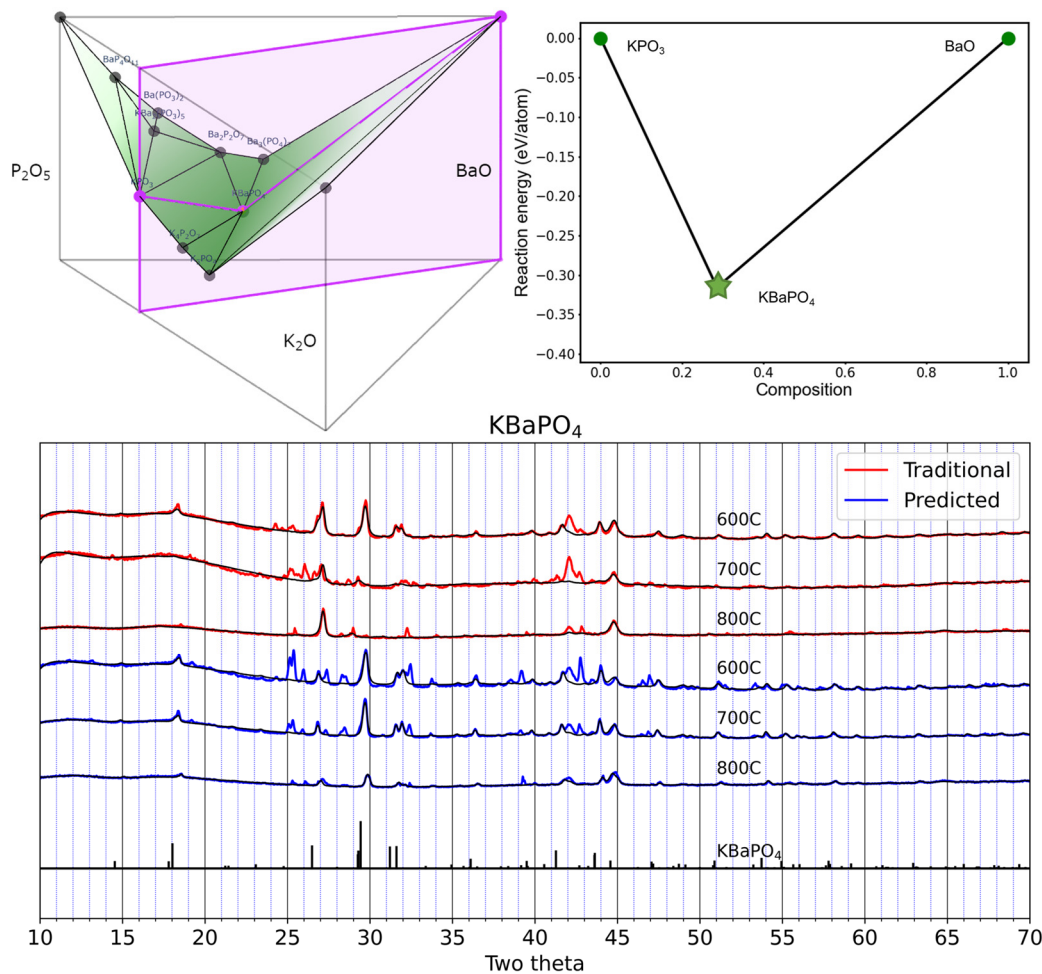


Table 1. Temperature, XRD intensities, and phase fraction of traditional and predicted reactions.

Compound	Precursor type	Precursors	Temp (°C)	Target intensity (e6)	Residual intensity (e6)	Target phase fraction
KBaPO <sub>4</sub>	Traditional	BaO, K <sub>2</sub> CO <sub>3</sub> , NH <sub>4</sub> H <sub>2</sub> PO <sub>4</sub>	600	0.88	0.62	0.59
			700	0.17	0.71	0.20
			800	0.13	0.28	0.32
	Predicted	BaO, KPO <sub>3</sub>	600	0.82	0.97	0.46
			700	1.03	0.81	0.56
			800	0.23	0.22	0.52

Table 2. Candidate pairwise reactions evaluated using our precursor selection principles

Pairwise	Deepest	Reaction energy	Competing Phases	Inverse hull energy	Reaction	Best
Y	Y	-0.315	0	-0.315	BaO + KPO <sub>3</sub> → KBaPO <sub>4</sub>	Y
Y	N	-0.244	1	-0.119	0.5 K <sub>2</sub> O + 0.5 Ba <sub>2</sub> P <sub>2</sub> O <sub>7</sub> → KBaPO <sub>4</sub>	N
Y	Y	-0.036	0	-0.036	0.33 K <sub>3</sub> PO <sub>4</sub> + 0.33 Ba <sub>3</sub> (PO <sub>4</sub> ) <sub>2</sub> → KBaPO <sub>4</sub>	N

# BaNaBO<sub>3</sub>

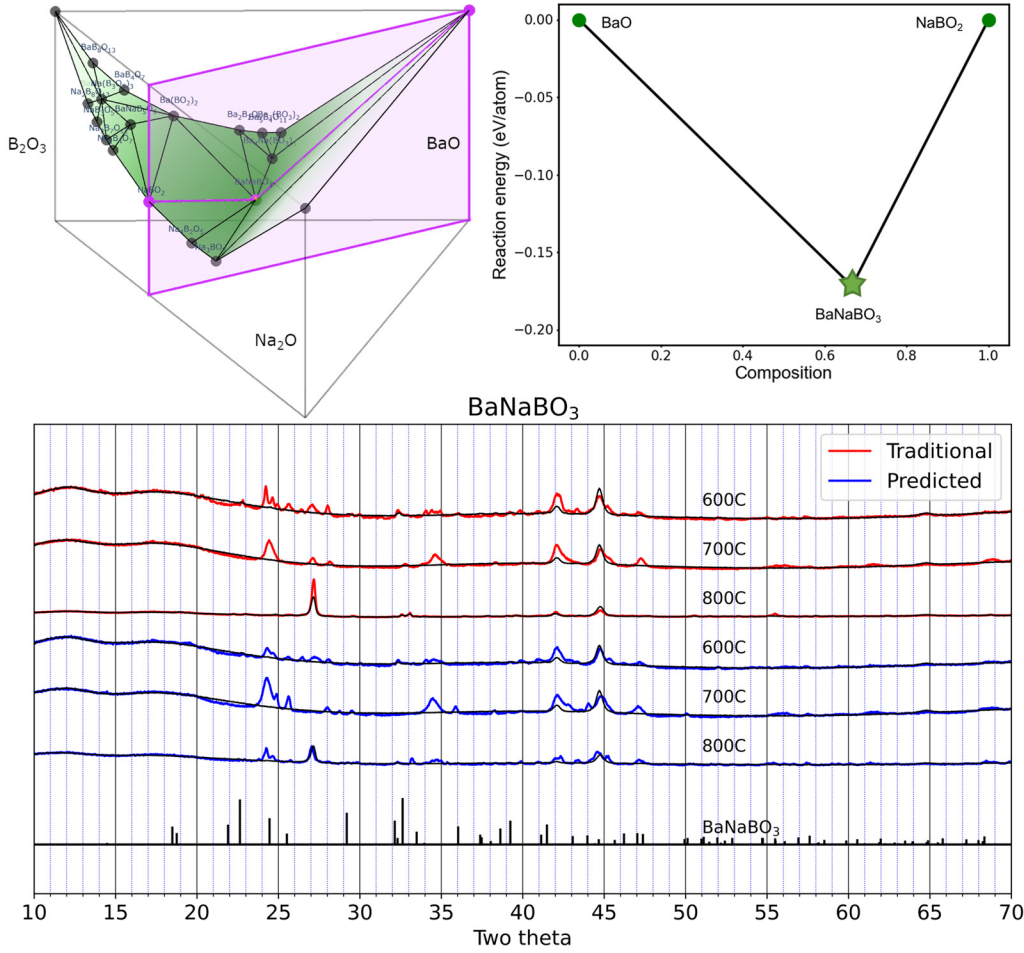


Table 1. Temperature, XRD intensities, and phase fraction of traditional and predicted reactions.

Compound	Precursor type	Precursors	Temp (°C)	Target intensity (e6)	Residual intensity (e6)	Target phase fraction
BaNaBO <sub>3</sub>	Traditional	B <sub>2</sub> O <sub>3</sub> , BaO, Na <sub>2</sub> CO <sub>3</sub>	600	0.06	0.66	0.08
			700	0.00	0.68	0.00
			800	0.17	0.34	0.33
	Predicted	BaO, NaBO <sub>2</sub>	600	0.03	0.55	0.05
			700	0.00	0.95	0.00
			800	0.02	0.37	0.05

Table 2. Candidate pairwise reactions evaluated using our precursor selection principles

Pairwise	Deepest	Reaction energy	Competing Phases	Inverse hull energy	Reaction	Best
Y	Y	-0.172	0	-0.172	NaBO <sub>2</sub> + BaO → BaNaBO <sub>3</sub>	Y
Y	Y	-0.139	1	-0.089	0.5 Ba <sub>2</sub> B <sub>2</sub> O <sub>5</sub> + 0.5 Na <sub>2</sub> O → BaNaBO <sub>3</sub>	N
Y	Y	-0.048	1	-0.031	0.33 Ba <sub>3</sub> (BO <sub>3</sub> ) <sub>2</sub> + 0.33 Na <sub>3</sub> BO <sub>3</sub> → BaNaBO <sub>3</sub>	N
Y	Y	-0.031	0	-0.031	0.25 Ba <sub>4</sub> Na(BO <sub>3</sub> ) <sub>3</sub> + 0.25 Na <sub>3</sub> BO <sub>3</sub> → BaNaBO <sub>3</sub>	N

# KMgPO<sub>4</sub>

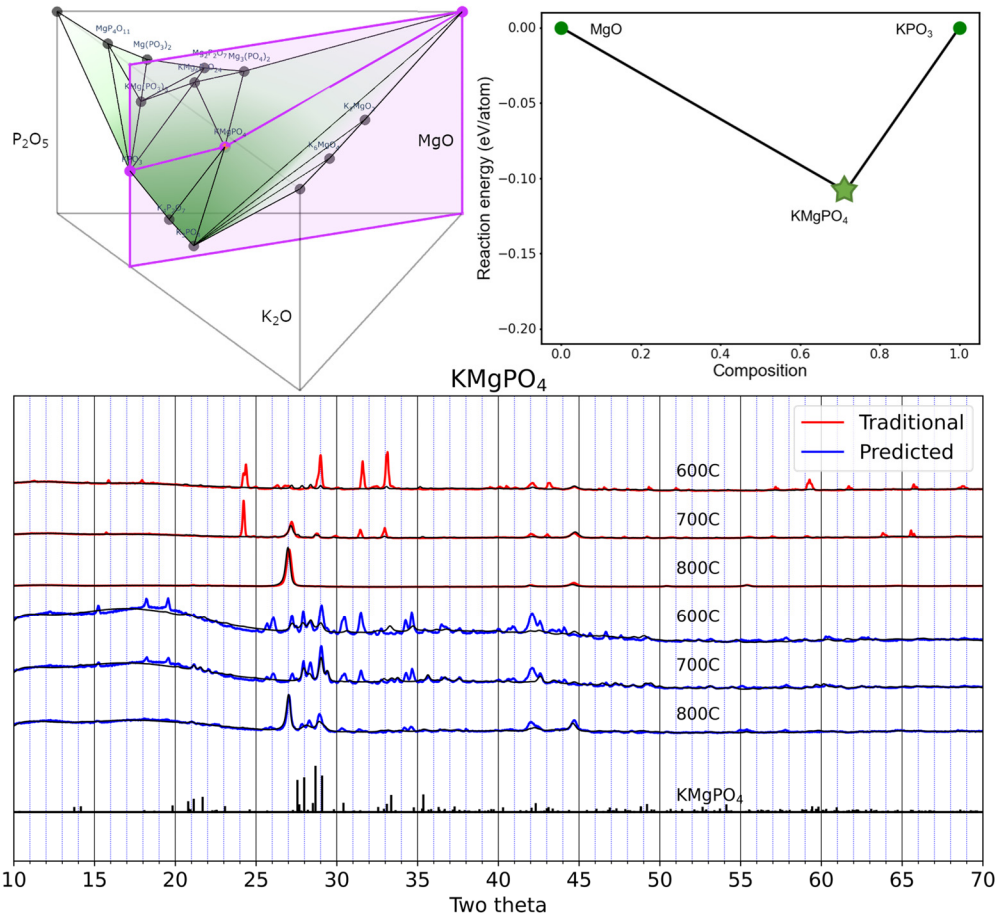


Table 1. Temperature, XRD intensities, and phase fraction of traditional and predicted reactions.

Compound	Precursor type	Precursors	Temp (°C)	Target intensity (e6)	Residual intensity (e6)	Target phase fraction
KMgPO <sub>4</sub>	Traditional	K <sub>2</sub> CO <sub>3</sub> , MgO, NH <sub>4</sub> H <sub>2</sub> PO <sub>4</sub>	600	0.29	1.56	0.15
			700	0.39	1.39	0.22
			800	0.07	0.62	0.11
	Predicted	KPO <sub>3</sub> , MgO	600	0.99	1.70	0.37
			700	1.29	1.53	0.46
			800	0.55	0.57	0.49

Table 2. Candidate pairwise reactions evaluated using our precursor selection principles

Pairwise	Deepest	Reaction energy	Competing Phases	Inverse hull energy	Reaction	Best
Y	Y	-0.123	0	-0.123	MgO + KPO <sub>3</sub> → KMgPO <sub>4</sub>	Y
Y	N	-0.377	4	-0.099	0.5 Mg(PO <sub>3</sub> ) <sub>2</sub> + 0.5 K <sub>2</sub> MgO <sub>2</sub> → KMgPO <sub>4</sub>	N
Y	N	-0.272	2	-0.095	0.143 K <sub>6</sub> MgO <sub>4</sub> + 0.143 KMg <sub>6</sub> P <sub>7</sub> O <sub>24</sub> → KMgPO <sub>4</sub>	N
Y	N	-0.303	4	-0.085	0.5 K <sub>2</sub> O + 0.5 Mg <sub>2</sub> P <sub>2</sub> O <sub>7</sub> → KMgPO <sub>4</sub>	N
Y	Y	-0.051	0	-0.051	0.33 K <sub>3</sub> PO <sub>4</sub> + 0.33 Mg <sub>3</sub> (PO <sub>4</sub> ) <sub>2</sub> → KMgPO <sub>4</sub>	N

## NaSrBO<sub>3</sub>

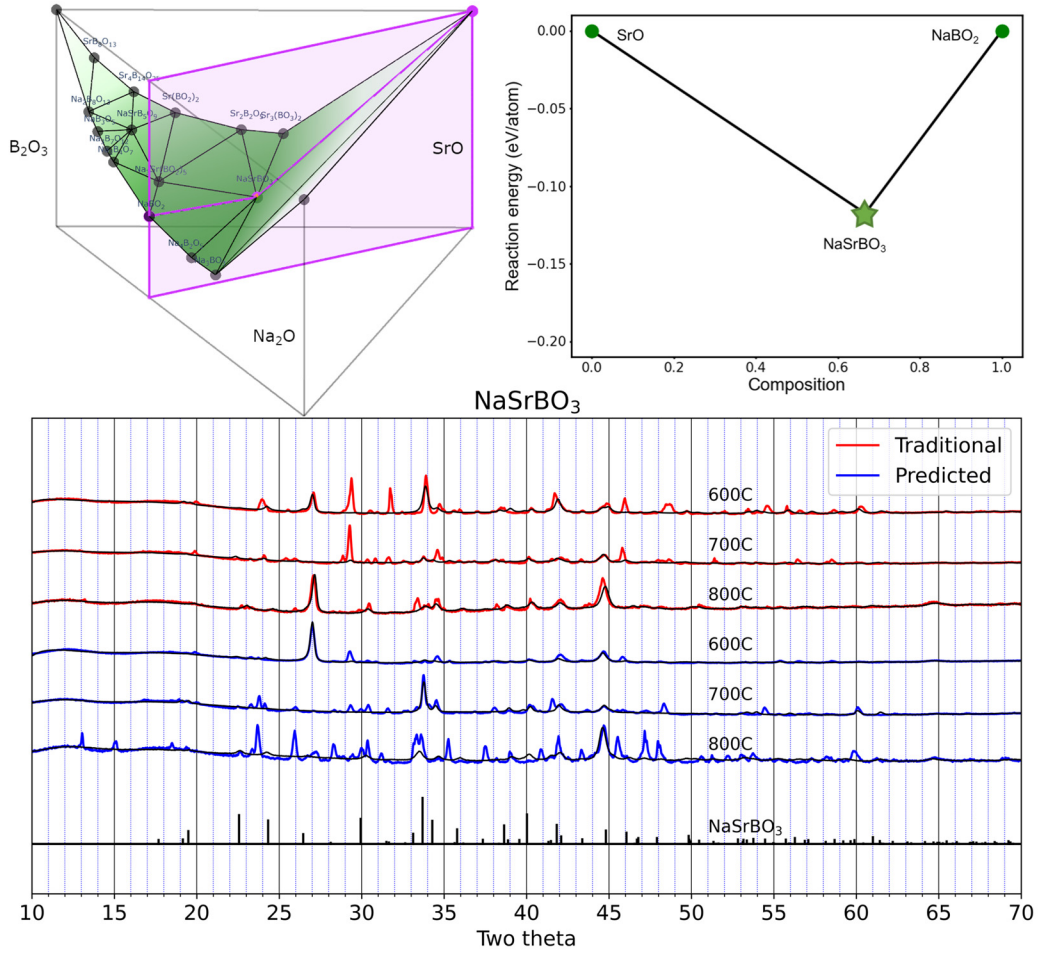


Table 1. Temperature, XRD intensities, and phase fraction of traditional and predicted reactions.

Compound	Precursor type	Precursors	Temp (°C)	Target intensity (e6)	Residual intensity (e6)	Target phase fraction
NaSrBO <sub>3</sub>	Traditional	B <sub>2</sub> O <sub>3</sub> , Na <sub>2</sub> CO <sub>3</sub> , SrO	600	1.13	1.58	0.42
			700	0.57	1.30	0.30
			800	0.57	0.57	0.50
	Predicted	NaBO <sub>2</sub> , SrO	600	0.49	0.92	0.35
			700	0.69	1.28	0.35
			800	0.49	1.19	0.29

Table 2. Candidate pairwise reactions evaluated using our precursor selection principles

Pairwise	Deepest	Reaction energy	Competing Phases	Inverse hull energy	Reaction	Best
Y	Y	-0.118	0	-0.118	NaBO <sub>2</sub> + SrO → NaSrBO <sub>3</sub>	Y
Y	N	-0.119	1	-0.057	0.5 Sr <sub>2</sub> B <sub>2</sub> O <sub>5</sub> + 0.5 Na <sub>2</sub> O → NaSrBO <sub>3</sub>	N
Y	Y	-0.02	0	-0.02	0.33 Sr <sub>3</sub> (BO <sub>3</sub> ) <sub>2</sub> + 0.33 Na <sub>3</sub> BO <sub>3</sub> → NaSrBO <sub>3</sub>	N

### $K_3Bi_2(PO_4)_3$

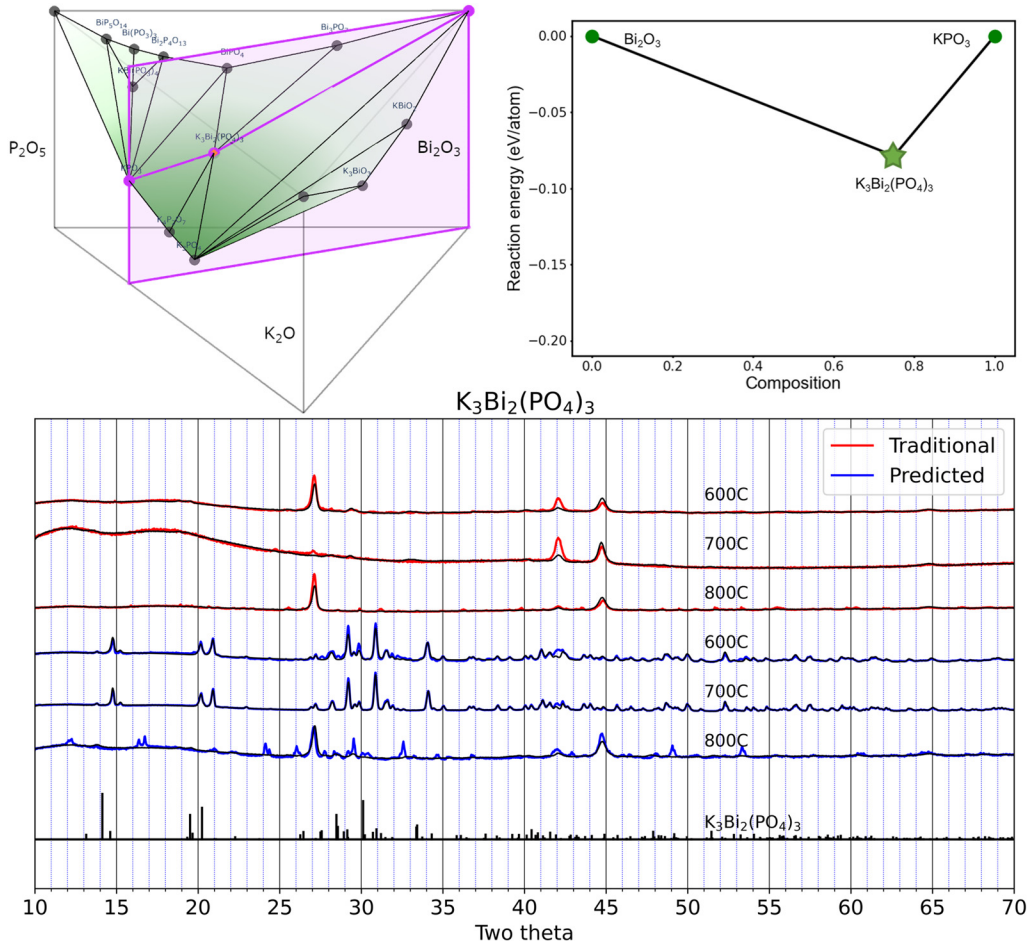


Table 1. Temperature, XRD intensities, and phase fraction of traditional and predicted reactions.

Compound	Precursor type	Precursors	Temp (°C)	Target intensity (e6)	Residual intensity (e6)	Target phase fraction
$K_3Bi_2(PO_4)_3$	Traditional	$Bi_2O_3, K_2CO_3, NH_4H_2PO_4$	600	0.56	0.60	0.48
			700	0.27	0.40	0.41
			800	0.07	0.43	0.14
	Predicted	$Bi_2O_3, KPO_3$	600	2.67	0.88	0.75
			700	3.37	0.58	0.85
			800	0.31	0.58	0.34

Table 2. Candidate pairwise reactions evaluated using our precursor selection principles

Pairwise	Deepest	Reaction energy	Competing Phases	Inverse hull energy	Reaction	Best
Y	Y	-0.079	0	-0.079	$3 KPO_3 + Bi_2O_3 \rightarrow K_3Bi_2(PO_4)_3$	Y
Y	Y	-0.3	5	-0.056	$Bi(PO_3)_3 + K_3BiO_3 \rightarrow K_3Bi_2(PO_4)_3$	N
Y	Y	-0.04	0	-0.04	$K_3PO_4 + 2 BiPO_4 \rightarrow K_3Bi_2(PO_4)_3$	N

## K<sub>2</sub>Zr(PO<sub>4</sub>)<sub>2</sub>

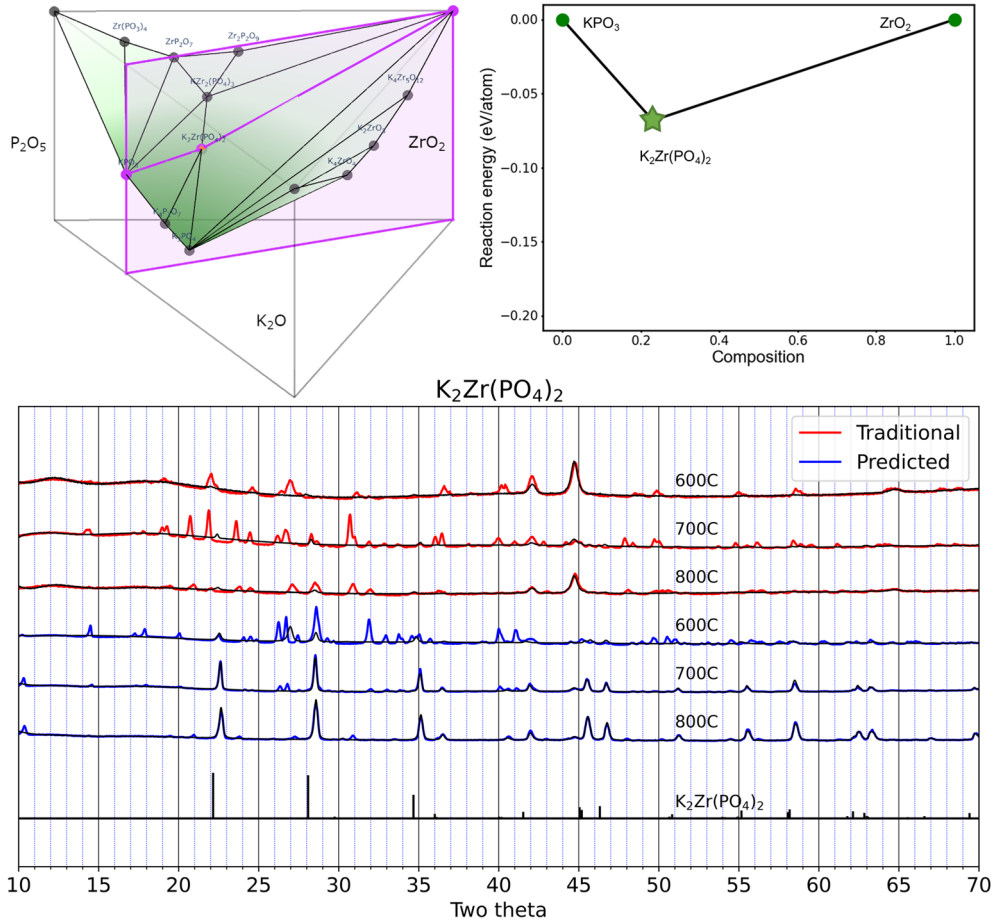


Table 1. Temperature, XRD intensities, and phase fraction of traditional and predicted reactions.

Compound	Precursor type	Precursors	Temp (°C)	Target intensity (e6)	Residual intensity (e6)	Target phase fraction
K <sub>2</sub> Zr(PO <sub>4</sub> ) <sub>2</sub>	Traditional	K <sub>2</sub> CO <sub>3</sub> , NH <sub>4</sub> H <sub>2</sub> PO <sub>4</sub> , ZrO <sub>2</sub>	600	0.04	0.62	0.06
			700	0.09	1.67	0.05
			800	0.06	0.44	0.12
	Predicted	KPO <sub>3</sub> , ZrO <sub>2</sub>	600	0.44	2.42	0.15
			700	1.31	0.92	0.59
			800	0.93	0.31	0.75

Table 2. Candidate pairwise reactions evaluated using our precursor selection principles

Pairwise	Deepest	Reaction energy	Competing Phases	Inverse hull energy	Reaction	Best
Y	Y	-0.068	0	-0.068	2 KPO <sub>3</sub> + ZrO <sub>2</sub> → K <sub>2</sub> Zr(PO <sub>4</sub> ) <sub>2</sub>	Y
Y	Y	-0.419	5	-0.045	P <sub>2</sub> O <sub>5</sub> + K <sub>2</sub> ZrO <sub>3</sub> → K <sub>2</sub> Zr(PO <sub>4</sub> ) <sub>2</sub>	N
Y	Y	-0.063	1	-0.03	0.5 K <sub>4</sub> P <sub>2</sub> O <sub>7</sub> + 0.5 Zr <sub>2</sub> P <sub>2</sub> O <sub>9</sub> → K <sub>2</sub> Zr(PO <sub>4</sub> ) <sub>2</sub>	N
Y	Y	-0.027	0	-0.027	0.5 K <sub>3</sub> PO <sub>4</sub> + 0.5 KZr <sub>2</sub> (PO <sub>4</sub> ) <sub>3</sub> → K <sub>2</sub> Zr(PO <sub>4</sub> ) <sub>2</sub>	N
Y	N	-0.338	5	-0.041	0.5 K <sub>4</sub> ZrO <sub>4</sub> + 0.5 Zr(PO <sub>3</sub> ) <sub>4</sub> → K <sub>2</sub> Zr(PO <sub>4</sub> ) <sub>2</sub>	N
Y	N	-0.34	5	-0.035	K <sub>2</sub> O + ZrP <sub>2</sub> O <sub>7</sub> → K <sub>2</sub> Zr(PO <sub>4</sub> ) <sub>2</sub>	N

### $K_3Al_2(PO_4)_3$

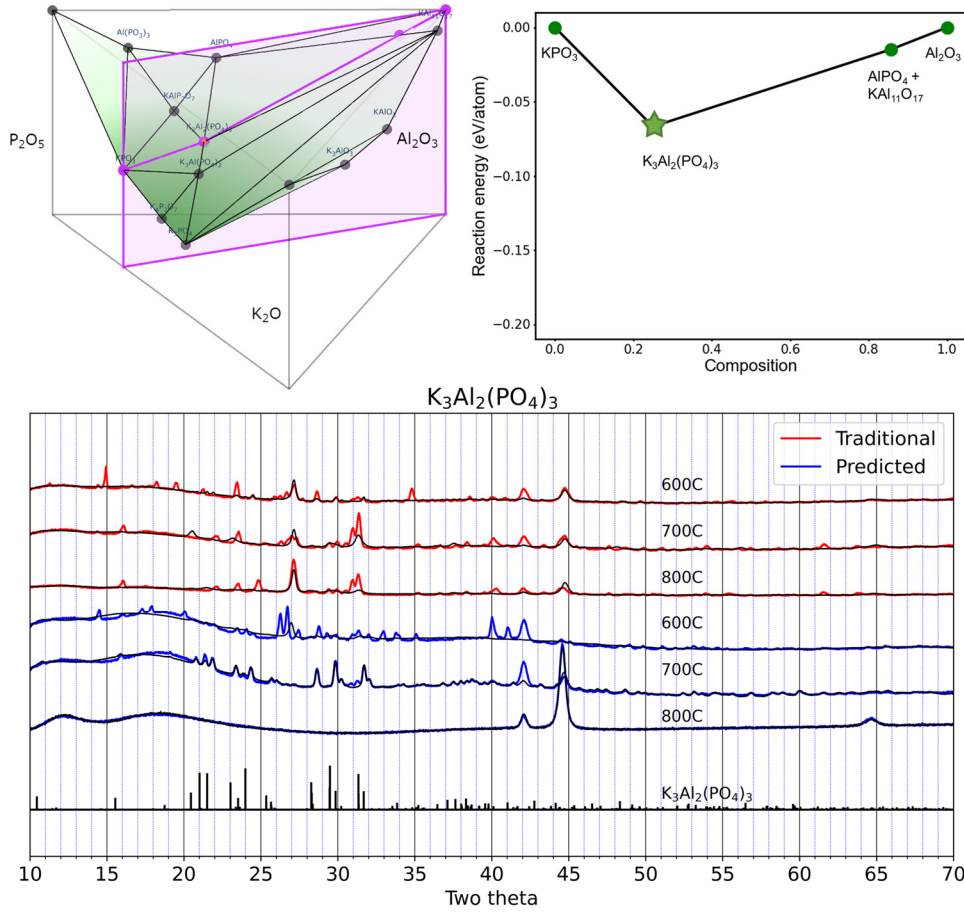


Table 1. Temperature, XRD intensities, and phase fraction of traditional and predicted reactions.

Compound	Precursor type	Precursors	Temp (°C)	Target intensity (e6)	Residual intensity (e6)	Target phase fraction
$K_3Al_2(PO_4)_3$	Traditional	$Al_2O_3, K_2CO_3, NH_4H_2PO_4$	600	0.17	0.78	0.18
			700	0.83	0.94	0.47
			800	0.40	0.63	0.39
	Predicted	$Al_2O_3, KPO_3$	600	0.52	1.44	0.27
			700	1.14	0.80	0.59
			800	0.04	0.31	0.11

Table 2. Candidate pairwise reactions evaluated using our precursor selection principles

Pairwise	Deepest	Reaction energy	Competing Phases	Inverse hull energy	Reaction	Best
Y	Y	-0.067	1	-0.062	$3 KPO_3 + Al_2O_3 \rightarrow K_3Al_2(PO_4)_3$	Y
Y	N	-0.121	3	-0.023	$1.5 KAIP_2O_7 + 0.5 K_3AlO_3 \rightarrow K_3Al_2(PO_4)_3$	N
Y	N	-0.301	4	-0.023	$K_3AlO_3 + Al(PO_3)_3 \rightarrow K_3Al_2(PO_4)_3$	N
Y	N	-0.053	1	-0.016	$K_3PO_4 + 2 AlPO_4 \rightarrow K_3Al_2(PO_4)_3$	N
Y	Y	-0.016	0	-0.016	$AlPO_4 + K_3Al(PO_4)_2 \rightarrow K_3Al_2(PO_4)_3$	N

# KTiPO<sub>5</sub>

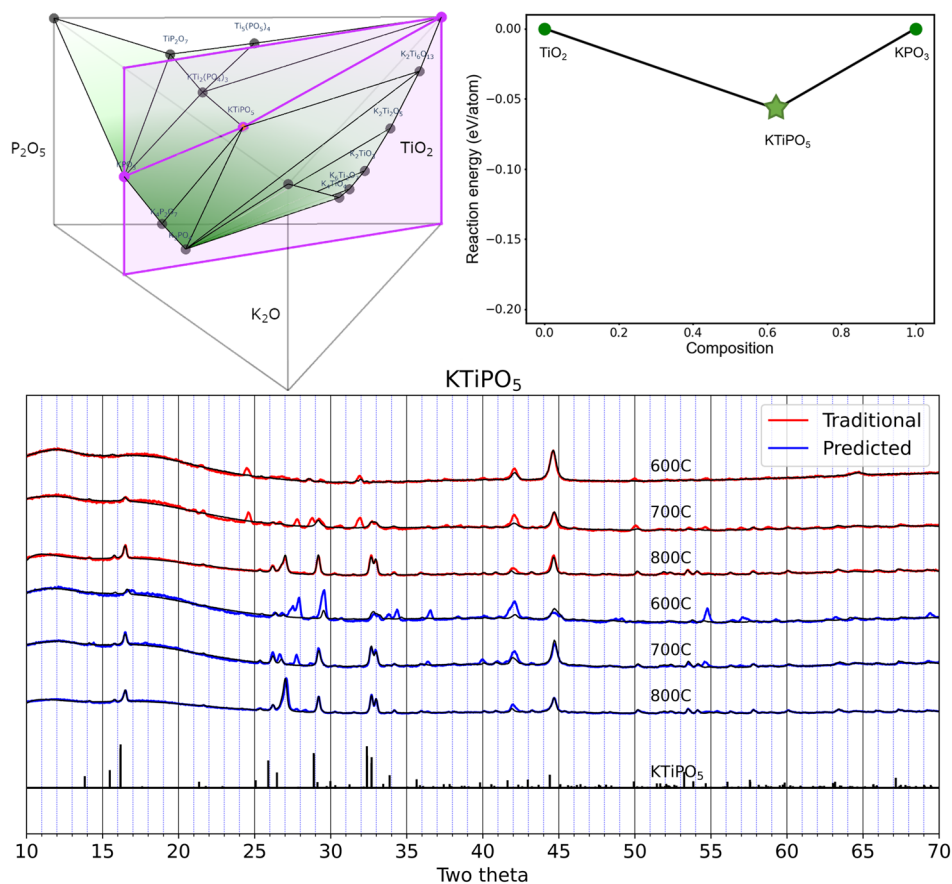


Table 1. Temperature, XRD intensities, and phase fraction of traditional and predicted reactions.

Compound	Precursor type	Precursors	Temp (°C)	Target intensity (e6)	Residual intensity (e6)	Target phase fraction
KTiPO <sub>5</sub>	Traditional	K <sub>2</sub> CO <sub>3</sub> ,	600	0.09	0.42	0.17
		NH <sub>4</sub> H <sub>2</sub> PO <sub>4</sub> ,	700	0.28	0.58	0.33
		TiO <sub>2</sub>	800	0.52	0.27	0.66
	Predicted	KPO <sub>3</sub> , TiO <sub>2</sub>	600	0.21	0.81	0.21
			700	0.68	0.56	0.55
			800	0.52	0.31	0.62

Table 2. Candidate pairwise reactions evaluated using our precursor selection principles

Pairwise	Deepest	Reaction energy	Competing Phases	Inverse hull energy	Reaction	Best
Y	Y	-0.057	0	-0.057	TiO <sub>2</sub> + KPO <sub>3</sub> → KTiPO <sub>5</sub>	Y
Y	N	-0.262	3	-0.049	0.5 P <sub>2</sub> O <sub>5</sub> + 0.5 K <sub>2</sub> Ti <sub>2</sub> O <sub>5</sub> → KTiPO <sub>5</sub>	N
Y	N	-0.084	2	-0.049	0.33 KTi <sub>2</sub> (PO <sub>4</sub> ) <sub>3</sub> + 0.33 K <sub>2</sub> TiO <sub>3</sub> → KTiPO <sub>5</sub>	N
Y	Y	-0.163	3	-0.049	0.5 TiP <sub>2</sub> O <sub>7</sub> + 0.5 K <sub>2</sub> TiO <sub>3</sub> → KTiPO <sub>5</sub>	N

## KNiPO<sub>4</sub>

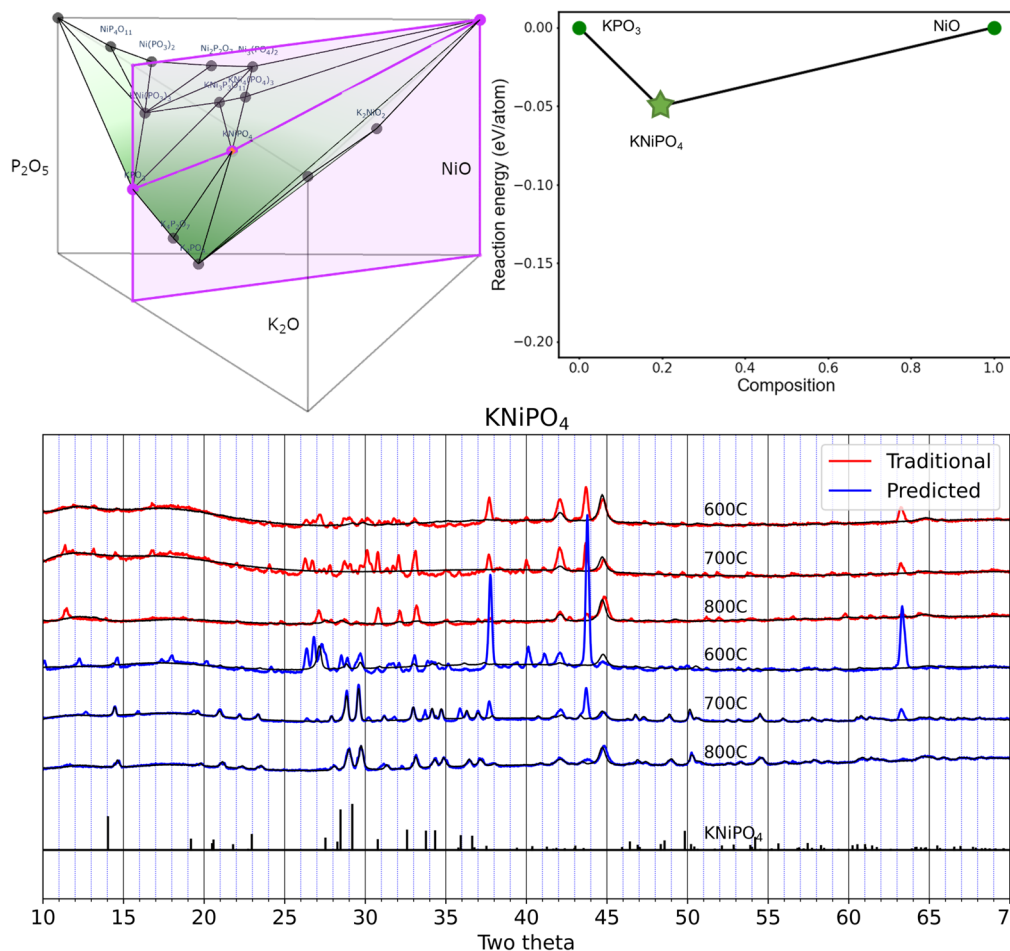


Table 1. Temperature, XRD intensities, and phase fraction of traditional and predicted reactions.

Compound	Precursor type	Precursors	Temp (°C)	Target intensity (e6)	Residual intensity (e6)	Target phase fraction
KNiPO <sub>4</sub>	Traditional	K <sub>2</sub> CO <sub>3</sub> , NH <sub>4</sub> H <sub>2</sub> PO <sub>4</sub> , NiO	600	0.15	0.87	0.15
			700	0.00	1.07	0.00
			800	0.21	0.62	0.25
	Predicted	KPO <sub>3</sub> , NiO	600	0.23	2.26	0.09
			700	1.13	1.04	0.52
			800	0.75	0.34	0.69

Table 2. Candidate pairwise reactions evaluated using our precursor selection principles

Pairwise	Deepest	Reaction energy	Competing Phases	Inverse hull energy	Reaction	Best
Y	Y	-0.05	0	-0.05	KPO <sub>3</sub> + NiO → KNiPO <sub>4</sub>	Y
Y	N	-0.322	5	-0.043	0.5 K <sub>2</sub> NiO <sub>2</sub> + 0.5 Ni(PO <sub>3</sub> ) <sub>2</sub> → KNiPO <sub>4</sub>	N
Y	N	-0.303	4	-0.041	0.5 K <sub>2</sub> O + 0.5 Ni <sub>2</sub> P <sub>2</sub> O <sub>7</sub> → KNiPO <sub>4</sub>	N
Y	N	-0.187	2	-0.041	0.33 K <sub>2</sub> O + 0.33 KNi <sub>3</sub> P <sub>3</sub> O <sub>11</sub> → KNiPO <sub>4</sub>	N
Y	Y	-0.045	1	-0.031	0.33 Ni <sub>3</sub> (PO <sub>4</sub> ) <sub>2</sub> + 0.33 K <sub>3</sub> PO <sub>4</sub> → KNiPO <sub>4</sub>	N
Y	Y	-0.031	0	-0.031	0.25 KNi <sub>4</sub> (PO <sub>4</sub> ) <sub>3</sub> + 0.25 K <sub>3</sub> PO <sub>4</sub> → KNiPO <sub>4</sub>	N

### $K_3Fe_2(PO_4)_3$

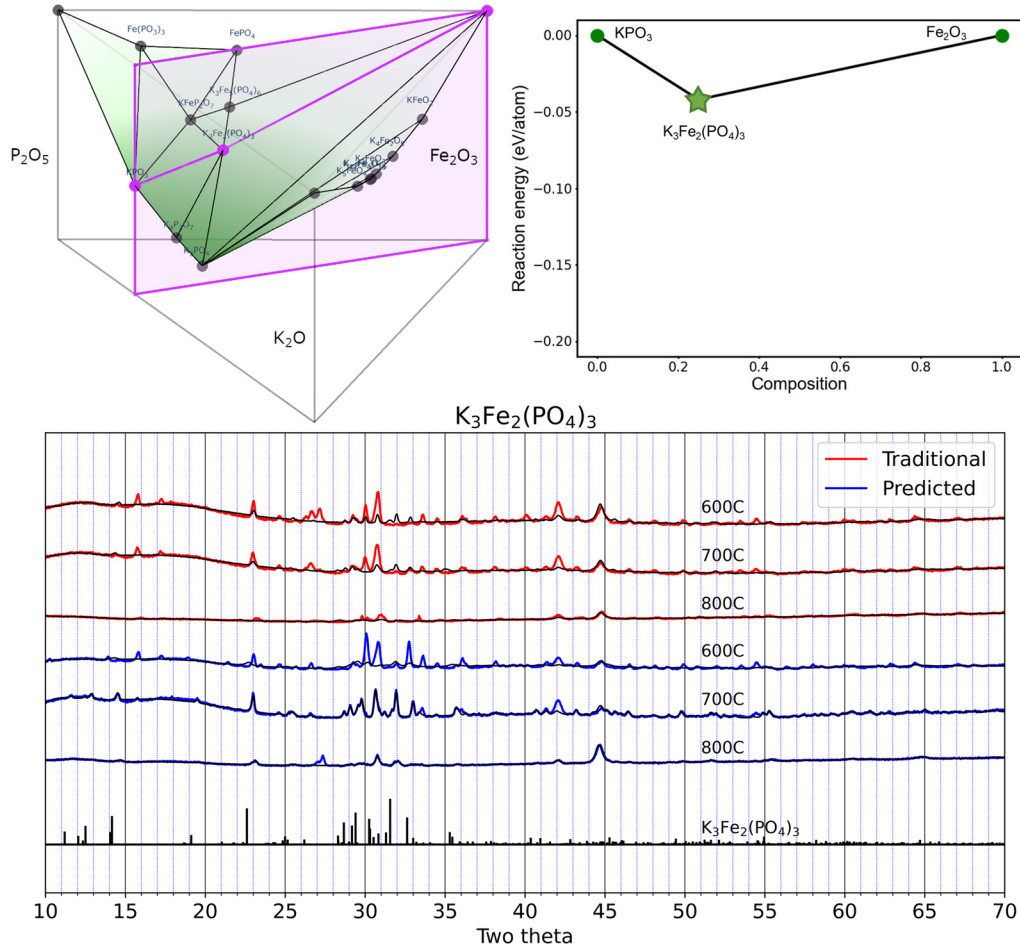


Table 1. Temperature, XRD intensities, and phase fraction of traditional and predicted reactions.

Compound	Precursor type	Precursors	Temp (°C)	Target intensity (e6)	Residual intensity (e6)	Target phase fraction
$K_3Fe_2(PO_4)_3$	Traditional	$Fe_2O_3, K_2CO_3, NH_4H_2PO_4$	600	0.24	0.76	0.24
			700	0.31	0.65	0.33
			800	0.14	0.22	0.39
	Predicted	$Fe_2O_3, KPO_3$	600	0.77	1.09	0.41
			700	0.87	0.42	0.68
			800	0.22	0.19	0.55

Table 2. Candidate pairwise reactions evaluated using our precursor selection principles

Pairwise	Deepest	Reaction energy	Competing Phases	Inverse hull energy	Reaction	Best
Y	Y	-0.042	0	-0.042	$3 KPO_3 + Fe_2O_3 \rightarrow K_3Fe_2(PO_4)_3$	Y
Y	N	-0.105	3	-0.031	$0.5 K_3FeO_3 + 1.5 KFeP_2O_7 \rightarrow K_3Fe_2(PO_4)_3$	N
Y	N	-0.3	4	-0.031	$K_3FeO_3 + Fe(PO_3)_3 \rightarrow K_3Fe_2(PO_4)_3$	N
Y	Y	-0.07	1	-0.026	$2 FePO_4 + K_3PO_4 \rightarrow K_3Fe_2(PO_4)_3$	N
Y	Y	-0.026	0	-0.026	$0.4 K_3Fe_5(PO_4)_6 + 0.6 K_3PO_4 \rightarrow K_3Fe_2(PO_4)_3$	N

# KNbWO<sub>6</sub>

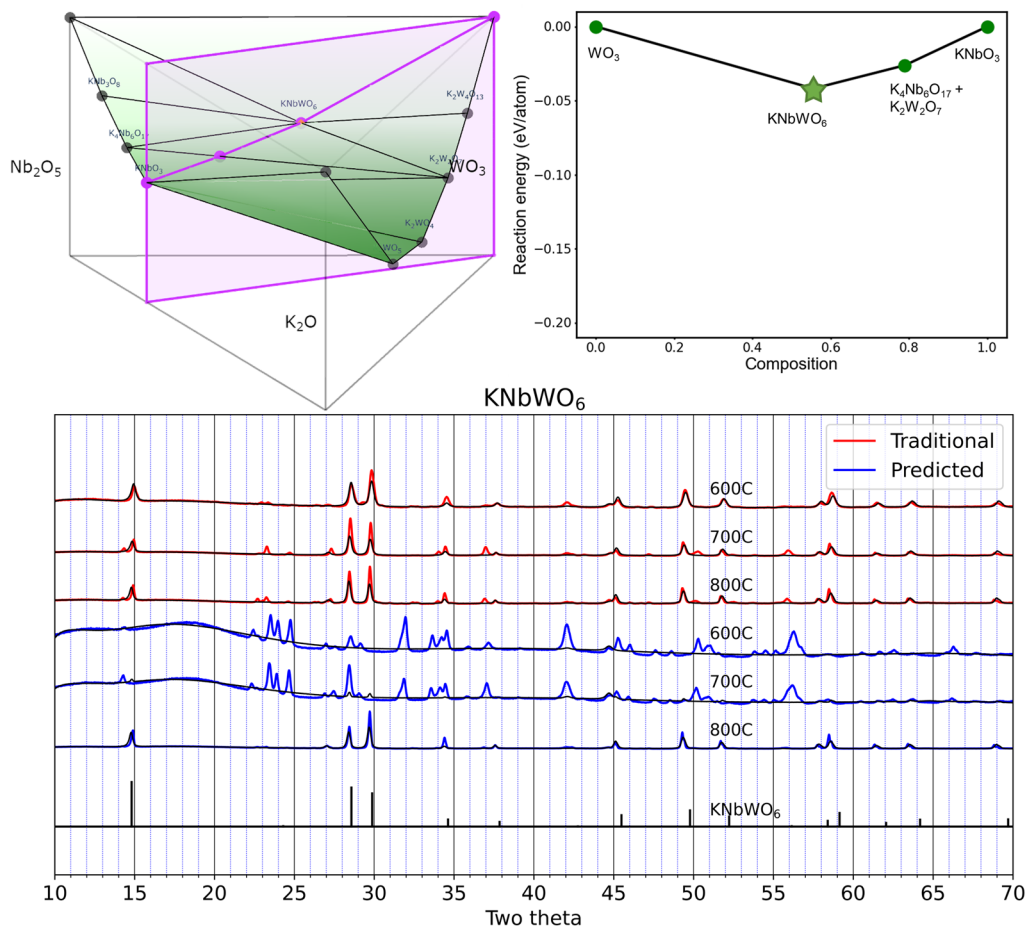


Table 1. Temperature, XRD intensities, and phase fraction of traditional and predicted reactions.

Compound	Precursor type	Precursors	Temp (°C)	Target intensity (e6)	Residual intensity (e6)	Target phase fraction
KNbWO <sub>6</sub>	Traditional	K <sub>2</sub> CO <sub>3</sub> , WO <sub>3</sub> Nb <sub>2</sub> O <sub>5</sub>	600	1.96	1.02	0.66
			700	2.65	2.49	0.52
			800	1.37	1.18	0.54
	Predicted	KNbO <sub>3</sub> , WO <sub>3</sub>	600	0.00	2.18	0.00
			700	0.09	2.43	0.04
			800	2.97	1.86	0.61

Table 2. Candidate pairwise reactions evaluated using our precursor selection principles

Pairwise	Deepest	Reaction energy	Competing Phases	Inverse hull energy	Reaction	Best
Y	Y	-0.042	1	-0.024	KNbO <sub>3</sub> + WO <sub>3</sub> → KNbWO <sub>6</sub>	Y
Y	Y	-0.022	0	-0.022	0.5 Nb <sub>2</sub> O <sub>5</sub> + 0.5 K <sub>2</sub> W <sub>2</sub> O <sub>7</sub> → KNbWO <sub>6</sub>	N

## KTa<sub>2</sub>PO<sub>8</sub>

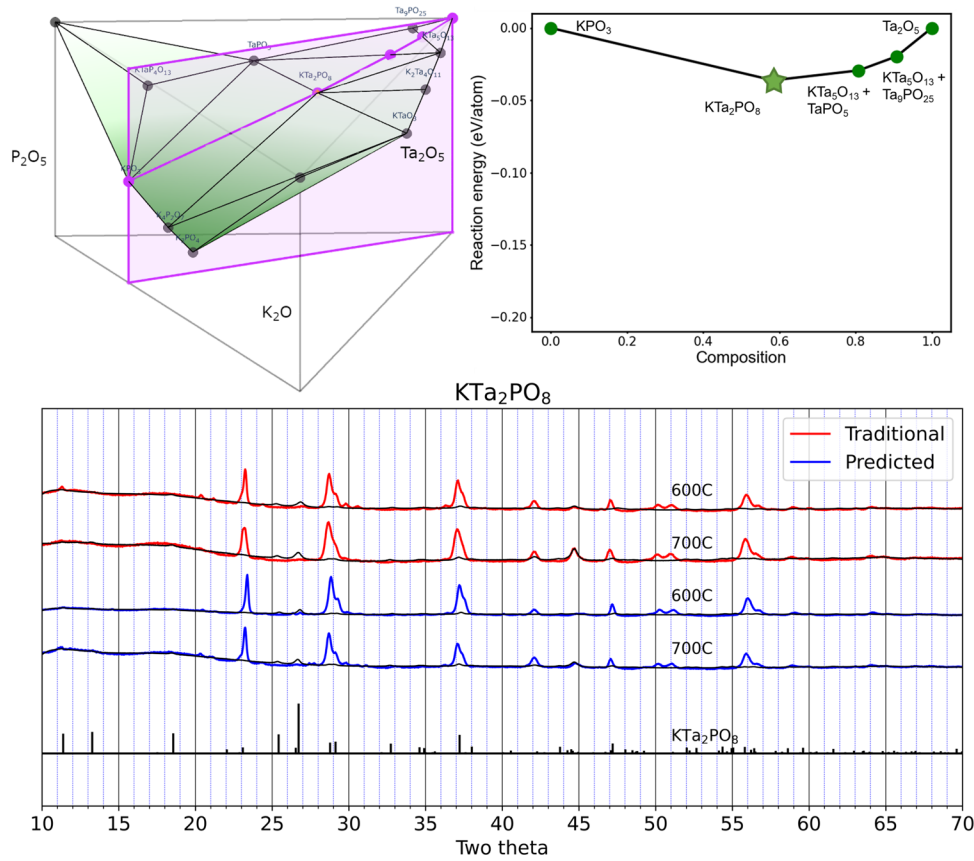


Table 1. Temperature, XRD intensities, and phase fraction of traditional and predicted reactions.

Compound	Precursor type	Precursors	Temp (°C)	Target intensity (e6)	Residual intensity (e6)	Target phase fraction
KTa <sub>2</sub> PO <sub>8</sub>	Traditional	K <sub>2</sub> CO <sub>3</sub> , Ta <sub>2</sub> O <sub>5</sub> , NH <sub>4</sub> H <sub>2</sub> PO <sub>4</sub>	600	0.36	1.50	0.19
			700	0.46	1.77	0.21
	Predicted	KPO <sub>3</sub> , Ta <sub>2</sub> O <sub>5</sub>	600	0.46	2.71	0.14
			700	0.30	1.52	0.16

Table 2. Candidate pairwise reactions evaluated using our precursor selection principles

Pairwise	Deepest	Reaction energy	Competing Phases	Inverse hull energy	Reaction	Best
Y	Y	-0.036	2	-0.015	KPO <sub>3</sub> + Ta <sub>2</sub> O <sub>5</sub> → KTa <sub>2</sub> PO <sub>8</sub>	Y
Y	Y	-0.01	0	-0.01	KTaO <sub>3</sub> + TaPO <sub>5</sub> → KTa <sub>2</sub> PO <sub>8</sub>	N
Y	N	-0.124	2	-0.009	0.5 K <sub>2</sub> Ta <sub>4</sub> O <sub>11</sub> + 0.5 P <sub>2</sub> O <sub>5</sub> → KTa <sub>2</sub> PO <sub>8</sub>	N

## Li<sub>3</sub>Y<sub>2</sub>(BO<sub>3</sub>)<sub>3</sub>

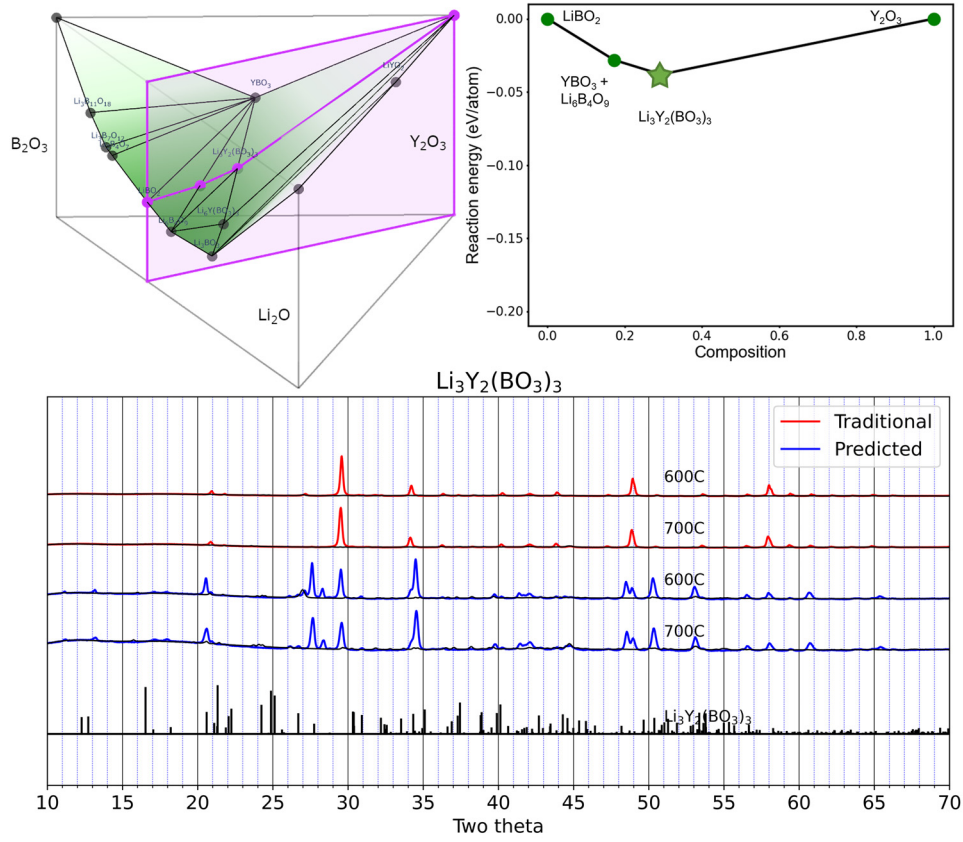


Table 1. Temperature, XRD intensities, and phase fraction of traditional and predicted reactions.

Compound	Precursor type	Precursors	Temp (°C)	Target intensity (e6)	Residual intensity (e6)	Target phase fraction
Li <sub>3</sub> Y <sub>2</sub> (BO <sub>3</sub> ) <sub>3</sub>	Traditional	B <sub>2</sub> O <sub>3</sub> , Li <sub>2</sub> CO <sub>3</sub> , Y <sub>2</sub> O <sub>3</sub>	600	0.56	4.00	0.12
			700	0.20	2.88	0.07
	Predicted	LiBO <sub>2</sub> , Y <sub>2</sub> O <sub>3</sub>	600	0.40	3.56	0.10
			700	0.52	2.45	0.17

Table 2. Candidate pairwise reactions evaluated using our precursor selection principles

Pairwise	Deepest	Reaction energy	Competing Phases	Inverse hull energy	Reaction	Best
Y	Y	-0.038	2	-0.014	Y <sub>2</sub> O <sub>3</sub> + 3 LiBO <sub>2</sub> → Li <sub>3</sub> Y <sub>2</sub> (BO <sub>3</sub> ) <sub>3</sub>	Y
Y	N	-0.01	1	0	2 YBO <sub>3</sub> + Li <sub>3</sub> BO <sub>3</sub> → Li <sub>3</sub> Y <sub>2</sub> (BO <sub>3</sub> ) <sub>3</sub>	N
Y	Y	0	0	0	1.5 YBO <sub>3</sub> + 0.5 Li <sub>6</sub> Y(BO <sub>3</sub> ) <sub>3</sub> → Li <sub>3</sub> Y <sub>2</sub> (BO <sub>3</sub> ) <sub>3</sub>	N

## Na<sub>2</sub>Al<sub>2</sub>B<sub>2</sub>O<sub>7</sub>

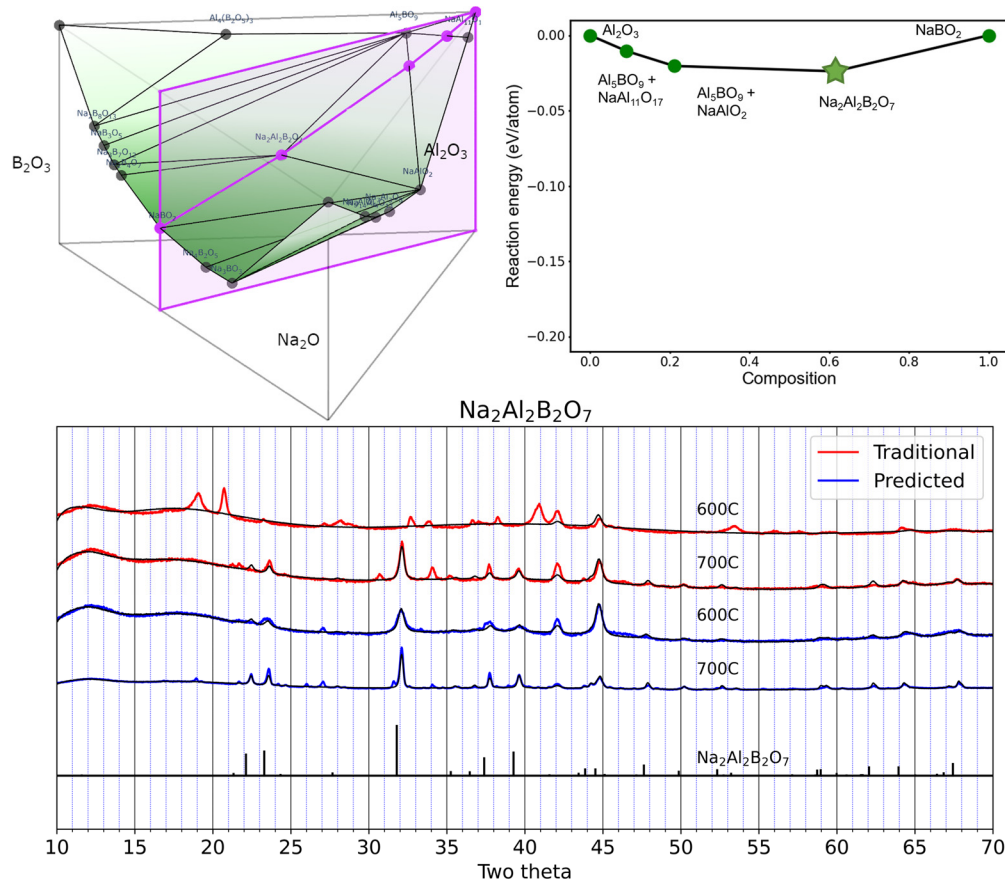


Table 1. Temperature, XRD intensities, and phase fraction of traditional and predicted reactions.

Compound	Precursor type	Precursors	Temp (°C)	Target intensity (e6)	Residual intensity (e6)	Target phase fraction
Na <sub>2</sub> Al <sub>2</sub> B <sub>2</sub> O <sub>7</sub>	Traditional	Al <sub>2</sub> O <sub>3</sub> , B <sub>2</sub> O <sub>3</sub> , Na <sub>2</sub> CO <sub>3</sub>	600	0.00	1.11	0.00
			700	0.46	0.54	0.46
	Predicted	Al <sub>2</sub> O <sub>3</sub> , NaBO <sub>2</sub>	600	0.48	0.43	0.52
			700	1.28	0.84	0.60

Table 2. Candidate pairwise reactions evaluated using our precursor selection principles

Pairwise	Deepest	Reaction energy	Competing Phases	Inverse hull energy	Reaction	Best
Y	Y	-0.024	2	-0.014	Al <sub>2</sub> O <sub>3</sub> + 2 NaBO <sub>2</sub> → Na <sub>2</sub> Al <sub>2</sub> B <sub>2</sub> O <sub>7</sub>	Y
Y	N	-0.068	4	-0.012	B <sub>2</sub> O <sub>3</sub> + 2 NaAlO <sub>2</sub> → Na <sub>2</sub> Al <sub>2</sub> B <sub>2</sub> O <sub>7</sub>	N

# NaSiBO<sub>4</sub>

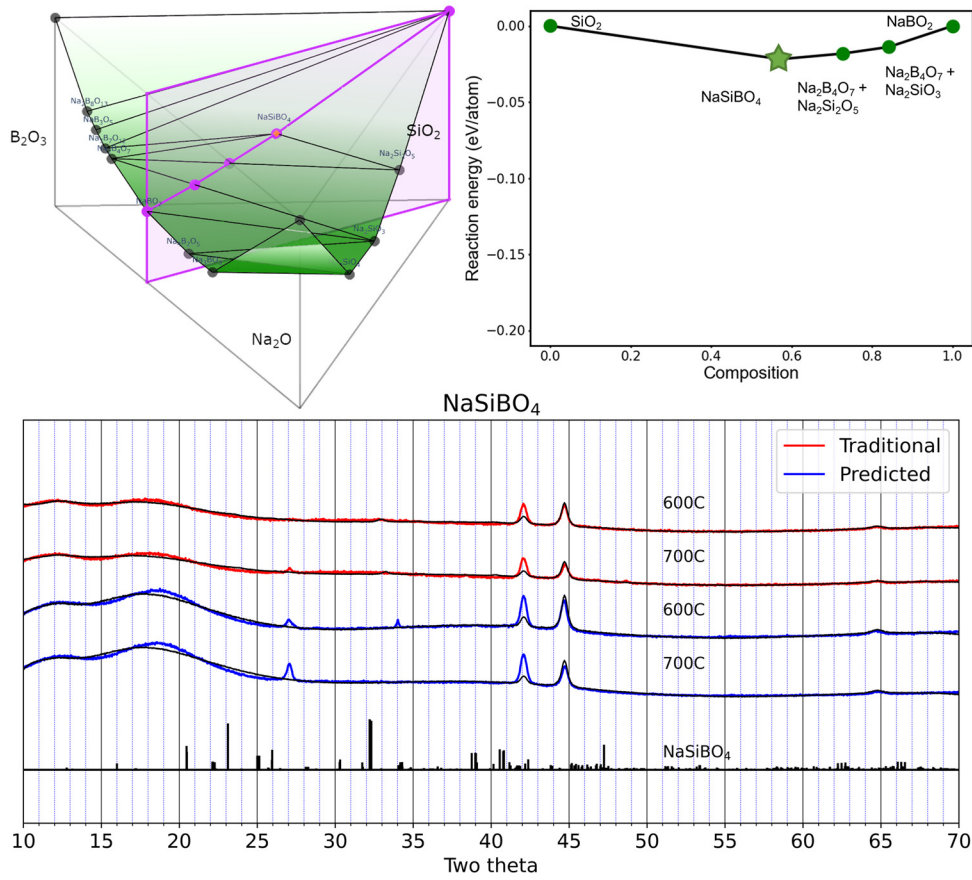


Table 1. Temperature, XRD intensities, and phase fraction of traditional and predicted reactions.

Compound	Precursor type	Precursors	Temp (°C)	Target intensity (e6)	Residual intensity (e6)	Target phase fraction
NaSiBO <sub>4</sub>	Traditional	B <sub>2</sub> O <sub>3</sub> , Na <sub>2</sub> CO <sub>3</sub> , SiO <sub>2</sub>	600	0.09	0.40	0.18
			700	0.08	0.45	0.15
	Predicted	NaBO <sub>2</sub> , SiO <sub>2</sub>	600	0.00	0.70	0.00
			700	0.00	0.79	0.00

Table 2. Candidate pairwise reactions evaluated using our precursor selection principles

Pairwise	Deepest	Reaction energy	Competing Phases	Inverse hull energy	Reaction	Best
Y	N	-0.049	3	-0.007	0.5 Na <sub>2</sub> Si <sub>2</sub> O <sub>5</sub> + 0.5 B <sub>2</sub> O <sub>3</sub> → NaSiBO <sub>4</sub>	N
Y	Y	-0.022	2	-0.008	SiO <sub>2</sub> + NaBO <sub>2</sub> → NaSiBO <sub>4</sub>	Y

## KTiNbO<sub>5</sub>

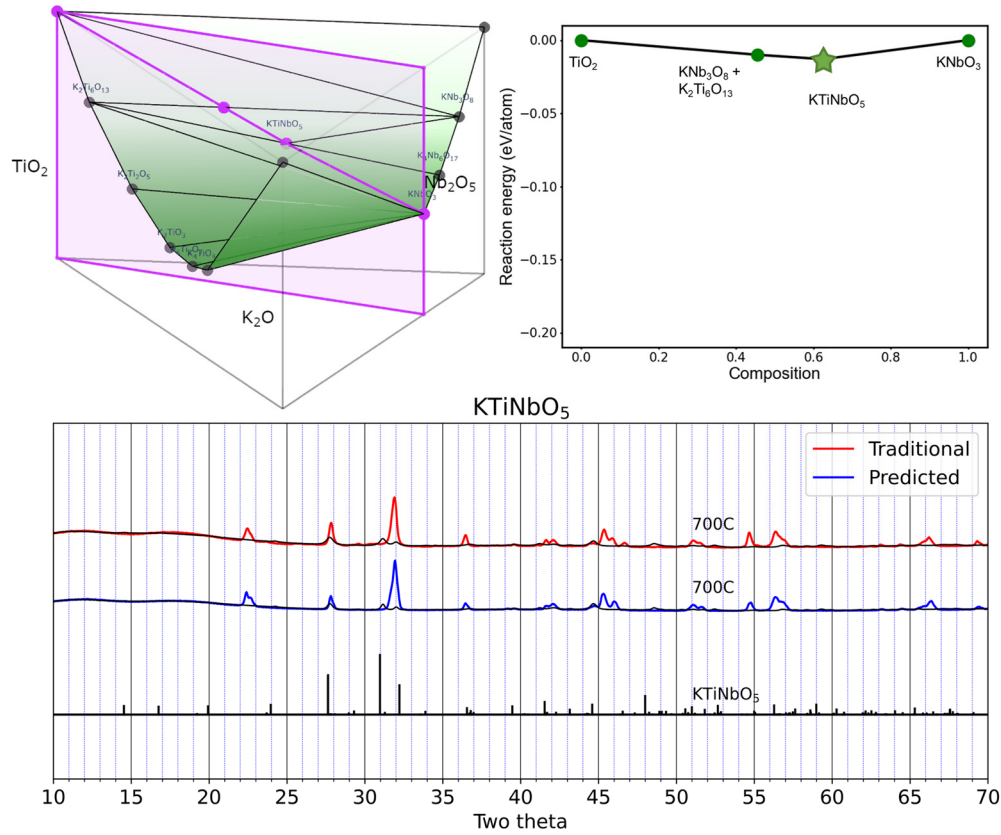


Table 1. Temperature, XRD intensities, and phase fraction of traditional and predicted reactions.

Compound	Precursor type	Precursors	Temp (°C)	Target intensity (e6)	Residual intensity (e6)	Target phase fraction
KTiNbO <sub>5</sub>	Traditional	K <sub>2</sub> CO <sub>3</sub> , Nb <sub>2</sub> O <sub>5</sub> , TiO <sub>2</sub>	700	0.78	2.06	0.27
	Predicted	KNbO <sub>3</sub> , TiO <sub>2</sub>	700	0.50	2.21	0.18

Table 2. Candidate pairwise reactions evaluated using our precursor selection principles

Pairwise	Deepest	Reaction energy	Competing Phases	Inverse hull energy	Reaction	Best
Y	Y	-0.061	4	-0.006	0.5 Nb <sub>2</sub> O <sub>5</sub> + 0.5 K <sub>2</sub> Ti <sub>2</sub> O <sub>5</sub> → KTiNbO <sub>5</sub>	Y
Y	Y	-0.013	2	-0.006	TiO <sub>2</sub> + KNbO <sub>3</sub> → KTiNbO <sub>5</sub>	N
Y	Y	0	0	0	0.17 K <sub>4</sub> Nb <sub>6</sub> O <sub>17</sub> + 0.17 K <sub>2</sub> Ti <sub>6</sub> O <sub>13</sub> → KTiNbO <sub>5</sub>	N

# LiSi<sub>2</sub>BO<sub>6</sub>

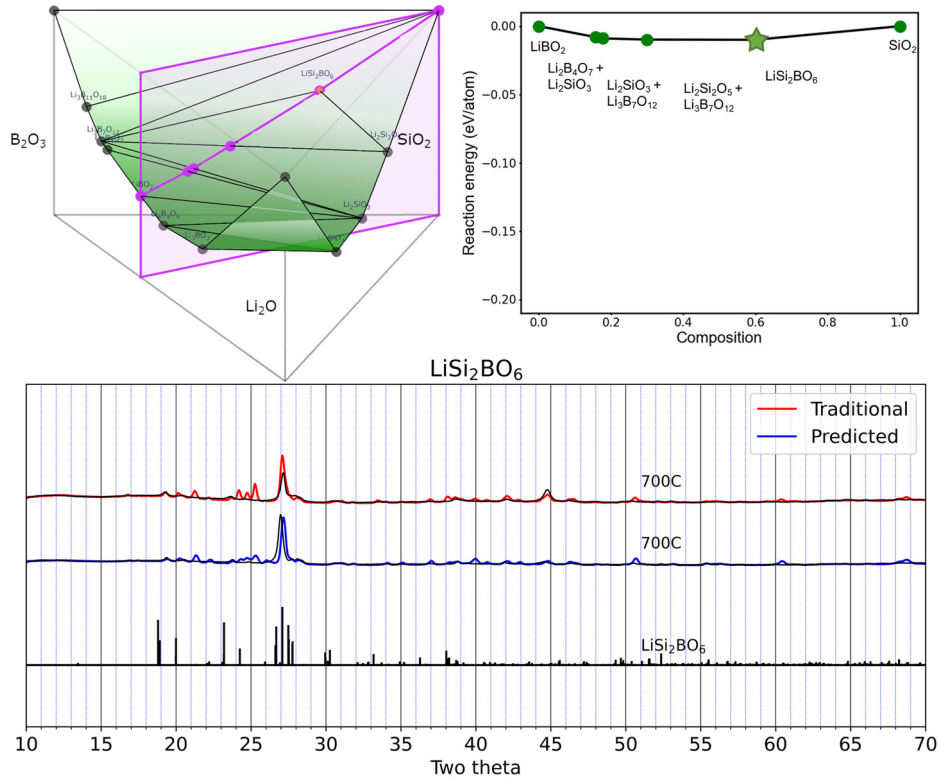


Table 1. Temperature, XRD intensities, and phase fraction of traditional and predicted reactions.

Compound	Precursor type	Precursors	Temp (°C)	Target intensity (e6)	Residual intensity (e6)	Target phase fraction
LiSi <sub>2</sub> BO <sub>6</sub>	Traditional	B <sub>2</sub> O <sub>3</sub> , Li <sub>2</sub> CO <sub>3</sub> , SiO <sub>2</sub>	700	1.34	1.59	0.46
	Predicted	LiBO <sub>2</sub> , SiO <sub>2</sub>	700	0.94	2.56	0.27

Table 2. Candidate pairwise reactions evaluated using our precursor selection principles

Pairwise	Deepest	Reaction energy	Competing Phases	Inverse hull energy	Reaction	Best
Y	Y	-0.01	3	-0.004	2 SiO <sub>2</sub> + LiBO <sub>2</sub> → LiSi <sub>2</sub> BO <sub>6</sub>	Y

# LiNbWO<sub>6</sub>

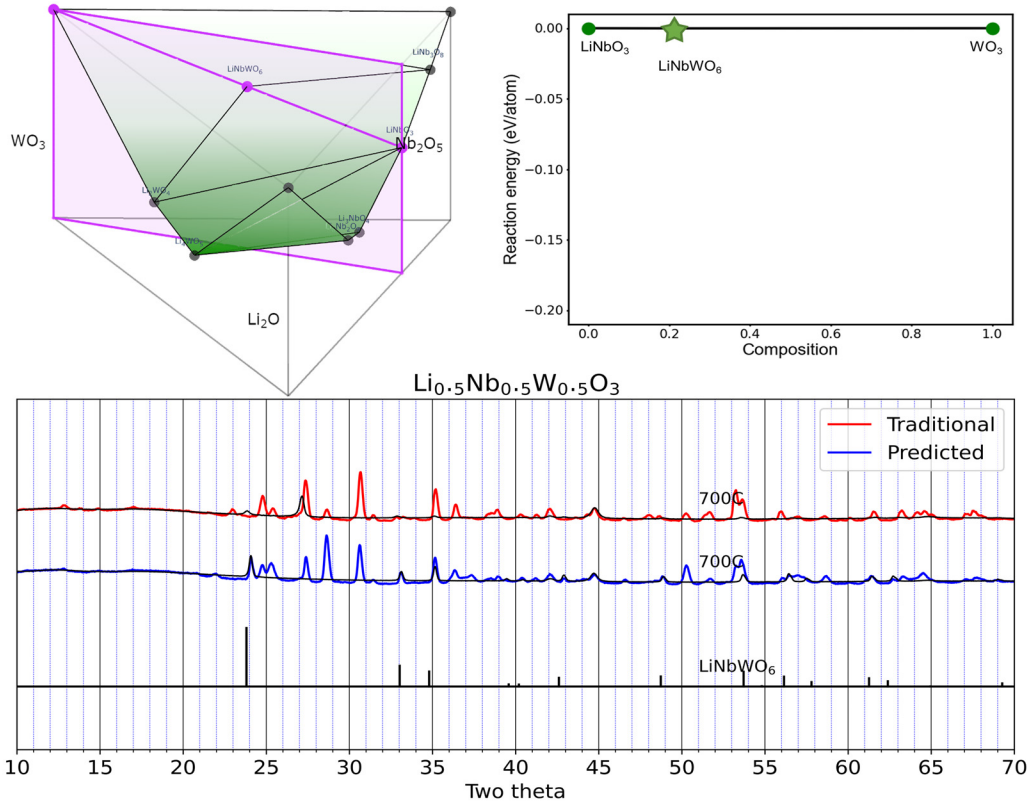


Table 1. Temperature, XRD intensities, and phase fraction of traditional and predicted reactions.

Compound	Precursor type	Precursors	Temp (°C)	Target intensity (e6)	Residual intensity (e6)	Target phase fraction
LiNbWO <sub>6</sub>	Traditional	Li <sub>2</sub> CO <sub>3</sub> , Nb <sub>2</sub> O <sub>5</sub> , WO <sub>3</sub>	700	0.14	2.52	0.05
	Predicted	LiNbO <sub>3</sub> , WO <sub>3</sub>	700	0.41	2.05	0.17

Table 2. Candidate pairwise reactions evaluated using our precursor selection principles

Pairwise	Deepest	Reaction energy	Competing Phases	Inverse hull energy	Reaction	Best
Y	Y	0	1	0	LiNbO <sub>3</sub> + WO <sub>3</sub> → LiNbWO <sub>6</sub>	Y

# LiZnBO<sub>3</sub>

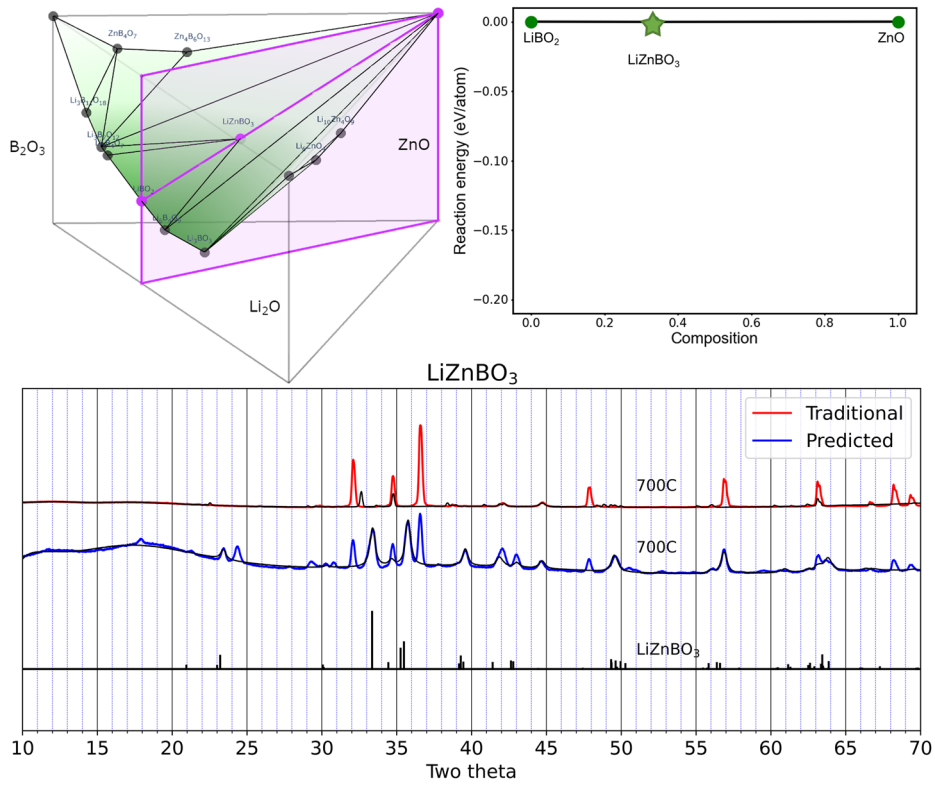


Table 1. Temperature, XRD intensities, and phase fraction of traditional and predicted reactions.

Compound	Precursor type	Precursors	Temp (°C)	Target intensity (e6)	Residual intensity (e6)	Target phase fraction
LiZnBO <sub>3</sub>	Traditional	B <sub>2</sub> O <sub>3</sub> , Li <sub>2</sub> CO <sub>3</sub> , ZnO	700	0.74	4.07	0.15
	Predicted	LiBO <sub>2</sub> , ZnO	700	2.11	1.93	0.52

Table 2. Candidate pairwise reactions evaluated using our precursor selection principles

Pairwise	Deepest	Reaction energy	Competing Phases	Inverse hull energy	Reaction	Best
Y	Y	0	0	0	ZnO + LiBO <sub>2</sub> → LiZnBO <sub>3</sub>	Y